UNIVERSITA' DEGLI STUDI DI MILANO

Facoltà di Medicina e Chirurgia

Dipartimento di Biotecnologie Mediche e Medicina Traslazionale

Dottorato di ricerca in Farmacologia, Chemioterapia e Tossicologia mediche

XXV ciclo

Mechanisms of protein transport at the ER-Golgi interface

Settore disciplinare BIO/14

Tesi di Dottorato di Ricerca di:

Matteo Fossati

Docente guida: Prof. Nica Borgese

Coordinatore del corso: Prof. Alberto Emilio Panerai

Anno accademico 2011/2012

CONTENTS

ABSTRACT

The Endoplasmic Reticulum represents the first station of the secretory pathway, where proteins destined to the cell surface or to some intracellular organelles are recruited in specific ER subdomains, the ER Exit Sites (ERES), and start to travel into transport carriers to reach the proper final destination. Even though cargoes are usually recruited to ERES by a sequence-dependent mechanism, it is known that other factors contribute to protein export from the ER. Using model fluorescent tail-anchored proteins our group previously demonstrated that the length/hydrophobicity of the transmembrane domain is an important factor determining recruitment to or exclusion from ERES: a protein with a short TMD (FP-17) is excluded from ERES and retained in the ER, while a longer TMD (FP-22) determines enrichment in ERES. In order to clarify the molecular mechanism underlying this TMD-dependent transport, we first compared the transport of an export signal-bearing (VSV-G DxE) membrane protein with our model protein FP22, which lacks an export signal. FP22 and VSV-G accumulate together at ERES, but VSVG reaches the plasma membrane more rapidly than FP22. To investigate the basis of this difference, we combined cDNA microinjection to temperature blocks and live-cell imaging approaches that allowed us to analyze the transport at early steps of the secretory pathway at the ER-Golgi interface. At 20°C, a temperature at which only the transport between the ER and the Golgi is allowed, all of the VSVG accumulates in the Golgi, while FP-22 remains distributed between the ER and the Golgi. After bleaching the Golgi fraction of FP22 we observed a rapid, energy-dependent, fluorescence recovery, indicating an efficient ER to Golgi transport even in the absence of the export signal and suggesting that FP22 may be recycled between the two compartments. In agreement, a rapid emptying of the Golgi was observed after ER bleaching (accompanied by a fluorescence recovery of the ER fraction). To investigate whether this phenomenon is restricted to our model protein only or it is more general event, we then tested the behavior of a signal-deleted form of VSV-G (VSV-G AxA). Similarly to FP22, VSVG AxA is distributed between the Golgi and the ER at 20°C and Golgi fluorescence rapidly decreases after ER bleaching, suggesting a new role of the ER export signal, which is important not only in re-

cruiting cargoes at the ERES, but also in preventing their recruitment into futile cycles between the Golgi and the ER, which delay their arrival to the cell surface.

To further characterize the mechanism of TMD-dependent sorting, we then investigated the role of membrane curvature; our group previously demonstrated that FP-22 is segregated from FP-17 in specific ER subdomains, which are characterized by membrane curvature (ERES and ER tubules). In collaboration with Bruno Goud and Jean-Baptiste Manneville (Institute Curie, Paris), we created highly curved domains using membranes composed of a uniform lipid composition (POPC, palmitoyl-oleyl-phosphatidylcholine) or ER lipids extracted from rat liver microsomes, and we analyzed the distribution of our two model proteins in flat and curved domains. Our results indicate that the two proteins are uniformly distributed in curved membranes and strongly suggest that the membrane curvature alone cannot drive the TMD-dependent partitioning of membrane proteins in ERES and ER tubules.

Taken together, our data contribute to clarify the role of two fundamental factors influencing the transport of membrane proteins along the secretory pathway that were never investigated before.

ABBREVIATIONS

ALPS: Amphipatic Lipid Packing Sensor

BAR: Bin Amphiphysin Rvs domain

(Cyt)b_5: cytochrome b_5

COPI: Coatomer Complex I

COPII: Coatomer Complex II

DIC: Differential Interference Contrast

DOPE: 1,2-dioleyl-phosphatidylethanolamine

DSPE: 1,2-distearoyl-phosphatidylethanolamine

ER: Endoplasmic Reticulum

ERES: Endoplasmic Reticulum Exit Sites

ERGIC: ER to Golgi Intermediate Compartment

FRAP: Fluorescent Recovery After Photobleaching

GEF: Guanine nucleotide Exchange Factor

GPI-anchored protein: GlycoPhosphatidylInostol-anchored protein

GUV: Giant Unilamellar Vesicle

IC: Intermediate Compartment

ITO: Indium Tin Oxide

LUV: Large Unilamellar Vesicle

MTs: Microtubules

OT: Optical Tweezers

PAIRS: Pairing Analysis of Cargo Receptors

PM: Plasma Membrane

POPC: Palmitoyl-oleyl-PhosphatidylCholine

PtdCho: phosphatidylcholine

PtdEtn: phosphatidylethanolamine

PtdIns: phosphatidylinositol

PtdSer: phosphatidylserine

ROI: Region of Interest

SM: sphingomyelin

SNARE: Soluble NSF Attachment protein REceptor

SRP: Signal Recognition Particle

TA: C-tail-anchored

tER: transitional Endoplasmic Reticulum

TGN: *trans*-Golgi network

TMD: transmembrane domain

VSV-G: Vesicular Stomatitis Virus - Glycoprotein

1. INTRODUCTION

The unique feature of eukaryotic cells is the presence of a complex subdivision into physically distinct compartments and organelles. This organization is crucial for a correct cellular function and to ensure that different reactions, each essential for cell life, occur at specific rates without interfering with other processes. For examples, acid hydrolases have to be segregated into lysosomes in order to efficiently degrade cellular junk without the elimination of other cellular components. Thus, each organelle has its own set of membrane and luminal components that confer its functional specialization. In addition to specific proteins, each organelle is enclosed by unique bilayers in terms of lipid composition.

Due to this complex organization, eukaryotic cells have developed a highly dynamic trafficking system that is essential to maintain the differences between organelles and their identity. The cellular sorting machinery is a very efficient system, which mediates continuous exchanges between contiguous compartments and a constant regeneration and replacement of proteins and lipids.

In this chapter I will summarize the organization and functional principles of the secretory pathway, which represents the a group of physically distinct but functionally interconnected organelles dedicated to the traffic of macromolecules between the cell interior and the extracellular world.

1.1 The secretory pathway

The secretory pathway consists of a number of independent organelles that function sequentially to mediate protein and lipid transport (Fig. 1). Each compartment has a specialized environment that promotes the different events that are required for protein secretion such as protein biogenesis, post-translational modifications and targeting to the correct final destination.

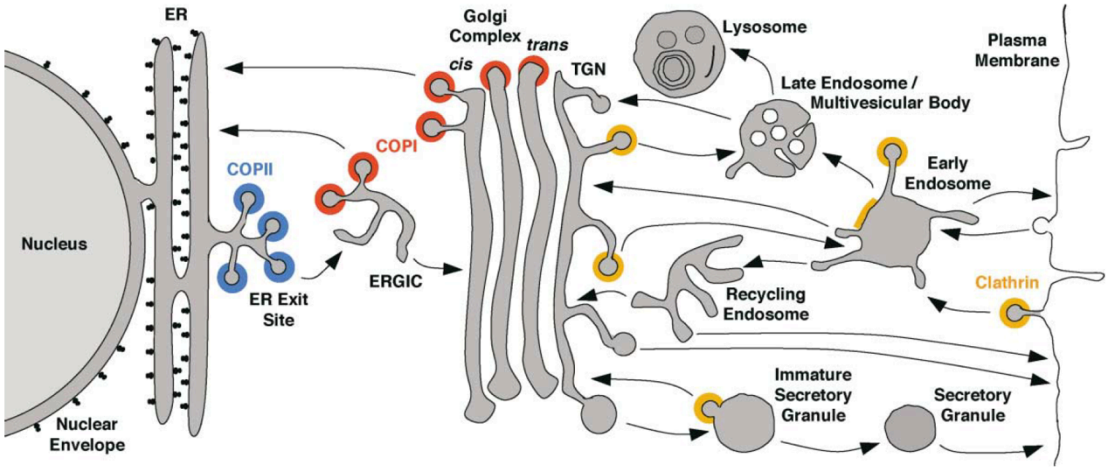

Figure 1: The complexity of the exo-endocytic pathway (Bonifacino and Glick, 2004)

The Endoplasmic Reticulum is the entry point into the secretory pathway. All the proteins that carry out their function in any one compartment of the secretory pathway (i.e. Intermediate Compartment, Golgi apparatus, lysosomes and endosomes) or at the plasma membrane, are synthesized on ribosomes docked on ER membranes, properly folded in the ER lumen and then recruited by the secretion machinery to reach their final destination.

The first step in the lifetime of a newly synthesized protein destined to a compartment of the secretory pathway is its insertion – or translocation across – the ER membrane. Depending on protein topology, this event may occur either co- or post-translationally. Most proteins are translocated into the ER in a co-translational fashion. This event is mediated by the Signal Recognition Particle (SRP), which recognizes a specific signal-sequence in the N-terminus of proteins or an internal transmembrane segment (Blobel and Dobberstein, 1975). Then SRP drives the emerging nascent protein together with the ribosome to the ER membrane, where SRP interacts

with its specific membrane receptor. Here, the elongating polypeptide moves directly from the tunnel inside the ribosome to the membrane channel, which is represented by the Sec61 translocon complex (Rapoport, 2007).

As mentioned above, in eukaryotic cells there are also a number of proteins, which are inserted after their translation on ribosomes free in the cytosol. A large and heterogeneous class of these proteins is represented by tail-anchored proteins, which belong to the type II single-spanning membrane proteins with a cytosolic amino terminus and a carboxy terminus transmembrane domain followed by few luminal residues (Borgese et al., 2007; Borgese et al., 2003). Since the hydrophobic segment of TA proteins is in close proximity to the C-terminus, it emerges from ribosomes only after the termination of translation and it cannot be bound co-translationally by SRP. Therefore, their translocation can occur only through a translocon-independent and post-translational mechanism (Yabal et al., 2003), which may be, depending on the physicochemical features of the TA proteins, either assisted or unassisted by cytosolic proteins.

Independently from which mechanism has been used, after membrane insertion/translocation all proteins need to be properly folded and post-translationally modified (i.e. N-glycosylated). Then, if they are not ER resident proteins, cargoes are first recruited into specific ER subdomains, known as ER Exit Sites, leave the ER and start to travel through the secretory pathway to reach their final destination

1.2 Vesicular transport

The overall organization of the secretory pathway was discovered thanks to the work of George Palade and colleagues, more than 30 years ago (Palade, 1975). Fromm this and subsequent work (Rothman and Orci, 1992) it emerged that transport of cargo molecules is mediated by shuttling transport vesicles. According to these findings, vesicles bud from a donor compartment through a process that allows the selective incorporation of cargoes into these budding vesicles; subsequently the vesicles fuse with a specific downstream acceptor compartment where cargoes are released. By contrast, resident proteins of the donor organelles are retained in the donor compartment through their exclusion from recruitment into the budding vesicles.

Since the transport of cargo molecules along the secretory pathway is a highly dynamic process and determines a continuous flux of membranes and effector proteins, eukaryotic cells have developed a parallel retrograde route that balances the forward movement and guarantees the recycling of effectors and the replacement of membranes, essential for the maintenance of organelle architecture and identity.

Even though different effector molecules mediate different steps of the exo-endocytic pathway, all of them follow a general scheme, which can be divided into seven subsequent steps (Bonifacino and Glick, 2004). As shown in figure 2, the formation, budding and fusion of carrier vesicles are complex active processes that involve many effector proteins and require energy.

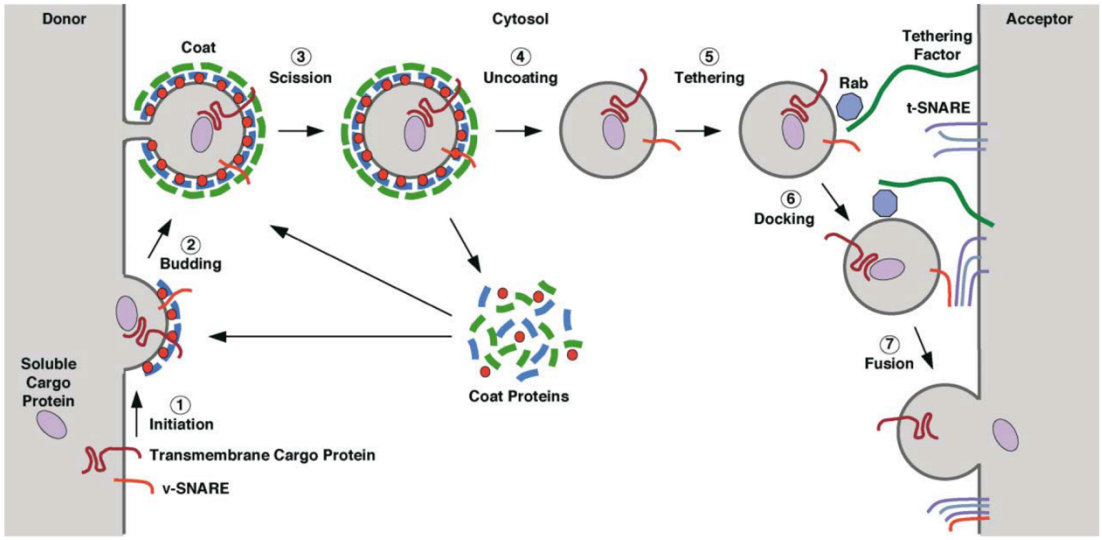

Figure 2: steps of vesicle budding and fusion (Bonifacino and Glick, 2004)

The initiation of vesicle assembly is mediated by the recruitment of adaptor components of the coat complex (or membrane-proximal coat) to the donor compartment by binding to a membrane-associated specific GTPase, leading to the accumulation of cargoes at the assembling coat. Then, the membrane-distal components of the coat bind adaptors and their polymerization into a lattice-like structure drives the progressive deformation of the membrane. The third step is represented by the energy-dependent scission of the vesicle neck, which could be mediated either by coat components themselves (Matsuoka et al., 1998) or by accessory proteins (i.e. dynamin in the case of clathrin-coated pits) (Ferguson and De Camilli, 2012). Once the vesicle has been pinched off from the donor compartment, the membrane-specific small

GTPase hydrolyzes GTP and this energy is used to mediate vesicle uncoating, which is essential to return coat components to the cytosol where they become available for new rounds of vesicle budding; furthermore the vesicles must loose their coat to become more fusogenic. The naked vesicle progressively moves and tethers to the acceptor compartment by interacting with specific Rab GTPases and tethering factors. The specificity of this interaction plays a central role because it determines that cargoes are delivered to the correct destination. Finally, the SNARE complex mediates the late step of vesicular transport by allowing the fusion between vesicle and acceptor membrane. The SNARE complex is composed of three SNAREs (one on the vesicle membrane, the v-SNARE, and three on the acceptor membrane, the t-SNARE) that form a coiled-coil-like helical bundle, which provides the energy required to drive the membrane fusion (Jahn and Grubmuller, 2002). In this way cargo molecules can be released into the acceptor compartment, travel through the different organelles of the secretory pathway and reach their final destination.

1.3 Transport at the ER/Golgi interface

1.3.1 COPII-dependent transport

Cargo molecules that have been properly processed leave the ER through their recruitment at specific ER subdomains, the ER Exit Sites, also known as transitional ER (tER), which are regions not decorated by ribosomes and highly enriched in COPII proteins. There are five core components of COPII are composed, but additional regulatory proteins participate in the correct assembly of carrier vesicles that bud from the ER to reach ERGIC and Golgi compartments (Fig. 3).

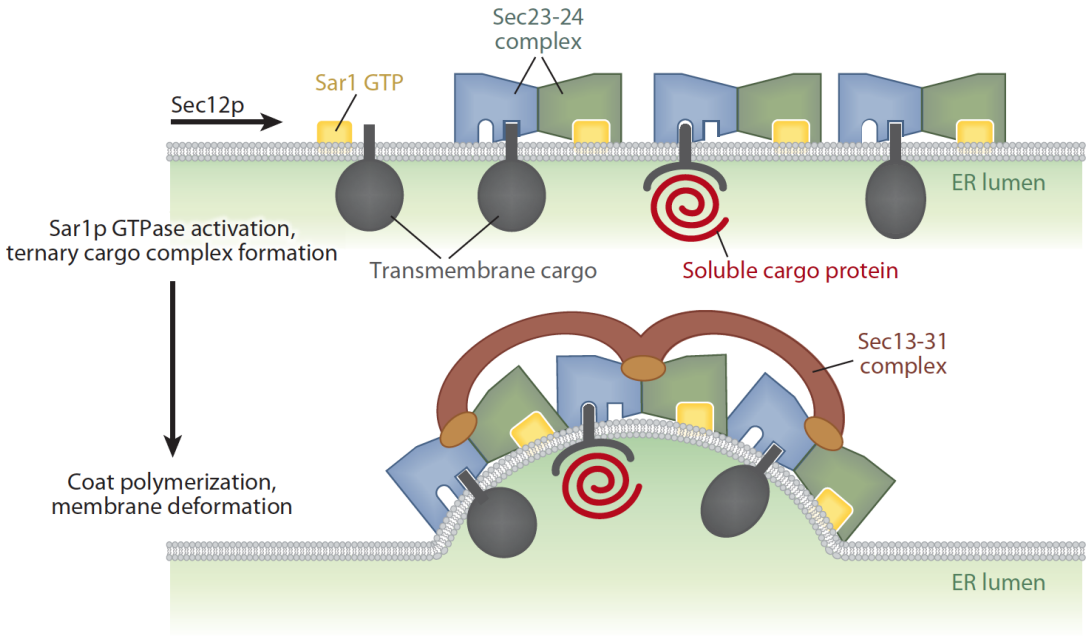

Figure 3: Assembly of COPII-coated vesicle at the ERES (Dancourt and Barlowe, 2010)

The first step of COPII vesicle assembly is the recruitment on the ER membrane of one of the key components involved in this process, the small Ras-like GTPase Sar1 (Lee et al., 2004). Even if it is still unclear what marks these sites for COPII recruitment, Sec16 and Sec12 are two good candidates for this role: Sec16 is a large peripheral ER membrane protein and may serve as scaffold for the nucleation and stabilization of the assembling coat (Espenshade et al., 1995), while Sec12 is the specific guanine nucleotide exchange factor (GEF) for Sar1 (Barlowe and Schekman, 1993). Once bound to GTP, Sar1 exposes its amino-terminal hydrophobic region, which allows its association with the ER membrane and the subsequent recruitment of the COPII heteromeric subcomplex Sec23-Sec24, which constitutes the membrane-proximal adaptor layer of COPII and forms, together with Sar1 the so called pre-budding complex. Sec23 makes direct contact with Sar1-GTP (Bi et al., 2002), while Sec24 mediates the recruitment of cargoes (see below). Once assembled into membranes, the pre-budding complex makes contact with the membrane-distal layer of COPII Sec13-Sec31, which consists of two Sec13 and two Sec31 molecules. Even though a role of Sar1-GTP in bending the membrane has been proposed by *in vitro* studies, the deformation of membrane curvature of the nascent coated vesicle is mainly induced by the polymerization of the external COPII subunits into a mesh-like

structure, which provides the force required to overcome the energetic barrier to membrane bending (Lee et al., 2005).

One of the most debated points about the mechanism of COPII assembly arises from the fact that Sec23 displays a GTPase-activating protein (GAP) activity on Sar1-GTP, which triggers GTP hydrolysis by Sar1, reducing the stability of the assembling complex. And the GAP activity of Sec23 is even augmented about 10 fold by addition of Sec13-Sec31 (Antonny et al., 2001). How can the COPII coat polymerize to cover a forming vesicle if the basic unit of the polymer is unstable? The first possible explanation is that the kinetics of GTP hydrolysis is slower than the kinetics of vesicle budding, giving in this way enough time to the vesicle to leave the ER. Alternatively, GTP hydrolysis could cause only the release of Sar1, while the other components could remain assembled on the membrane (Bonifacino and Glick, 2004). Another possible explanation is that Sec12 is present on the rims of the nascent COPII vesicle and it provides a continual supply of activated Sar1-GTP (Futai et al., 2004; Sato and Nakano, 2005).

Another key point, which is still unclear, concerns the scission of the vesicle neck that represents the last step in COPII vesicle formation. While clathrin-coated vesicles require an accessory protein, dynamin, to sever the vesicle neck, COPII vesicles are intrinsically capable of pinching off the neck, even though the responsible subunit is unknown. Indeed, it has been demonstrated that a mixture of purified Sec23-Sec24, Sec13-Sec31 and Sar1-GTP is able to generate coated vesicles from liposomes (Matsuoka et al., 1998). Some evidences suggest that Sar1 itself, at least *in vitro*, might control membrane constriction of vesicle neck and mediate the scission of COPII-coated vesicles from ER membranes (Long et al., 2010).

1.3.2 COPI-dependent transport

Even though the best characterized function of the COPI system is the retrograde transport of luminal and membrane proteins at the ER/Golgi interface, it has been implicated also in maintaining the correct steady-state distribution of proteins within the Golgi stack (Rabouille and Klumperman, 2005) and in delivering antero-

grade carrier vesicles from the intermediate compartment to the Golgi apparatus, in a process that is subsequent to COPII-dependent transport (Stephens et al., 2000).

Similarly to Sar1 in COPII-mediated transport, the key molecule that organizes specific recruitment of the COPI subunits to donor membrane is the Ras-like GTPase Arf1 (Beck et al., 2009) (Fig. 4). Both the GDP and the GTP-bound forms of Arf1 interact with the membrane. Arf1-GDP binds to the cytoplasmic tail of p23/p24, which are also able, upon binding of their TMD to a specific sphingomyelin species, to interact directly with coatomer and increase the efficiency of vesicle formation (Contreras et al., 2012). Upon GDP/GTP switch, mediated by the GEF protein Gea1, Arf1 undergoes to a conformational change that leads to the exposure of a myristoylated N-terminal amphipatic helix that provides a stable membrane anchorage (Antonny et al., 1997). Once activated, Arf1 and p24 proteins can directly bind and recruit all the seven subunits of the COPI complex (α, β', β, γ, δ, ζ and ε). As described for the membrane-distal layer of the COPII coat, the interaction of COPI components with the other effectors Arf1 and p24, triggers coat polymerization and membrane deformation. And finally, the neck of the nascent COPI-coated vesicle is pinched off by Arf1-GTP itself (Spang et al., 1998).

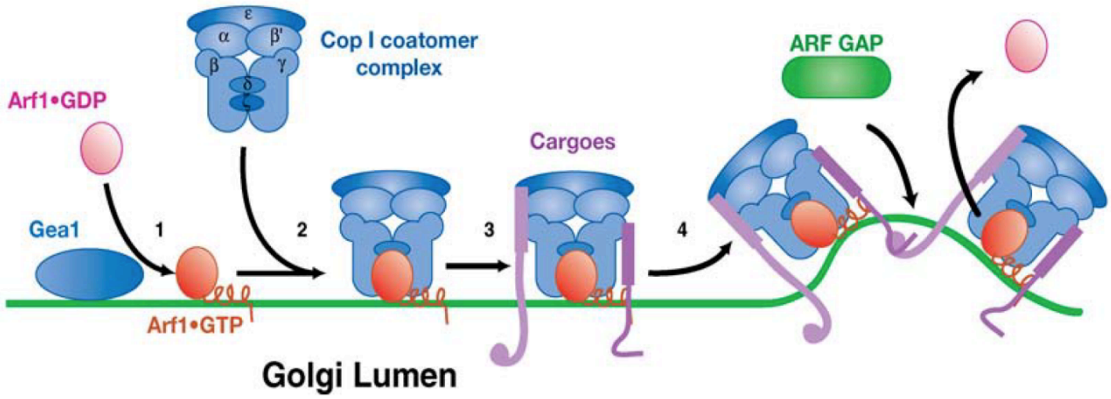

Figure 4: the main steps of COPI-coated vesicles (Lee et al., 2004)

Once released from the donor compartment, the COPI-coated vesicle needs to be uncoated in order to be competent for subsequent fusion with the acceptor membrane. Similarly to Sar1 in COPII-dependent transport, the uncoating step depends on the GTP hydrolysis activity of Arf1, which is stimulated by Arf-directed GTPase-

activating proteins ArfGAPs. In mammals, three Golgi-localized ArfGAPs have been identified, ArfGAP1 and ArfGAP2/3 (Cukierman et al., 1995). ArfGAP1 differs from the other two ArfGAPs for the presence of the lipid packing sensor motif ALPS, which is able to sense and bind poorly packed lipids, such as in the presence of highly curved domains or bilayers enriched in cone-shaped lipids. Indeed in both situations the activity of ArfGAP1 strongly increases (Bigay et al., 2005; Mesmin et al., 2007). By contrast, both ArfGAP2 and ArfGAP3 lack the ALPS motives and their activity is not modulated by either membrane curvature or lipid composition, but strictly depends on coatomer binding. Indeed, a lysine-rich stretch in the middle of the ArfGAP2/3 was identified as a critical determinant for COPI binding and regulation of GAP activity (Kliouchnikov et al., 2009). Due to these different features, different functions of the three ArfGAPs have been proposed. Because of its curvature-dependent activity and the fact that coated vesicles are highly curved domains, ArfGAP1 seems to be a general terminator of Arf1 activity, while the role of ArfGAP2/3 seems to be tightly involved in the COPI mechanism, because their GAP activity depends on coatomer binding: whether these ArfGAPs act as a coat components or their function is primarily related to the regulation of GTP hydrolysis is still unknown.

1.4 Signals for COPI and COPII-dependent transport

1.4.1 ER-export signals

Experimental studies have proposed two different non-exclusive models for the exit of cargo proteins from the ER, the signal-mediated recruitment and the bulk flow hypothesis (Fig. 5). The bulk flow process is the passive, sequence-independent process by which cargoes stochastically enter into transport vesicle without any positive selection. This type of transport appears to operate in the export of some secretory proteins, such as amylase and chymotripsinogen, from the ER of pancreatic exocrine cells (Martinez-Menarguez et al., 1999; Wieland et al., 1987).

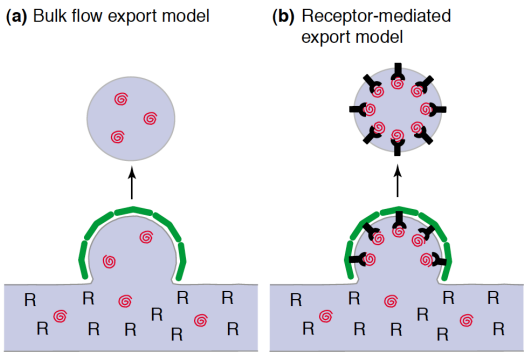

Figure 5: Bulk flow and receptor-mediated hypothesis for export secretory proteins out of the ER (Barlowe, 2003)

Despite the existence of bulk flow transport, most proteins seems to be actively recruited at the ERES and possesses a binding affinity for key components of the coat. More specifically, the molecules constituting the "pre-budding complex" (see above) can be isolated bound to cargoes under conditions that preserve the Sar1-GTP configuration (Aridor et al., 1998; Kuehn et al., 1998). Based on these findings, it has been hypothesized that secretory proteins contain sequence motives that can be recognized, either directly or indirectly, by the pre-budding complex. Indeed, many studies have identified specific ER-export signals on different transmembrane cargoes as well as on transmembrane receptors that drive the export of soluble proteins that cannot be bound directly by the COPII complex (Table 1).

Export signal	Protein
Di-acidic motifs	
IYTDIEMNRLGK (−1)	VSV-G
ANSFCYENEVAL (−45)	Kir2.1
QSPIQLKDLESQI (−1)	Sys1p
AEKMDIDTGR (−34)	Gap1p
Di-hydrophobic motifs	
YIMYRSQQEAAAKKFF (−1)	ERGIC53
YYMFRINQDIKKVKLL (−1)	Emp46p
YLRRFFKAKKLIE (−1)	p24δ1
YQPDDKTKGILDR (−1)	Erv41p
KLFYKAQRSIWGKKSQ (−1)	Erv46p

Table 1: Characterized ER export signals (modified from Barlowe 2003)

The best-characterized export signal is represented by the di-acidic motif (DxE) in the cytoplasmic C-terminal tail of VSV-G, a type I transmembrane protein widely used as model to study the secretory pathway (Nishimura and Balch, 1997). Deletion of one of the aminoacids in the consensus sequence causes a slower export rate, while the addition of DxE to other transmembrane cargoes strongly improves their transport

rate (Sevier et al., 2000). This motif has been also identified in other exported proteins, such as the Kir2.1 potassium channel (Ma et al., 2001) and the yeast proteins Sys1 and Gap1 (Malkus et al., 2002; Votsmeier and Gallwitz, 2001). However, there are many other transmembrane cargoes that do not contain the di-acidic sequence and are efficiently transport out of the ER. Indeed, other export motives have been discovered and they generally consist of a pair of bulky hydrophobic residues (Barlowe, 2003). For example, ERGIC53, a type I transmembrane protein that cycles between the ER and Golgi apparatus, has a pair of conserved aromatic residues in its cytoplasmic tail that bind COPII and that are necessary for ER export (Kappeler et al., 1997). Other di-aromatic motifs (FF, YY, FY) have been found in similar positions in members of the p24 family (Dominguez et al., 1998) and in the Erv41-Erv46 complex (Otte and Barlowe, 2002). Concerning the export of soluble secretory proteins, beyond the bulk flow mechanism, a receptor-mediated mechanism has been demonstrated; in this case, a transmembrane cargo receptor links a soluble protein inside the ER lumen to the cytosolically exposed coat by binding, on one side, luminal cargoes and, on the other side, COPII through the already mentioned export sequences. Indeed, most of the proteins in which the export signal has been identified act as transport receptors. ERGIC53 mediates the exit from the ER of a subset of soluble glycoproteins including blood coagulation factors V and VII and cathepsin-Z (Appenzeller et al., 1999), while the p24 family is required for the efficient export of some GPI-anchored proteins (Takida et al., 2008).

Despite the fact that some papers reported the ability of activated Sar1 to bind some ER export signals (Aridor et al., 1998), Sec24 seems to be the most important regulator of cargo recognition. The genome of higher eukaryotes encodes at least four different Sec24 isoforms (Sec24A-D) (Pagano et al., 1999) and this has been proposed to explain the wide range of secretory proteins with different export motives that can be packaged into COPII-coated vesicles. Indeed, structural studies demonstrated a non-overlapping selectivity of the two classes of Sec24, Sec24A-B and Sec24C-D; Mancias and Goldberg (2008) reported that the F/IxM sequence binds a surface groove only of Sec24C and D and not the Sec24A and B isoforms. Conversely, the LxxLE class of transport signals, as well as DxE signal, are selectively bound by Sec24A and B (Mancias and Goldberg, 2008).

Recently two other receptors have been found to be important for the export of secretory proteins. The integral membrane protein TANGO1 is located at the ERES,

acts as bridge between the unusual large cargo collagen VII and the pre-budding complex Sec23/24-Sar1 and its knockdown strongly impaired collagen secretion (Saito et al., 2009). Another unconventional cargo receptor, Erv14, has been recently identified in yeast by combining genetic manipulation of yeast with high-throughput microscopy, termed "PAIRS" (Pairing Analysis of Cargo Receptors). It has been suggested that Erv14 does not facilitate the export of transmembrane cargoes by the recognition of a specific export motif, but through the binding of the TMD independently from their sequence (Herzig et al., 2012).

1.4.2 Retrograde sorting signals and receptors

The COPI retrograde pathway recycles not only the COPII anterograde machinery, but is also critical to retrieve escaped ER resident proteins through the action of retrograde sorting receptors, which bind specific retention motives on cargoes (Dancourt and Barlowe, 2010). Indeed, two possible mechanisms to maintain correct protein localization have been identified, retention or retrieval. The retention mechanism is the active exclusion of proteins from recruitment into transport carriers, while retrieval means that proteins can be included into transport carriers by bulk flow mechanism and then they are actively recycled back to the correct compartment through a receptor-mediated mechanism.

As in the case of COPII-dependent transport, ER resident membrane proteins usually bear a retention motif and are directly bound by COPI, while soluble proteins are recognized by specific receptors that link cargoes to COPI complex. Two different retrieval motifs have been identified in the cytoplasmic tail of membrane proteins, the di-lysine motif KKxx and di-arginine motif RxR. While the specific subunit of COPI that binds RxR-bearing-cargo is still unknown, the KKxx signal is recognized by WD40 domains of either the α or β' subunit (Michelsen et al., 2005; Shikano and Li, 2003). Concerning soluble proteins, the most characterized retention mechanism is represented by the KDEL signal, or related sequences, at the C-terminus of soluble ER-resident proteins, which is recognized by the KDEL receptor in the ERGIC or Golgi compartments and recycled back to the ER in COPI-coated vesicles. On the

other side, the KDEL receptor can bind COPI through a di-Lysine motif. It is unclear how the KDEL receptor can bind COPI only when it already makes contact with cargoes, but it is generally thought that the presence of ligand induces some conformational changes on its cytoplasmic residues, which trigger uptake into COPI vesicles (Aoe et al., 1998). Since the secretory pathway displays a pH gradient of increasing acidity from the ER to the Golgi and the optimal binding affinity of the KDEL receptor with its ligands is at pH 5-5.5, once the receptor reaches the ER, the luminal neutral pH induces release of cargoes.

In addition to the KDEL receptor, another important retrograde sorting receptor is Rer1, a tetraspanning membrane protein that recognizes a subset of ER membrane proteins for COPI-dependent retrieval from the Golgi/ERGIC back to the ER (Sato et al., 2003b). Similarly to the KDEL receptor, it can rapidly recycle because of a di-Lysine motif in its C-terminal tail and it is required for a correct ER localization of numerous proteins including Sec12, Sec63, Sec71 and Mns1 (Massaad et al., 1999; Sato et al., 1996). Interestingly, human Rer1 has been implicated in the regulation of γ-secretase activity by binding directly unassembled subunits of the γ-secretase complex at the Golgi apparatus and retrieving them to ER; thus only the properly assembled complex can proceed from the Golgi to the PM, where it participates in processing of the amyloid precursor protein and of Notch (Kaether et al., 2007). Concerning the molecular basis for recognition of transmembrane sorting motives, mutational analysis revealed that Rer1 binds a pair of polar residues that must flank a hydrophobic cluster of 6-7 aminoacids. However, single mutation in the fourth transmembrane segment of Rer1 impaired retrograde transport of some but not all cargoes, suggesting that Rer1 makes contact with its cargoes through at least two different mechanisms (Sato et al., 2003b).

Beyond the COPI-dependent route, another Golgi-ER retrograde pathway has been identified. This pathway can be used by some cargoes that lack retention motives, such as Shiga and Shiga-like toxins, to reach the ER from the plasma membrane via the Golgi apparatus (Sannerud et al., 2003). The ER targeting represents a crucial step for these toxins to be properly processed and to exploit their toxic action in the cytosol. White and colleagues demonstrated that Rab6-positive transport carriers are separated from COPI-positive components and that Shiga toxin retrograde transport is not inhibited upon the microinjection of anti-EAGE antibodies, potent inhibitors of

COPI function in live cells (White et al., 1999). It has also been demonstrated that Rab6 mediates vesicular Golgi-ER transport along microtubules. Indeed, one of the interacting partners of Rab6 is Bicaudal D1, a dynein-dynactin-binding protein, whose overexpression increases the recruitment of dynein on Rab6-positive structures; furthermore, a truncated form of Bicaudal D1, which is still able to bind Rab6 but not dynein, inhibits microtubule minus-end directed movements of Rab6 transport vesicles (Matanis et al., 2002). Even though it's not completely understood, it has been suggested that this alternative retrograde route is used not only by toxin proteins, but also by endogenous cellular proteins, such as Golgi enzymes, which lack a retrieval motif but continuously cycle to the ER via a COPI-independent pathway (Girod et al., 1999).

Another different retrograde route has been identified for two Golgi proteins that are responsible for the generating and maintaining the Golgi structure and architecture, the so called Golgi matrix proteins. It has been demonstrated that the two *cis*-Golgi proteins GM130 and GRASP65 cycle back to the Intermediate Compartment (IC) through specialized membrane tubules that physically interconnect the two compartments, allowing a very rapid exchange between them. Even though the co-localization with COPI has been observed within these tubules, the molecular machinery operating in this pathway is still unknown (Marra et al., 2001).

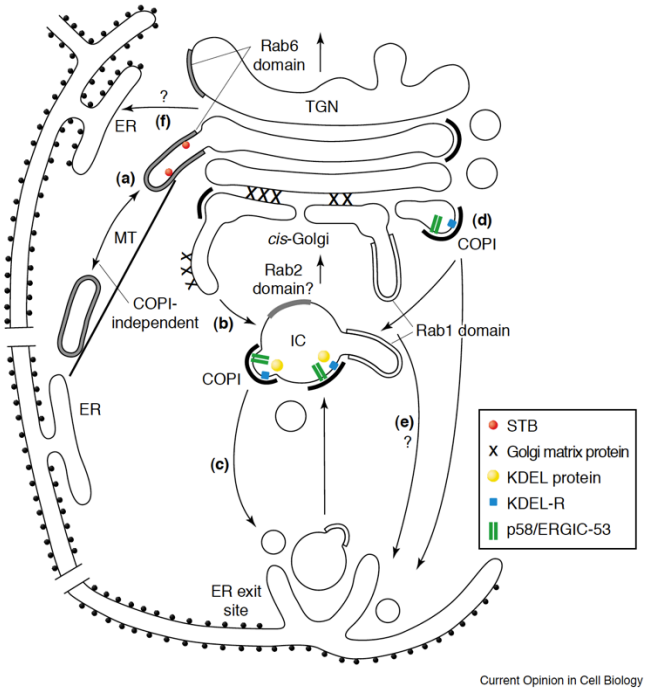

Figure 6: Working model depicting the different retrograde routes at the Golgi/ER interface (Sannerud et al., 2003).

1.5 Role of lipids in protein trafficking

As already described, eukaryotic cells have different intracellular compartments, where specialized metabolic reactions take place. Each organelle is enveloped by a unique lipid bilayer, in term of lipid composition, which provides both structural and signaling properties required for organelle-specific function.

In the context of the secretory pathway, lipids and lipid transport are strictly interconnected to protein transport. On the one hand, lipids use, in addition to local metabolism, the same molecular machinery to reach their final membrane destination by vesicular transport and, on the other hand, they can influence the transport of proteins through the interaction with specific membrane-spanning proteins both by the inclusion/exclusion of them into transport vesicles and by activating specific signaling events. In addition to this mechanism, as I will describe later, lipids can also be transported as single molecules through the action of cytosolic specific transporters (Sprong et al., 2001a).

In this chapter, I will describe the unique molecular composition of each membrane-bound compartment along the exo-endocytic pathways and the role of lipid microdomains in protein trafficking.

1.5.1 Lipid composition along the secretory pathway and lipid transport

The most abundant lipids in eukaryotic membranes are the glycerophospholipids, which they are composed by diacylglycerol (DAG) and a phosphate group (phosphatidic acid, PA) that can be esterified to either a choline (forming PtdCho), ethanolamine (forming PtdEtn), serine (forming PtdSer) or inositol (forming PtdIns). PtdIns can be phosphorylated in different positions within their polar head, giving rise to a big variety of PtdIns species within the cell, which mark specific cellular membranes and play a fundamental role in membrane traffic (De Matteis and Godi, 2004). In contrast, sphingolipids contain a ceramide backbone (consisting of a sphingoid base linked to a fatty acid) conjugated to a variable group such as a sugar group in the case

of glycosphingolipid, or to choline in the case of sphingomyelin, the most abundant sphingolipids of eukaryotic cells. Breakdown products of these two lipid species serve as lipid second messengers and they include PA, DAG, lysoPA, Cer-1-phosphate, Cer and sphingosin-1-phosphate (van Meer et al., 2008).

Another important class of lipids in eukaryotic cells is represented by sterols, where cholesterol is the most abundant sterols in eukaryotic cells and which are defined by the presence of a planar and rigid tetracyclic ring (Sprong et al., 2001b).

The main lipid biosynthetic organelle is the Endoplasmic Reticulum, which produces the bulk of structural phospholipids and cholesterol as well as ceramide, which is the precursor for complex sphingolipids. PtdCho is most abundant lipid of the ER membranes and represents about 60% of total ER lipids. The other two abundant ER lipids are PtdEtn and PtdIns, which represent about 30% and 15% of total ER lipids, respectively. Although they are synthesized in the ER, ceramide and cholesterol are quickly transported out of the ER and represent about 5% of total ER lipids (Fig. 7). Due to its low content of cholesterol and sphingolipids, the ER membrane is the thinnest and least rigid bilayer within the secretory pathway, with a thickness of the hydrophobic core of about 2,5 - 2,6 nm (Sharpe et al., 2010). Significant levels of lipid synthesis can also occur in the Golgi complex, which is specialized in sphingomyelin and complex glycosphingolipid synthesis as well as PtdCho and PtdEtn. The major lipids of the Golgi membranes are still PtdCho and PtdEtn, even though their levels are less than those of the ER, but they have increased levels of SM and cholesterol, giving rise to a thicker and more rigid bilayer (Fig. 7). The peculiarity of Golgi membranes is represented by the fact that their composition is not homogenous, but shows a gradient from the *cis*-Golgi to the *trans*-Golgi cisternae, with the *cis* face similar to the ER and the *trans* face similar to the composition of the downstream compartments (Sprong et al., 2001a). Indeed, the plasma membrane is particularly enriched in sphingolipids and sterols and shows the highest cholesterol/phospholipid ratio within the cell. Since cholesterol and sphingolipid can be packed with a higher density than glycerophospholipids, they form a thick and very rigid bilayer that makes the plasma membrane competent to resist mechanical stress coming from the extracellular environment (Fig. 7).

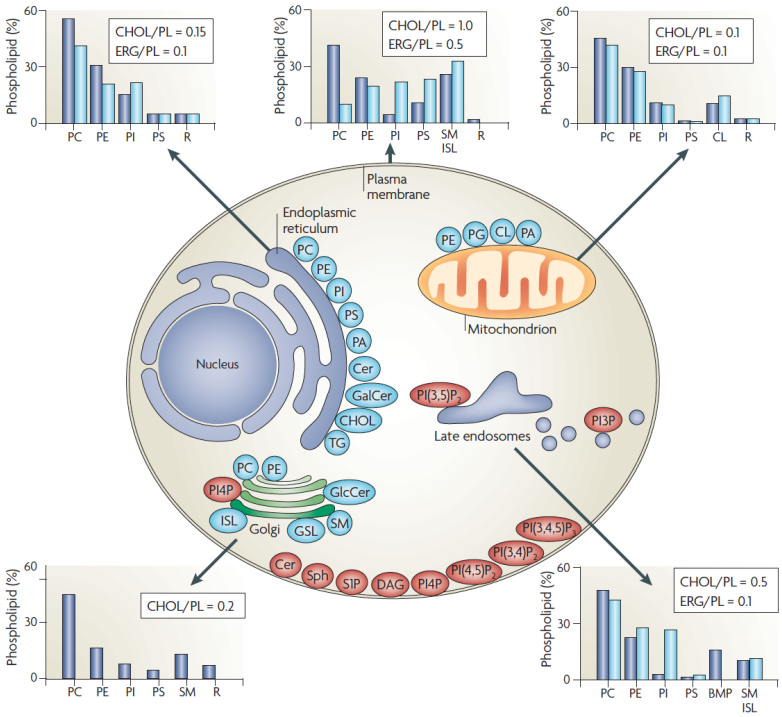

Figure 7: lipid synthesis and steady-state composition of cellular membranes: blue indicates the site of synthesis, while in red are shown lipids involved in signaling and organelle recognition pathways (van Meer et al., 2008).

An important issue that many research groups are trying to address is how eukaryotic cells maintains the unique lipid composition of its different intracellular compartments; once lipids are synthesized in the ER or in the Golgi apparatus, they need to reach their final destination. In particular, endosomes and plasma membrane do not contain any enzyme required for lipid synthesis and they totally depend on ER and Golgi as sources of lipids. Till now, two different mechanisms of lipid transport have been identified. Lipids can be included in the same transport vesicles that are responsible for protein trafficking and reach, together with protein cargoes, their final destination. The progressive enrichment of sterols and sphingolipids along the secretory pathway implies a selective inclusion/exclusion of specific lipids from anterograde or retrograde transport carriers. Therefore, different lipids can segregate into microdomains within the same membrane. Since membrane proteins can preferentially interact with specific lipid species, the formation of these lipid microdomains can determine protein recruitment or exclusion into vesicles, representing in this way an important factor that can influence trafficking along the secretory pathway (see paragraph below) (Simons and Sampaio, 2011).

Lipids that are synthesized on the cytosolic leaflet of the ER, such as PtdIns, can be also transported to the specific acceptor membrane as single molecules by the action of cytosolic proteins. These lipid-exchange proteins contain on one side a hydrophobic pocket that serves as a binding domain for lipids and, on the other side, a protein interaction domain that bridges the donor and acceptor membranes creating a contact site that allows lipid exchange (Voelker, 2005).

1.5.2 Lipid microdomains

Our view of biological membranes has evolved dramatically over the last few decades and evidence on the role of lipids in controlling cellular events are constantly increasing. In the classical bilayer model of Singer and Nicolson (Singer and Nicolson, 1972), termed "fluid mosaic model", both proteins and lipids freely diffuse within the plane of the membrane. In the 90s, the discovery of detergent-resistant membranes, the so called "lipid rafts", suggested the possibility of sterol-dependent sphingolipid and protein associations within cell membranes and completely changed our view of biological membranes. This concept was first introduced to explain the generation of the glycolipid-rich apical membrane of epithelial cells; these membrane domains are characterized by resistance to cold detergent extraction (Simons and van Meer, 1988). This and other studies on artificial model membranes led to the conclusion that lipids can coexist in two different phases in the plane of the bilayer: liquid-ordered and liquid-disordered phases. In the liquid-disordered phase, lipids containing unsaturated acyl chains are poorly packed in the planar bilayer, due to the disordered fatty acid structures of glycerophospholipids, and they have a high lateral mobility, while the liquid-ordered phase is characterized by the high order of a solid but the high lateral mobility of a liquid. This ordered phase exists mainly in the presence of sphingolipids that possess long and saturated acyl chains and cholesterol, which, together, participate in packing lipids close to each other (van Meer et al., 2008).

Presently, this working model has been modified and lipid rafts are not seen any more as micrometer-scale stable platforms, in which specific lipids and proteins are segregated, but they are defined as dynamic nano-scale, sphingolipid-enriched, ordered assemblies of specific proteins that can be activated to coalesce by specific li-

pid-lipid, lipid-protein and protein-protein interactions (Lingwood and Simons, 2010). The real spatial characteristics and dynamics of these microdomains are still debated and different models strongly depend on the methodologies that are used. For instance, fluorescence correlation spectroscopy studies revealed the existence of 120 nm structures that fluctuate on a sub-second time scale (Lenne et al., 2006), while high spatial and temporal resolution fluorescence energy transfer estimated more stable domains of about 10 nm (Goswami et al., 2008). What is nowadays generally accepted, is that the fluctuating nano-scale assemblies can be functionalized by different stimuli (protein oligomerization, presence of palmitoylated proteins or the interaction with cortical actin) that trigger the coalescence of membrane order-forming lipids, leading to the "raft phase", in which these domains can merge to each other and reach a more stable state of micro scale size and where "raftophilic" and "non-raftophilic" membrane constituents are laterally segregated from each other (Simons and Sampaio, 2011) (Fig. 8).

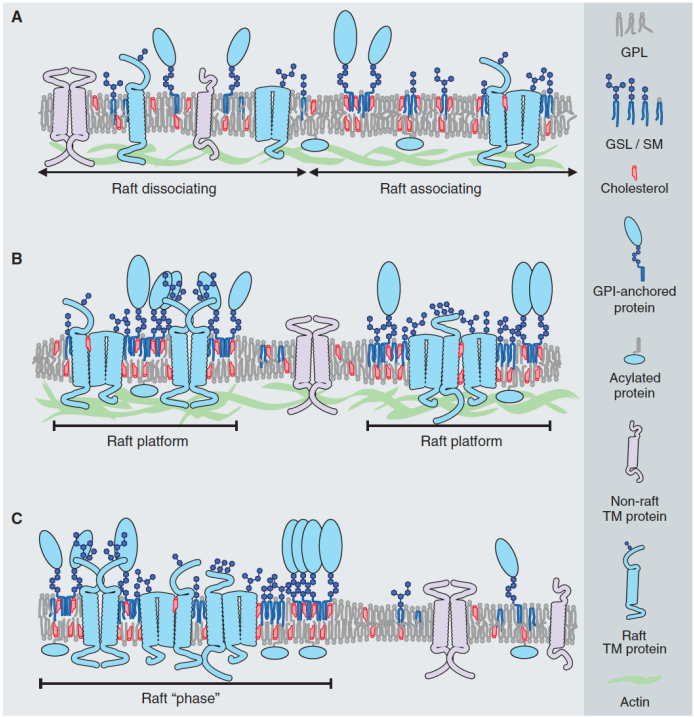

Figure 8: scheme of lipid raft assemblies in cellular membranes (Lingwood and Simons, 2010).

Most of the above-mentioned studies concern the plasma membrane and the *trans*-Golgi, where it has been demonstrated that their lipid composition, at physiological temperature, is close to a critical miscibility point, in which the two phases co-

exist and fluctuate in a metastable state as already described. From an evolutionary point of view, this situation gives a great advantage because the raft assembling and the formation of the "raft phase" can be achieved with a little energy cost, such as occurs for protein oligomerization (Simons and Sampaio, 2011).

In contrast, the other intracellular membranes, because of their lower cholesterol content, are expected to assume a homogenous liquid-disordered phase and till now, no demonstrations of the presence of rafts have emerged. Nonetheless, there are a growing number of indications that specific lipids are crucial factors in vesicular transport along the entire secretory pathway. Many papers have reported the importance of PtdIns in many steps along the exo-endocytic pathway: PtdIns(4,5)P_2 participates in the invagination of clathrin coated pits at the plasma membrane, while PtdIns(3)P, which is exclusively distributed in early endosomes, is important for multiple endocytic steps, including docking, fusion and motility of endosomes (De Matteis and Godi, 2004). The presence of specific lipids seems to be important also in the early steps of the secretory pathway, at the ER/Golgi interface. COPI-coated vesicles are depleted of both cholesterol and sphingomyelin (Brugger et al., 2000), while the presence of diacylglycerol is required for the formation of COPI vesicles and for a correct Golgi to ER transport (Fernandez-Ulibarri et al., 2007).

Concerning the anterograde transport from the ER to the Golgi, a few have reported the requirement of cholesterol for the transport of some membrane proteins. Indeed, acute treatment with statins, which inhibit cholesterol synthesis, or with cyclodextrins, which remove cholesterol from membranes, cause an impairment in the COPII-dependent transport of VSV-G, scavenger receptor-A and of the GPI-anchored protein, CD59 (Bonnon et al., 2010; Ridsdale et al., 2006; Runz et al., 2006). Reduced cholesterol levels cause both a decrease in the lateral mobility of membrane proteins and a delay in the turnover of the COPII component Sec23. Cholesterol doesn't seem to be the only lipid involved in transport from the ER; Pathre and colleagues demonstrated that the activation of phospholipase D (which catalyzes the formation of phosphatidic acid) by Sar1 supports membrane tubulation during exit site formation and facilitates cargo export (Pathre et al., 2003). Indeed, treatment with an inhibitor of the lysophospholipid acyltransferase (which promotes the formation of phosphatidic acid from lysophosphatidic acid) affects the exit of cargoes from the ER and the formation of COPII vesicles *in vitro* (Brown et al., 2008). Also ceramide has been suggested to play a role in COPII-dependent transport; treatment with PDMP, which blocks the

sphingolipid synthesis pathway by inhibiting the conversion of ceramide into sphingomyelin and glucosylceramide and causes an accumulation of ceramide, significantly delayed the transport of VSV-G and retained the M glycoprotein of Infectious Bronchitis Virus into the ER (Maceyka and Machamer, 1997).

All this evidence clearly indicates the fundamental role that lipids play in controlling protein function and localization and how lipid and protein sorting and transport are intrinsically linked.

1.6 Membrane curvature

In addition to lipid domains, cells also display different morphological domains that differ in membrane curvature or bending (Fig. 9). Highly curved regions are of particular importance during vesicle trafficking, as the budding of a vesicle means the formation of different domains with both "positive" and "negative" curvature (where positive indicates regions of membrane that curve inwards the cytoplasm and negative regions that curve in the opposite direction).

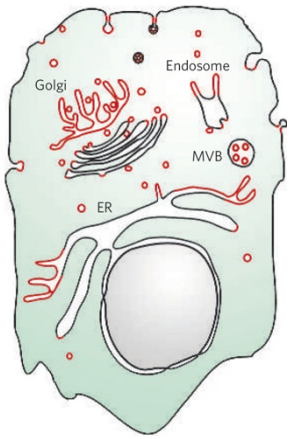

Figure 9: regions of high curvature within cellular membranes (McMahon and Gallop, 2005)

Moreover, some intracellular organelles have specialized regions characterized by high curvature, such as peripheral ER tubules, Golgi tubules that connect different cisternae within a Golgi stack and the plasma membrane protrusion during cell migration. Frequently, areas of high membrane curvature exist for only limited period of

time and, in the context of protein trafficking, it's quite intuitive that dynamic changes should be important for proper transport; in vesicles bending is primarily induced by the coat proteins, but then, after the uncoating event, the curvature is no longer stabilized and the vesicle becomes more fusogenic as while the coat proteins can be reused for another round of vesicle formation. Five different mechanisms have been identified to generate curved domains, which are not mutually exclusive, but probably cooperate to bend a membrane (Farsad and De Camilli, 2003; McMahon and Gallop, 2005) (Fig. 10).

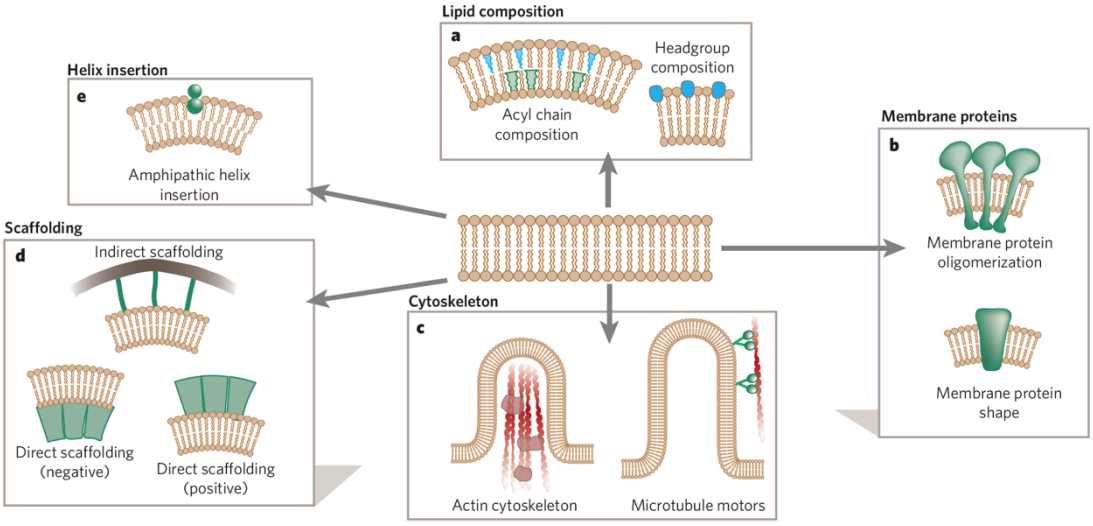

Figure 10: mechanisms of membrane deformation (McMahon and Gallop, 2005).

One of the most studied mechanism to induce membrane deformation and that is strictly linked to lipid rafts involves the presence of specific lipid species that have a permissive role in membrane curvature because of their shape or chemical properties. For example, cone-shaped lipids with small polar heads and a bigger hydrophobic part, like PtdEtn, or lipids with an inverted cone shape (where the acyl chains occupy a smaller surface than the headgroup, like lysophosphatidic acid or phosphatidic acid) can favour positive or negative curvature, respectively (Sprong et al., 2001b). Indeed, as I already mentioned, phosphatidic acid has been proposed to assist the formation of COPII-coated vesicle at the ERES (Brown et al., 2008). Also cholesterol has been proposed to be important in generating highly curved regions by two possible mechanisms: first, a selective enrichment of cholesterol in one leaflet of the bilayer could alter and increase the relative surface of the bilayer acting as a lipid "reservoir" only on one leaflet to favour budding and second, it might intercalate into the

budding-site leaflet to reduce hydrophobic-hydrophilic interactions during the distortion of the bilayer and, in this way, the energy needed for budding (Baba et al., 2001).

As well as assisting or antagonizing curvature, lipids can even form domains in response to curvature that they prefer. Using a ternary lipid mixture close to the demixing point and composed of sphingomyelin, cholesterol and PtdCho, Roux and colleagues demonstrated that lipids of the liquid-disordered phase are selectively partitioned into curved domains, while those of the liquid-ordered phase are excluded (Roux et al., 2005). Indeed, COPI is able to bind membranes and form a coat only on liquid-disordered domains, where the membrane tension is low and, therefore, the energy cost to bend the membrane is small (Manneville et al., 2008).

A second mechanism of membrane bending is represented by integral membrane proteins. For simple geometric reasons, transmembrane proteins with a conical shape, like the TMD of the nicotinic acetylcholine receptor, naturally prefer curved regions and, in turn, themselves could facilitate membrane deformation in a way similar to the cone-shaped lipids. The Reticulon family, of which Rtn4 is the most studied member, represents an important example of membrane proteins that are responsible for generating and maintaining highly curved regions, the ER tubules. Reticulons contain two hydrophobic segments that insert into the cytosolic leaflet of the ER membrane adopting a wedge shape; thereby, they increase the surface area only on the outer leaflet of the bilayer and, similar to cone shape lipids, facilitate membrane tubulation (Voeltz et al., 2006) (Fig. 11).

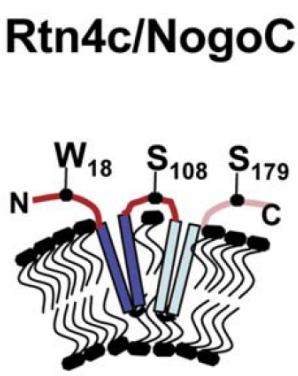

Figure 11: membrane topology of Reticulon4 (Voeltz et al., 2006).

Cytoskeletal assembly and disassembly is intimately linked to membrane-shape changes of both plasma membrane and intracellular organelles. Remodeling of actin filaments is involved in the generation of many areas of high membrane curvature

during cell migration like filopodia and axonal growth cones. It is still poorly understood whether actin is directly able to drive membrane curvature, but it is generally accepted that the cytoskeleton can promote the generation of local curvature. Indeed, actin polymerization has been implicated in some endocytic events. For example, actin nucleation alone is able to mediate the scission of Shiga toxin-induced tubular invaginations of the plasma membrane in a way that is independent from both clathrin and dynamin (Romer et al., 2010). It has also been demonstrated that the microtubule network can, at least *in vitro*, pull out tubules from intracellular membranes by the action of molecular motors (Roux et al., 2005); thus, it is very likely that motors might be partly responsible for tubulated organelle morphology.

Another class of proteins that can bend membranes is represented by cytosolic proteins that, upon specific modifications, are capable to bind membranes and constrain membrane topology into a tubular shape. BAR domains (banana-shaped lipid binding domains) are found in a wide variety of trafficking proteins (i.e. dynamin), and they bind preferentially to curved regions through their concave shape. After their membrane binding, they are also able to polymerize and lead to membrane tubulation (at least in *in vitro* assays). Like BAR domains, coat proteins can also bind to membrane and trigger membrane bending by polymerizing into curved structures (Antonny et al., 2003) (see section 1.2).

The fifth identified mechanism is based on the action of a different class of proteins that contain amphipatic helices with hydrophobic residues on one side of the helix and hydrophilic residues on the other one.

The most studied member of this family is ArfGAP1, which triggers GTP hydrolysis of Arf1 during COPI-coated vesicle budding in the Golgi apparatus (Antonny, 2011). Like BAR domains, the ALPS domain (Amphipatic Lipid Packing Sensor) of ArfGAP1 can sense and bind highly curved domains or flat membranes enriched in lipids with small polar heads and unsaturated acyl chains; in both situations lipids are not tightly packed and, therefore, the amphipatic helix can be inserted into the small space between lipids (Fig. 12).

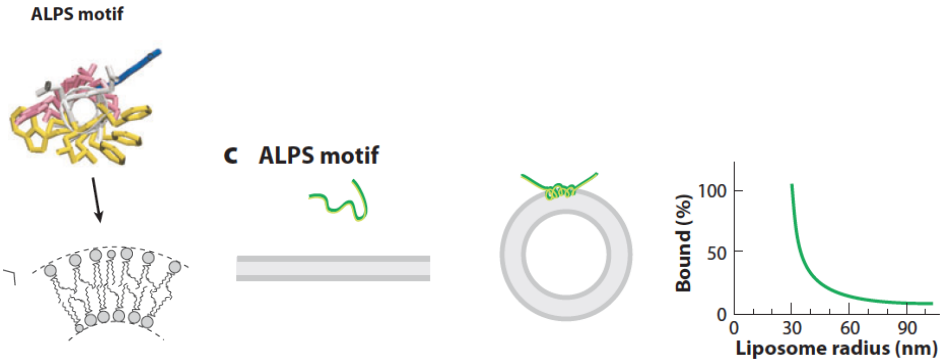

Figure 12: ALPS motif can sense a lipid packing defect typically present on curved domains (modified from (Antonny, 2011).

1.7 The TMD-dependent transport

As described in the section 1.3 of this chapter, one factor that strongly determines the retention in or exit from the ER is the ER export signal. But other factors influencing protein transport along the secretory pathway have been identified. Among them, the physico-chemical features of the TMD of membrane protein cargoes are one of the most important. One fundamental principle of membrane-spanning protein-lipid interaction is based on the fact that non-permissive hydrophobic-hydrophilic interactions must be avoided; therefore, the length of the TMD must match the thickness of the hydrophobic core of the bilayer. In other words, the sequences of TMDs should reflect the physical properties of the bilayers in which they reside (Sharpe et al., 2010). Since membranes along the secretory pathway display a progressive increase in thickness and rigidity of the bilayer, proteins that are distributed in different intracellular organelles and at the plasma membrane should have different TMD length. Indeed, this paradigm has been recently confirmed by a bioinformatic analysis from a large scale dataset from fungi to vertebrates on the correlation between TMD length of membrane proteins and their intracellular localization (Sharpe et al., 2010). The authors found that TMDs have organelle-specific properties with a dichotomy in TMD length between the early and late parts of the secretory pathway; ER and Golgi resident proteins have a mean TMD length of 19-20 aa, while proteins localized in the TGN, endosomes and plasma membrane have longer TMDs of 24-25 aa (Fig. 13).

Experimentally, many examples of TMD-dependent sorting have been observed essentially throughout the entire secretory pathway (Bulbarelli et al., 2002; Nufer et al., 2003; Sato et al., 2003a; Schamel et al., 2003).

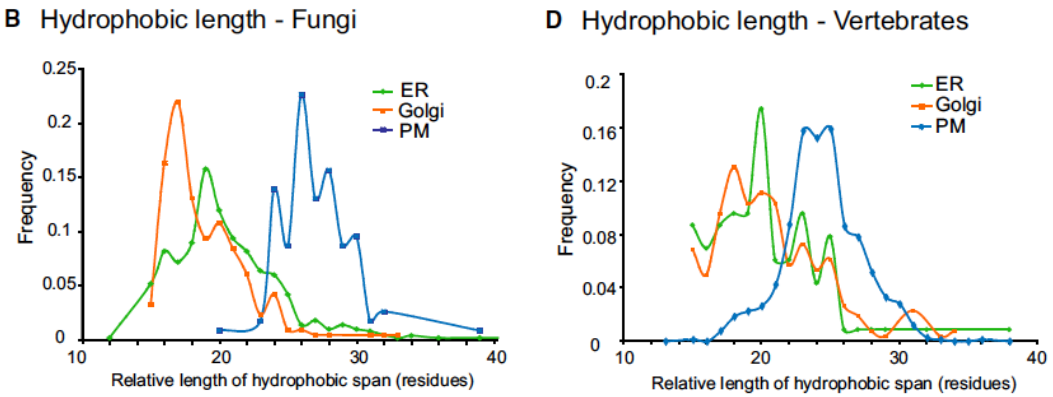

Mean hydrophobic lengths (residues)

	ER	Golgi	TGN/endo	PM	apical	basolat.
Fungi	20.6	19.2	23.6	27.0		
Vertebrates	20.3	20.6	24.8	24.4	24.0	24.8

Figure 13: TMD length distribution of fungi and vertebrates membrane proteins localized in the ER, Golgi and plasma membrane (Sharpe et al., 2010).

The TMD-dependent sorting was first demonstrated to explain the retention of Golgi enzymes in the Golgi apparatus (Munro, 1991). Indeed, the author found that the TMD of the Golgi enzyme α-2,6-sialyltransferase is the major determinant for its correct localization in the Golgi apparatus and he also hypothesized that a lipid-based sorting could be the mechanism by which Golgi enzymes are excluded from antero-grade vesicles and from transport to the plasma membrane (Munro, 1995). Subse-quently, our group demonstrated how this event is fundamental at the ER/Golgi inter-face by using C-tail-anchored proteins as model proteins (see below) (Pedrazzini et al., 1996).

1.7.1 C-tail-anchored proteins as a model to study TMD-dependent transport

Since many years, our laboratory has been using C-tail anchored proteins as models to study mechanisms of post-translational insertion into membranes (see section 1.1) and TMD-dependent sorting. In particular we have been using rabbit cytochrome b5 ((cyt)b_5), which is a 15 kDa protein, with a globular heme-linked N-terminal domain, a short linker separating the functional domain from the membrane, 17 hydrophobic aminoacids spanning the ER bilayer and a short luminal polar sequence at the C-terminus. This protein is particularly abundant in the hepatocyte ER, where it acts as electron donor for a vast variety of acceptors involved in lipid metabolism (in association with NADH-cyt b5 reductase) and in xenobiotic detoxification (receiving electrons from NADPH-cyt P450 reductase) (Borgese et al., 1993; Borgese and Harris, 1993).

Thanks to their simple structure and to fact that they lack any export signal motif, TA proteins represent an excellent model to clearly observe the TMD-dependent sorting. By analyzing the mean hydrophobicity of differently localized mammalian TA proteins, we observed a clear progressive increase of the TMD length along the exocytic pathway and that ER resident TA proteins have a short TMD tail (Borgese et al., 2007) (Fig. 14).

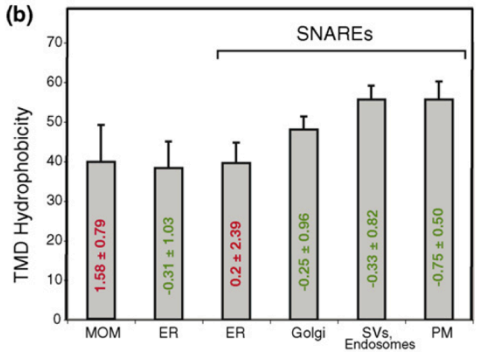

Figure 14: physicochemical features of the tail region of differently localized TA proteins. ER and MOM localized TA proteins display similar hydrophobicity, while SNARE proteins show a progressive increase of TMD length along the exo- endocytic route (Borgese et al., 2007)

Indeed, in 1996, our group experimentally demonstrated that the ER localization of (cyt)b_5 strictly depends on the length/hydrophobicity of its TMD; lengthening the membrane anchor to 22 residues causes the escape from the ER and its redistribution to the plasma membrane (by adding the hydrophobic sequence ILAAV).

This relocation does not depend on the aminoacid sequence that has been added, because restoring the length of 17 aa, but maintaining the ILAAV sequence does not alter the typical ER distribution of (cyt)b_5 (Pedrazzini et al., 1996). Moreover, the replacement of the N-terminal catalytic domain by GFP gave the same results regarding the importance of the TMD, thereby excluding the possibility of other topogenic determinants in the cytosolic domain (Bulbarelli et al., 2002) (Fig. 15).

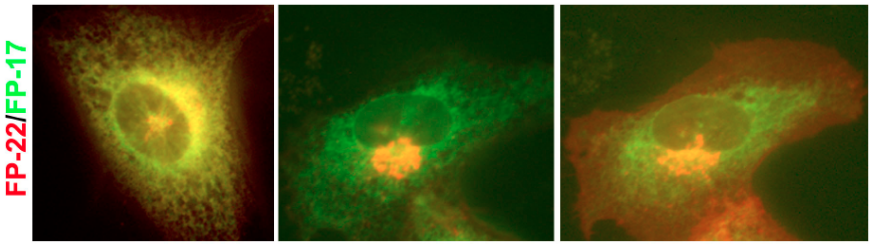

Figure 15: different intracellular distribution of FP-17 and FP-22; 1 h after cDNA microinjection (left picture) both FP-17 and FP-22 are localized in the ER. FP-17 remains distributed within the ER in all timepoints analyzed (90 min in the center and 150 min on the right). In contrast, FP-22 travels through the secretory pathway and 90 min after microinjection is localized in the Golgi (central picture) and after 150 min reaches the plasma membrane (right picture) (Ronchi et al., 2008).

1.7.2 Possible mechanisms for TMD-dependent sorting at the ER-Golgi interface

Nevertheless the mechanisms of ER retention of FP-17 and transport to the plasma membrane of FP-22 are still not fully understood. Concerning the residence in the ER, it has been demonstrated that a (cyt)b_5 version engineered to contain an *O*-glycosilation acceptor site close to the C-terminus is partially *O*-glycosylated, a process catalyzed by GalNAc transferases in the *cis*-Golgi, with a very slow rate (half time of 10 hours). This result suggests that only a small fraction can escape from the ER by a "bulk flow" mechanism and cycle between the ER and Golgi apparatus (Pedrazzini et al., 2000) and that the main mechanism keeping (cyt)b_5 in the ER might be exclusion from export (see below).

Indeed more recently, our group demonstrated that the two proteins are already partitioned into different domains when both are still distributed in the ER. The longer TMD is selectively enriched at the ERES and ER tubules (Rtn4A-positive structures), while FP-17 doesn't co-localize with the ERES marker Sec23 and is distributed in both ER tubules and sheets (Ronchi et al., 2008) (Fig. 16).

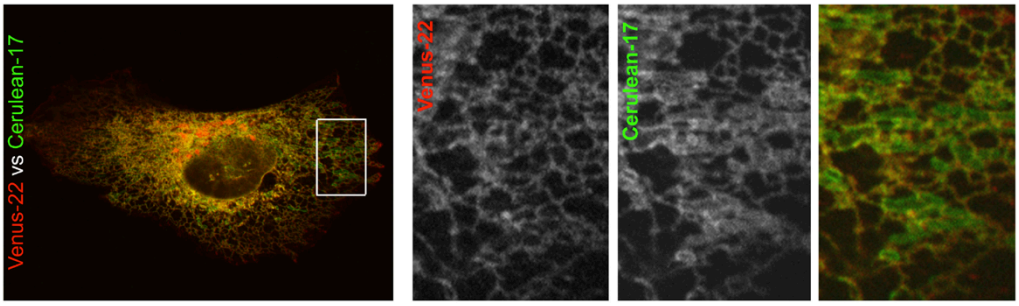

Figure 16: TMD-dependent partitioning of FP-17 and FP-22 into different ER domains. This panel shows a cell expressing both FP-17 and FP-22 1 h after cDNA microinjection; FP-22 (in red) is segregated in ER tubules, while FP-17 (in green) is localized in both ER tubules and sheets (Ronchi et al., 2008).

These findings led us to conclude that the vast majority of FP-17 is statically retained within the ER by a non-receptor-mediated and positive mechanism of exclusion from budding transport carriers.

Concerning FP-22, in addition to the segregation in ER tubules and ERES, we also demonstrated that its diffusion within the ER and from the ERES to the surrounding ER is higher than that of VSV-G, whose recruitment at the ERES is receptor-dependent. Therefore, it's difficult to explain either by bulk flow or receptor-mediated mechanisms how FP-22 can be excluded from the ER sheets, recruited to the ERES and diffuse both at the ERES and in the rest of the ER with the same rate. To explain these behaviors, two different, non-exclusive hypotheses have been formulated, based on the concept of the hydrophobic mismatch (Fig. 17). As described in section 1.7, transmembrane proteins need to match the length of the TMD with the thickness of the bilayer where they reside. But FP-22 is predicted to have a longer TMD than the thin ER membrane and it needs to find a way to accommodate the mismatch and to avoid the exposure of hydrophobic portions to a hydrophilic environment. Although ER membranes, because of their low cholesterol content, are predicted to have only a homogenous liquid-disordered phase, some evidence on the presence of specific microdomains enriched in "thicker" lipids has been reported (Bonnon et al., 2010; Ridsdale et al., 2006; Runz et al., 2006). Thus, FP-22 could segregate into specific

microdomains in which the lipid composition matches better its length/hydrophobicity. Indeed, it has already been demonstrated that the two form of (cyt)b_5 interact with different lipid species in reconstituted proteoliposomes and that the extended form prefers domains enriched in acidic phospholipids and ceramide, while the wild-type form is excluded from these domains (Ceppi et al., 2005).

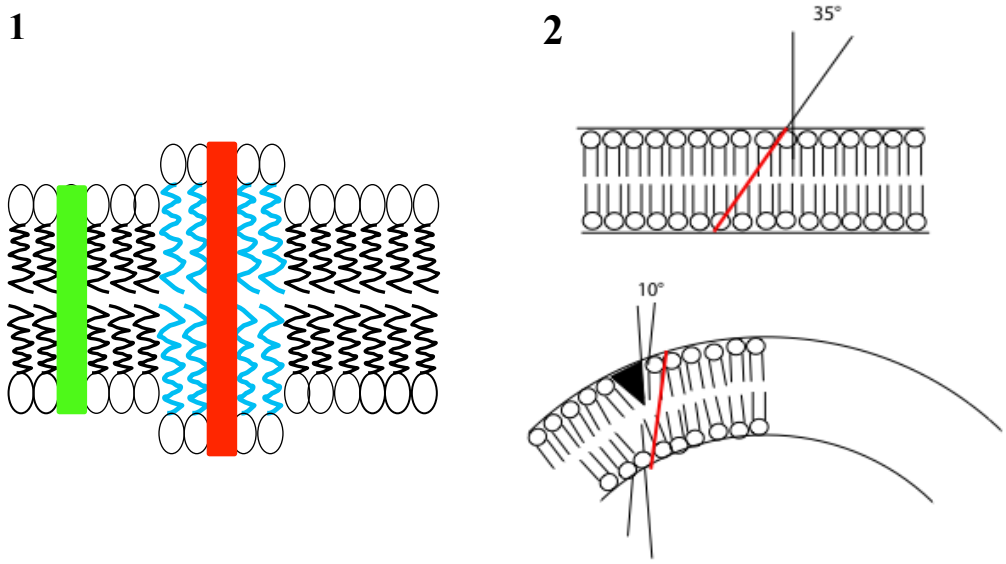

Figure 17: the lipid microdomain (1) and membrane curvature (2) hypothesis to explain the TMD-dependent partitioning of membrane proteins within the ER; in green is depicted the short TMD of FP-17, while in red the longer TMD of FP-22.

The second hypothesis is based on a simple geometrical consideration, taking into consideration the observation that FP-22 is segregated into curved ER domains (tubules and Exit Sites). One way to accommodate hydrophobic mismatch is by tilting of the TMD within the lipid bilayer (de Planque and Killian, 2003), but this results in a sub-optimal interaction between the TMD and the acyl chains of the bilayer. By contrast, in curved regions, FP-22's tilt might be compensated by tilting also of the acyl chains. Thus, the difference between the orientation of the acyl chains and of the TMD could be smaller, resulting in a more favorable interaction.

Another interesting point comes from the analysis of the transport rates of the sequence-dependent and the TMD-dependent (and sequence-independent) mechanisms by comparing the transport of FP-22 to that of VSV-G. This type I transmembrane protein is transported very efficiently to the plasma membrane and it contains a known di-acidic (DxE) export signal in its cytosolic tail (Balch et al., 1994). Our group demonstrated that VSV-G is strongly recruited at ERES compared to FP-22 and it's more efficiently transported to its final destination. Indeed, in 15 minutes the vast

majority of VSV-G leaves the ER and accumulates in the Golgi apparatus and in 45 minutes it is exclusively localized at the plasma membrane. In contrast, the TMD-dependent transport of FP-22 is less efficient: 120 minutes after its cDNA microinjection it is still distributed between the ER and the Golgi and 150 minutes after microinjection only a small amount of FP-22 reaches the plasma membrane. Therefore, the presence of the export signal in the cytosolic tail of VSV-G guarantees a faster and more efficient transport through the secretory pathway compared to that of cargoes that lack this export motif (Ronchi et al., 2008).

The crucial role of TMD length/hydrophobicity in protein trafficking and in particular at the ER-Golgi interface is not restricted to TA proteins, but other examples have been shown; one of the clearest reported case concerns the influence of the physicochemical TMD features of VSV-G. It has a predicted α-helix hydrophobic domain of 22-23 residues, which is similar to all other proteins localized at the plasma membrane (Fig. 12). The substitution of the di-acid motif with two alanines (AxA) does not block its arrival to the plasma membrane (even though its transport is significantly slowed down) thanks to the physical properties of its TMD. By contrast, Dukhovny and colleagues recently reported that when VSV-G TMD is shortened to 17 residues, a length that matches with the TMD length of ER resident proteins, the protein is no longer able to reach the plasma membrane and is blocked within the ER, even in the presence of the export signal (Dukhovny et al., 2009).

2. AIM OF THE THESIS

My PhD project is aimed at the identification of the molecular mechanisms responsible for transport of membrane proteins at the ER-Golgi interface. Since all the proteins that are localized at the plasma membrane or in different intracellular organelles need to be transported along the secretory pathway, the exo-endocytic route plays a fundamental cellular function and the understanding of its molecular mechanisms is of crucial importance. Considering that all ion channels and plasma membrane receptors are delivered to their destination via the exocytic pathway, the relevance of these mechanisms to basic pharmacology cannot be overstated. In this thesis we focused our attention on two crucial factors that influence protein transport: the presence of aminoacid export sequences and the physicochemical features of the TMD.

Our lab previously demonstrated that FP-17 and FP-22, which do not contain any export sequence in their cytosolic portion and that differ only for the length of the TMD, are differently segregated within the cell. FP-17 is actively retained in the ER and excluded from ERES, while FP-22 is recruited at ERES and transported along the secretory pathway to the plasma membrane. Even though it is enriched in transport carriers, its transport is significantly less efficient compared to that of a signal-bearing membrane protein, VSV-G. Therefore, we first investigated whether the different transport rates are only due to a differential recruitment at the ERES (demonstrated in (Ronchi et al., 2008)) or whether the di-acidic signal is crucial in other steps of the secretory pathway to guarantee an efficient transport. To this aim, we took advantage of the temperature blocks combined with live-cell imaging approaches to study the transport of our two model proteins in the different steps of the secretory pathway. Surprisingly, we found that the anterograde transport of FP-22 from the ER to the Golgi is fast and comparable to that of VSV-G, but it slowly reaches the plasma membrane because the vast majority, once arrives to the Golgi, is recycled back to the ER. This result suggests that recognition of the export sequence by a Golgi receptor might prevent VSV-G from futile recycling to the ER. In order to directly demonstrate the role of the export signal in the Golgi apparatus, we analyzed the behavior of

a mutant form of VSV-G, in which the DxE sequence has been replaced with two alanines (AxA).

As explained in the introduction, the second problem I investigated in my thesis concerns the mechanism of the TMD-dependent recruitment to ERES (Ronchi et al., 2008). FP-22 appears to be excluded from flat ER domains and segregated into curved domains. I asked whether membrane curvature could be a factor determining the recruitment of a hydrophobically mismatched TMD to ERES. To this aim, we used a simple *in vitro* model of membranes, in which the contribution of curvature alone can be easily studied. We reconstituted FP-17 and FP-22 into Giant Unilamellar Vesicles (GUVs) of micrometer size composed of either synthetic POPC (palmitoyl-oleyl-phosphatidylcholine) or ER lipids extracted from rat liver microsomes, and artificial highly curved nanotubes were pulled out using micromanipulation techniques, such as molecular motors and optical tweezers (Sens et al., 2008); finally, the distribution of the two proteins in flat (vesicle) and curved (tube) domains was analyzed. These experiments were carried out at the Marie Curie Institute (Paris) in collaboration with Bruno Goud and Jean-Baptiste Manneville.

3. MATERIALS AND METHODS

3.1 Plasmids and antibodies

The FP-22 construct used for live-cell imaging experiments was available in the laboratory and has been described in (Ronchi et al., 2008). It consists of the improved monomeric CFP variant, called mCerulean (A206K mutation) (Rizzo et al., 2004) at the N-terminus linked to the C-terminus of cyt(b_5) by a linker region containing the *myc* epitope and a $[(Gly)_4Ser]_3$ sequence. In this construct the cyt(b_5) sequence is not complete, but only the C-terminal fragment from Pro94 to Asp134 is present, comprising the elongated TMD and the short polar luminal residues. The pCDNA3 construct bearing the temperature sensitive mutant of VSV-G fused to EGFP (ts045VSV-G EGFP) was obtained from Jenninfer Lippincott-Schwartz (NIH, Bethesda, USA), while pRFP-KDEL and pmCherry-GalNAc were kind gifts from Erik Snapp (NIH, Bethesda, USA) and Rainer Pepperkok (EMBL, Heidelberg, Germany), respectively. The pCDNA3 ts045VSV-G AxA construct was generated with a site-directed mutagenesis kit (QuickChange Lightning Site-Directed Mutagenesis kit from Agilent Technologies) using pCDNA3 ts045VSV-G DxE as template. Briefly, the region containing the di-acidic export signal was amplified with two primers that perfectly anneal to the template except for two base pairs designed to replace two A in position 2508 and 2514 with two C in order to substitute the DxE sequence with AxA.

Various other different spectral fluorescent variants of GFP fused to the wild-type or the elongated forms of cyt(b_5) were produced both for expression in cells and for subsequent subcloning into pGEX vector to produce recombinant proteins. pCDNA3 mEGFP-22 was generated starting from the EGFP-22 construct (described in (Bulbarelli et al., 2002): the fluorescent protein was excised with *BamHI* and replaced with the monomeric variant. pCDNA3 mEGFP-17 was available in the laboratory and described in (Snapp et al., 2003). pTagBFP-17 and pTagBFP-22 were generated by ligating the wild-type or the elongated form of cyt(b_5) into pTagBFP-C1 (from Evrogen) opened in the polylinker region with the two restriction enzymes *BspEI* and *EcoRI*. The red spectral version of GFP (tdTomato) was amplified from

ptdTomato-N1 (from Clontech) by PCR using a reverse primer designed with a 3' end that introduced a site recognized by the restriction enzyme *BspEI*. The amplified product was digested with *NheI* and *BspEI* at the 5' and 3' ends respectively, and then ligated into pmCerulean-17 or -22 (Ronchi et al., 2008) after excising the mCerulean sequence with the same two restriction enzymes. Finally, all these constructs were amplified using forward primers designed to introduce an *EcoRI* site upstream to the open reading frame, digested with *EcoRI* at both 5' and 3' ends and ligated into pGEX2T vector (from Amersham) opened in the polylinker region with the same restriction enzyme. All constructs were checked both with diagnostic digestions and sequencing.

Polyclonal α-GFP antibody (from Abcam) and the secondary antibody α-rabbit peroxidase (from Jackson Immunoresearch Laboratories) were used for Western Blot diluted 1:5000 and 1:80000 in blocking buffer (5% milk, 0.1% Tween, 20 mM TrisHCl, 150 mM NaCl) respectively.

3.2 Cell culture, transfection and microinjection

NRK or CV1 cells were cultured in DMEM supplemented with 10% of FBS (Fetal Bovine Serum), 1% of antibiotic mix penicillin/streptomycin (Invitrogen) and 1% of L-glutamine at 37°C and 10% of CO_2.

Both cell lines were transiently transfected either with the Calcium Phosphate method as previously described (Bulbarelli et al., 2002) or with the jetPEI system (from Polyplus transfection) according to the manufacturer's instructions.

Microinjection was performed with an Eppendorf 5200 microinjector by applying a pressure of 80-90 hPa, which injected plasmids (in water solution at a concentration of 100-200 ng/μl) into the nucleus of NRK cells cultured at 80% of confluence. At the times indicated in the figure legends, microinjected cells were either imaged alive, or fixed in 4% paraformaldehyde for 20 min at 37°C.

3.3 Temperature blocks and energy depletion experiments

For temperature block experiments at 20°C, NRK cells were microinjected with FP-22 cDNA, incubated at 37°C at 10% CO_2 for 1 h in order to allow protein expression and then incubated in a refrigerated bath at 20°C for 1 h in DMEM containing 25 mM Hepes (from Sigma-Aldrich) before fixation or live-cell imaging. In the case of either VSV-G DxE or –AxA, cells were transfected for 24 h at the non-permissive temperature of 39,3°C and then, like microinjected cells, incubated in a refrigerated bath at 20°C for 1 h in DMEM plus 25 mM Hepes before starting live-cell imaging.

For energy depletion experiments, cells were incubated in the presence of DMEM without glucose (from Invitrogen) supplemented with 10mM 2-DOG (2-deoxyglucose, from Sigma) and 10 mM NaN_3 for 10 min before live-cell imaging, during which cells were further incubated under energy depletion conditions.

3.4 Imaging of fluorescent live cells, FRAP (Fluorescent Recovery After Photobleaching) experiments and image analysis

For live-cell imaging, co-microinjected or co-transfected cells were shifted to an incubator with both controlled temperature and CO_2 mounted on Zeiss LSM510 Meta confocal microscope in the presence of Imaging Medium (DMEM without phenol red and supplemented with 10% FBS, 1% of L-glutamine and pen/strep, 25 mM Hepes). Single sections of Cerulean-22 were acquired with the 458 nm line of the Argon laser, while 543 nm laser line was used for GalNAc-mCherry or RFP-KDEL imaging. In order to quantitatively study the transport kinetics at the ER-Golgi interface and to avoid any interfering ER signal due to novel protein synthesis during image acquisition, all live-cell imaging experiments were performed in the presence of the protein synthesis inhibitor puromycin at 100 μg/ml (from Sigma-Aldrich).

For VSV-G DxE-EGFP experiments at both 32°C and 20°C, live cells were recorded every 1 min for a total of 50 min.

For FRAP experiments either on Cerulean-22 or VSV-G AxA-EGFP, one pre-bleached image was acquired, and then a region of interest (ROI), corresponding to

the Golgi apparatus or the ER (using as a template the Golgi marker GalNAc-mCherry or the ER marker RFP-KDEL), was drawn and bleached by scanning 30 times with both 405 nm and 458 nm lasers at 100% power. Recovery of the fluorescence signal was recorded at 1 min intervals for 50-60 min.

All images were analyzed with ImageJ software. For the accumulation of VSV-G at the Golgi apparatus, a ROI corresponding to the GalNAc-mCherry-positive area has been drawn and the fluorescence signal of VSV-G in this region was measured over time and normalized to the total fluorescence intensity of the same cell. Similarly, in FRAP experiments the fluorescence recovery of the bleached ROI (corresponding to the Golgi or ER) was measured over time and normalized to the total fluorescence of bleached cells, which was always checked to be constant over time. In all the experiments background signal (determined in an area outside the cells) was subtracted from the fluorescent intensities of the ROIs. Finally, data were averaged and the results shown as graph with GraphPad Prism software.

3.5 Protein expression and purification from bacteria

For reconstitution of fluorescent proteins into liposomes, we used the GST-fusion system (Amersham) to purify mg amounts of our model proteins. BL21 strain of *E. coli*, transformed with pGEX2T constructs already described (see section 3.1), have been grown in a shaker at 37°C until they reach an OD_{600nm} of 0.6 - 0.8 and induced with IPTG 0.5 mM for 4 hours at room temperature. After bacterial lysis with Triton X-100 2%, lysozyme 0.2 mg/ml and DNAse 0.04 mg/ml (in the presence of a protease inhibitor cocktail as described in (Pedrazzini et al., 2000)), the soluble fraction of FP-17 and FP-22 has been attached to glutathione resin GS4B 50% in PBS (from GE Healthcare) for 1 h at 4°C on a rotating wheel. Thanks to the presence of a thrombin cleavage site downstream the GST and upstream FP-17 or FP-22 sequences, resin-bound proteins have been purified by adding thrombin 1 u/μl in PBS in a solution containing PBS and *N*-octyl glucoside 30 mM for 2 h at RT on a rocker. Finally, protein purification has been checked on SDS-PAGE followed by Coomassie Blue staining and quantified with BCA assay (from Perkin Elmer). Since during the purifi-

cation procedure the two proteins were partially degraded, we subtracted this amount to the result obtained with the BCA dosage using ImageJ software.

3.6 Preparation of rat liver microsomes and ER lipid extraction

Rat liver microsomes have been isolated by differential centrifugation. Briefly, a rat liver was homogenized and resuspended in two volumes of sucrose 250 mM, TrisHCl 5 mM pH 7.4, EDTA 0.1 mM and PMSF 0.5 mM. Nuclei and cytoskeletal components have been first removed by centrifugation at 1000xg for 8 minutes at 4°C. Mitochondria, lysosomes and peroxisomes have been pelleted by centrifugation at 10000xg for 10 min and the microsome-containing supernatant further ultracentrifuged at 55000 rpm for 1 h (rotor 55 Ti, Kontron) at 4°C. Finally, pelleted microsomes have been resuspended in sucrose 250 mM, TrisHCl 5 mM pH 7.4 and EDTA 0.1 mM, divided in small aliquots, quickly frozen in liquid nitrogen and stored at -80°C. The protein content has been measured by Lowry method (Lowry et al., 1951) or BCA assay.

500 μl of ER lipids were extracted with organic solvents by adding 9.5 ml of $CHCl_3$/MetOH 2:1 (Folch et al., 1957). Phase separation was achieved by mild centrifugation at 1000xg for 10 min at RT. The aqueous phase was removed and a second extraction has been performed by adding 4.9 ml of KCl 0.1 M/MetOH 1:1. After the second centrifugation, the organic phase has been dried with Rotavapor and the lipid film resuspended in 500 μl of $CHCl_3$ and stored at -20°C. Phospholipids amount was then measured by dosing the phosphate groups and compared samples to a standard of curve built using known amounts of NaH_2PO_4. Briefly, 50 μl of $Mg(NO_3)_2$ were added to samples or standard phosphate solution and were taken to dryness over a flame until the brown fumes disappeared. 0.3 ml of HCl 0.5 M were added to each sample and put in boiling water for 15 min to hydrolyze to phosphate any pyrophosphate formed in the ashing. Finally, a colorimetric reaction has been developed by adding 0.7 ml of a mix composed of 6 parts of ammonium molibdate 0.42% and 1 part of ascorbic acid 10% and incubation for 20 min at 45°C. The samples have been read on a spectrophotometer at 820 nm.

3.7 Detergent dialysis and reconstitution of FP-17 and FP-22 into LUVs (Large Unilamellar Vesicles)

To reconstitute our purified model proteins into LUVs we adopted the detergent dialysis method as previously described (Ceppi et al., 2005). 600 μg of POPC (from Avanti Polar) or ER lipids extracted from rat liver microsomes have been dried with Rotavapor under vacuum for 1 h and then resuspended overnight in KCl 400 mM, TrisHCl 4 mM pH 7.4 and *N*-octyl glucoside 30 mM. In order to pull out nanotubes from GUVs by molecular motors or optical tweezers, we also added a small amounts of biotinylated lipids (see below): 1% (mol/mol) of Cap-Biot-DOPE in the experiments with molecular motors or 0.03% w/w of Biot-DSPE Peg(2000) (from Avanti Polar) in the case of optical tweezers. To obtained proteoliposomes, bacterially purified FP-17 and FP-22 were added to detergent-lipid mix using a molar protein/lipid ratio of 1:500, loaded in dialysis membrane (cutoff 12.000-14.000) and dialyzed for 4 days against 8 x 2 liters of KCl 400 mM and TrisHCl 4 mM pH 7.4.

3.8 Na_2CO_3 extraction and flotation

To check the reconstitution of FP-17 and FP-22 into LUVs, we performed a carbonate extraction of membranes followed by flotation on a discontinuous sucrose gradient. 100 μl of proteoliposomes (or bacterially purified proteins alone) were treated with an equal volume of Na_2CO_3 0.2 M for 30 min on ice and then brought to sucrose 1.2 M in Na_2CO_3 0.1 M in a final volume of 740 μl. The samples were layered under a discontinuous sucrose gradient composed of layers (1, 0.5, 0.25, 0.15 and 0 M sucrose in Na_2CO_3 0.1 M), 560 μl each, which were ultracentrifuged overnight at 40000 rpm at 4°C (Beckman SW 55 rotor). Fractions of 0.7 ml each were collected, precipitated with 2.7 ml of TCA 20%, washed with acetone, resuspended in PBS and analyzed by SDS-PAGE and Western Blot.

3.9 Electron microscopy of negatively stained proteoliposomes

To analyze the morphology of proteoliposomes, formvar carbon-coated nickel grids were place on top of a 30 µl drop of proteoliposomes suspension for 10 min on ice. Grids were then washed quickly 5 times in H_2O, stained for 10 min on ice with uranyl acetate 1% and the excess of uranyl acetate was drained on a Whatman filter. Grids were observed under a Philips CM10 transmission electron microscope.

3.10 Giant Unilamellar Vesicle (GUV) Electroformation

Starting from our reconstituted LUVs, we have chosen the electroformation method to obtain GUVs composed of either POPC only or ER lipids. This method is based on the swelling of dried lipid films rehydrated in a sucrose solution under an alternating electric field (Manneville et al., 2012). Since low salt concentration is necessary to guarantee an optimal growth of the vesicles, we first decreased the concentration of KCl from 400 mM to 100 mM using Midi-Trap G25 desalting columns (GE Healthcare), according to the manufacture's procedure. A second critical parameter to get nice GUVs is the amount of lipids that are deposited on ITO (Indium Tin Oxide) - coated slides used for the electroformation (see below), which should be between 1.3-2.5 µg. At this aim after desalting step, proteoliposomes have been pelleted by ultracentrifugation at 55000 rpm for 2 h at 4°C (Beckman TLS 55 rotor) and resuspended in an appropriate volume of KCl 100 mM and TrisHCl 4 mM pH 7.4 to get a final lipid concentration of 1.3 mg/ml.

The first step of GUV growth consists of depositing small drops (1, 1.5 and 2 µl) of LUV suspension on the conductive side of two ITO-coated slides (Präzisions Glas & Optik GmbH), which will be used to build the electroformation chamber. In order to explode reconstituted LUVs and let them to pile up on ITO-coated slides, the samples were dried overnight under vacuum. The electroformation chamber was built with two ITO cover slides with their conductive sides facing each other, separated by a 1 mm Teflon spacer, connected to a low frequency generator (TG315 function generator, TTi Thurlby Thandar Instruments) via adhesive copper electrodes and sealed

with Sigilum wax (Vitrex Medical A/S) (Fig. 18). Dried proteoliposomes were then rehydrated by filling the chamber with a sucrose solution, whose osmotic pressure has to match to that of the experimental buffers that will be used.

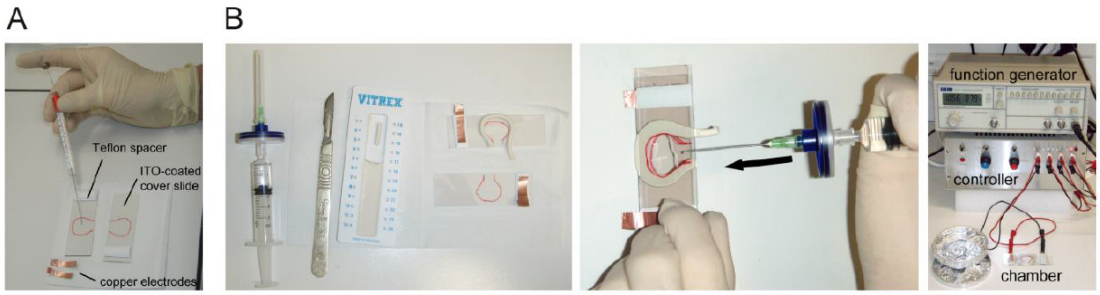

Figure 18: GUV electroformation. In A is depicted the spreading of samples on ITO-coated slides, while B shows the assembling of the electroformation chamber, the rehydratation of sample with sucrose and the application of an alternate electric field (Manneville et al., 2012).

Since GUVs are very sensitive to osmotic shock, matching the osmotic pressures represents another fundamental step in the electroformation protocol. In particular, to slightly deflate membranes and facilitate tube pulling we always used a sucrose with an osmotic pressure about 20-30 mOsm lower that that of the experimental buffers. In our case, we used two different osmolarity of sucrose, 180 mOsm and 279 mOsm, depending on the experiments we next performed, tube pulling with molecular motors or optical tweezers, respectively. Finally, an alternate electric field with an increasing voltage ramp from 20 mV to 1.1 V (6 minutes each step) at 10 Hz frequency has been applied for 3-4 hours. GUV growth has been checked in phase contrast (Axiovert 200M, Carl Zeiss) and then 20 µl of vesicles have been taken from the center of the drops, transferred into a 0.5 ml eppendorf and stored at 4°C.

3.11 In vitro microtubule polymerization and elongation of nanotubes with molecular motors

This method is an *in vitro* assay based on the ability of kinesins to pull out lipid nanotubes from GUVs in the presence of polymerized microtubules and ATP. In this assay kinesins can bind membranes thanks to the presence of both biotinylated kine-

sins and lipids and streptavidin that bridges the two biotinylated components (Roux et al., 2002).

A 50 µl aliquot of tubulin (purified from animal brain as described in (Hyman, 1991) dissolved in a solution containing GTP 1 mM and BRB (PIPES 80 mM, $MgCl_2$ 1 mM and EGTA 1 mM) has been thawed and incubated 15 min at 37°C to allow polymerization of microtubules (MTs). To obtain fluorescent MTs, 0.5 µl of Rhodamine tubulin 10 mg/ml can be added to purified tubulin. Microtubule network has been then stabilized with 2 µl of Taxol 1 mM and incubated again for 15 min at 37°C. Non-polymerized MTs were removed by centrifugation at 70000 rpm for 17 min at 37°C (Beckman TLA 100 rotor) and the pellet of polymerized MTs was finally resuspended in 50 µl of BRB plus Taxol 30 µM.

The tube assay has been performed in a flow chamber built using two parafilm spacers sandwiched between a glass slide and a coverslip and quickly melt on a hot plate (Fig. 19).

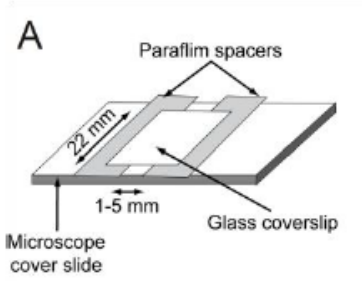

Figure 19: schematic representation of the flow chamber used in the kinesin assay (Manneville et al., 2012).

5 µl of MTs was loaded into the flow chamber and incubated 15 min at RT in order to allow the adhesion of MTs to the coverslip. The chamber was rinsed twice with IMI buffer (Imidazole 50 mM pH 6.7, NaCl 50 mM, EGTA 2 mM and $MgCl_2$ 1 mM) plus Casein 5 mg/ml and Taxol 30 µM and then filled with 5 µl of biotinylated kinesins pre-incubated on ice with 5 µl of streptavidin 1 mg/ml. After a 15 min incubation at RT, 10 µl of Motility buffer (IMI buffer supplemented with Taxol 30 µM, ATP 1 mM, DTT 5 mM, glucose 25 mM, catalase 0.18 mg/ml and glucose oxidase 0.37 mg/ml) were added and finally 1 µl of GUVs was loaded into the chamber and incubated for 15 min at RT to let kinesins to pull nanotubes. To avoid chamber dry-

ing, the flow chamber was sealed with Sigilum wax on both sides and left horizontally before the observation.

Single optical sections have been taken for both FP-17 and FP-22 channels in the vesicle plane and in the tube plane using Nikon AR1 confocal microscope. Images of TagBFP-17 and -22 have been acquired with 405 nm laser, while for both Venus and mEGFP spectral variants the Argon laser 488 nm have been used. TdTomato-17 and -22 have been acquired with 561 nm laser. All images have been captured by adjusting acquisition settings in order to avoid pixel saturation.

Concerning FRAP experiments, we acquired 3 pre-bleached images and then a portion of the vesicle or of the tube (selected by drawing 3 x 4 μm or 3 x 9 μm, respectively) were bleached. The fluorescence intensity recovery has been followed over time by taking one image every 6 seconds for a total of 5 min for vesicles and 9 min for tubes. The analysis has been done as described in section 3.5 of this chapter. Half-times and mobile fractions were derived from experimentally measured data by fitting the following monoexponential equation:

$$F(t) = F_{post} + (F_{rec} - F_{post})(1 - e^{-t/\tau})$$

where F_{post} is the fluorescence signal after photobleaching, F_{rec} is the maximum fluorescence recovery value that is reached after bleaching, t the final time of registration and τ the mid time of registration.

3.12 Optical tweezers and micropipette aspiration to pull lipid nanotubes of controlled radius

The second method we used to create artificial curved domains is based on a combination of two approaches, the optical tweezers and micropipette aspiration; the tube is held between the GUV aspirated by a micropipette and a streptavidin-coated bead trapped by optical tweezers. By progressively increase the aspiration force, it's possible to progressively increase the membrane tension and, consequently, the tube radius that can range between 200-10 nm (Callan-Jones et al., 2011).

The micropipette aspiration system is based on a suction pressure that is applied between the inside and the outside of the pipette by lowering a water reservoir com-

pared to a reference level (typically the aspiration can vary from 0 to 200 Pa, which corresponds to a vertical displacement of the water reservoir from 0 to 2 cm). When the water level is higher than the micropipette level, GUVs will be blown by the micropipette, while when the water level is lower the micropipette will aspirate. Pipettes are prepared using borosilicate glass capillaries (internal radius 0.7 mm, external radius 1 mm, from Kimble Glass Inc.), which are pulled using a pipette puller (Sutter instrument P-2000) and the pipette radius is set to the appropriate size (about 4 μm) using a microforge microscope (MF-800 Narishige, Japan). On the other hand, optical tweezers are created by a focused infra-red laser beam (Ytterbium fiber laser 1070 nm, 5W, IPG GmBH).

To perform the experiments, a micromanipulation chamber of about 200 μl was built using two coverslip spaced by a glass slide (Fig. 20), incubated for 10 min with casein 10 mg/ml to prevent membrane adhesion to glass surface and rinsed twice with HKM buffer (50 mM Hepes pH 7.2, 120 mM KAcetate, 1 mM $MgCl_2$ and 2 mM EGTA) and filled again with 200 μl of HKM. Then the micropipette (filled with Casein 10 mg/ml to prevent again membrane adhesion on glass surface) was inserted into the chamber and 2-3 μl of streptavidin-coated polystyrene beads (1.5 μm in diameter, from Spherotech Inc.) were injected into the chamber and followed by the injection of 5-10 μl of GUVs. After selecting an optically fluctuating vesicle, the zero reference pressure has been set by adjusting the level of water reservoir (neither aspiration nor blowing of the selected vesicle) and the vesicle has been aspirated by slightly increasing the suction pressure. After trapping a bead into the optical tweezers, a tube was pulled by contacting biotinylated lipid-containing GUV with the bead and moving the GUV away from the trap and finally the aspiration force has been progressively increased step by step, where one step typically corresponds to a vertical movement of the water reservoir of 0.5 mm. For each tension step, one equatorial confocal plane, in which both the vesicle and tube were on focus, has been acquired as well as a DIC movie has been created to record the position of the bead relative to the trap center.

As in the case of kinesin assay, Nikon AR1 confocal microscope has been used to take single optical section and 488 nm or 561 nm lasers were used to image mEGFP-17 and -22 or tdTomato-17 and -22, respectively. The fluorescence images were used to analyze the distribution of FP-17 and FP-22 in vesicles and tubes during the different tension steps, while DIC movies are needed to measure bead displace-

ment, which is required to derive the force applied in each step and the progressive increase of the tube radius.

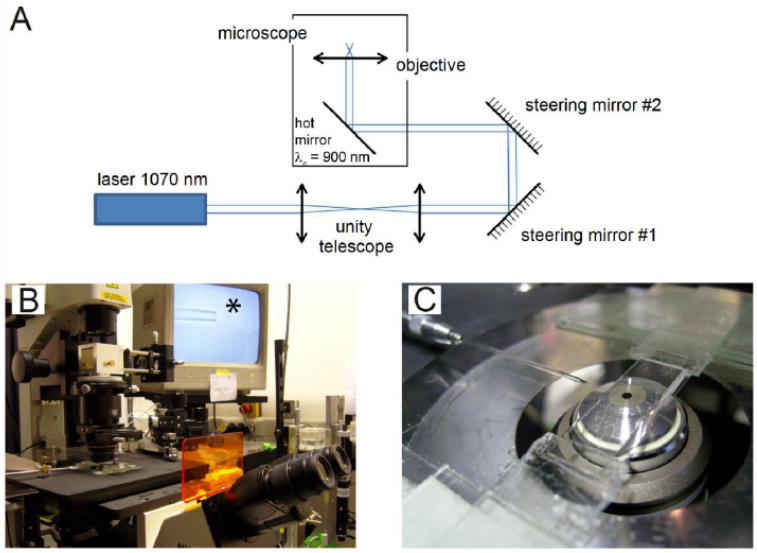

Figure 20: in A a schematic representation of the optical path of laser tweezers is shown; B shows a general view of the set-up we used and C displays the micropipette inside the micromanipulation chamber (Manneville et al., 2012).

3.13 Analysis of sorting ratio between FP-17 and FP-22 in GUVs and nanotubes

To analyze the distribution of FP-17 and FP-22 in tubes pulled out with molecular motors, we developed a manual method on ImageJ that allows us to globally quantify the mean fluorescence intensity of the two proteins in the entire tube network. First, the background maximum intensity was measured and subtracted to the image in order to set all the background pixels at 0 (Fig. 35 B). Then a ROI around the tube network or the vesicle has been drawn and the rest of the image has been cleared to exclude fluorescent objects not belonging to the tube network or vesicle (such as other vesicles or dirts) and a manual threshold was applied to create a mask and a binary image highlighting only the tube network or the vesicle (Fig. 35 B). This mask has been then superimposed to the original image (with the image calculator tool and the operator AND) and the mean fluorescence intensity has been measured (Fig. 35 B). Data from all experiments were averaged, the ratio of FP-22 over FP-17

was calculated in vesicles and in tubes and compared by paired t test with GraphPad Prism software.

For the optical tweezers and micropipette aspiration technique, the fluorescent signal of FP-17 and FP-22 in each vesicle and tube has been measured using a Matlab routine (from Bassereau lab, Institute Curie, Paris) (Sorre et al., 2009). Briefly, a rectangular selection was drawn around the horizontal tube and pixel intensity were averaged along the horizontal lines of the selection, giving an averaged fluorescence profile along the vertical axis. The same operation was also applied to the vesicle by selecting part of it. Then the sorting ratio was used to quantify protein sorting; the sorting ratio is defined as the ratio of FP-22 over FP-17 in the tube normalized by the same ratio in the vesicle:

$$Sorting\ ratio = \frac{I_{22\ tube}/I_{17\ tube}}{I_{22\ ves}/I_{17\ ves}}$$

The initial membrane tension required to pull a tube and its progressive increase applied to increase the membrane curvature and decrease tube radius were deduced by Laplace's law (Kwok and Evans, 1981) and is given by the following equation:

$$\sigma = \frac{(R_{pip} * \Delta P)}{2(1 - \frac{R_{pip}}{R_{ves}})}$$

where R_{pip} is the radius of the pipette, R_{ves} is the radius of the vesicle and ΔP is the vertical displacement of the water reservoir linked to the micropipette.

All the collected sorting ratios were then averaged and plotted versus membrane tension with GraphPad Prism software.

4. RESULTS

4.1 Anterograde transport of VSV-G DxE at the ER-Golgi interface at 32°C

In previous work we showed that FP-22, our model protein lacking an export signal in its cytosolic portion, is transported along the secretory pathway and reaches the plasma membrane more slowly compared to the export signal-bearing cargo VSV-G (Ronchi et al., 2008). And we also demonstrated that the DxE export signal permits a stronger recruitment at the ERES compared to FP-22. To investigate whether the di-acidic export signal has another role downstream protein recruitment at ERES, we analyzed and compared the transport rate of VSV-G and FP-22 in the different steps of the secretory pathway. First, we started to study the ER to Golgi anterograde transport of VSV-G. As described in chapter 3, we took advantage of the temperature-sensitive mutant form of VSV-G: when cells are incubated at 39°C VSV-G is not properly folded and, in this way, is retained in the ER, while at the permissive temperature of 32°C it becomes folded, exits from the ER and is transported to the plasma membrane. NRK cells were transfected for 24 h at 39°C with VSV-G GFP and then we analyzed its accumulation to the Golgi apparatus by live-cell imaging at the permissive temperature of 32°C. As soon as we shifted cells to 32°C, VSV-G was distributed mostly in the ER (Fig. 21 A, upper left picture), even though in some cells a small accumulation to the Golgi has been observed (upper right cell). This probably happens during the few minutes that cells spent on the microscope (whose incubator was set at 32°C) and that are required to have them on focus and to set correct acquisition settings before starting image registration. VSV-G showed a clear Golgi enrichment already after 5 min (Fig. 21 A, upper central picture) and in 12 min it was mostly localized in the Golgi and it is no longer distributed into the ER (Fig. 21 A, upper right picture). Since at 32°C the transport proceeds to the plasma membrane, at later timepoints VSV-G was progressively accumulated in the plasma membrane as well as the Golgi apparatus displayed a progressive emptying (Fig. 21 A, lower left and central pictures) and after 40 min it is mostly localized at the plasma membrane (Fig. 21

A, lower right picture). By measuring VSV-G fluorescence signal in the Golgi apparatus over time, it clearly appears that its anterograde transport rate at the ER to Golgi interface is very fast; indeed, the fluorescent intensity rapidly increases and the signal reaches a peak after only 12 minutes (Fig. 21 B). Since the fluorescent signal likewise rapidly decreases after 12 min, it also emerges that once reaches the Golgi, VSV-G efficiently leaves the Golgi and it is transported to its final destination (Fig. 21 B).

4.2 Anterograde transport rate of FP-22 from the ER to the Golgi at 37°C

We then moved to study the transport of FP-22 from the ER to the Golgi. To visualize the protein when is still in the ER, we co-microinjected nuclei of NRK with cDNAs encoding FP-22 and GalNAc-mCherry to generate a synchronized wave of expression and cells were imaged at 37°C in the presence of puromycin 1 h after microinjection, which represents the minimum time to have enough protein expression and to detect a fluorescent signal. As shown in figure 22 A (upper panels), 1 h after microinjection FP-22 is distributed not only in the ER, but is also partially accumulated in the Golgi and, indeed, co-localizes with the Golgi marker GalNAc-mCherry. Because of its double distribution, to study the transport from the ER to the Golgi we photobleached FP-22's Golgi fractions (Fig. 22 A, arrowheads and red ROIs in inset) and we followed fluorescence recovery over time. Surprisingly, we found a clear recovery of the Golgi signal already 5 min after bleaching and fluorescence progressively increased over time and reached a peak 20 min postbleach. This behavior can be particularly appreciated in merged images (Fig. 22 A, central pictures), where the Golgi apparatus (labeled with GalNAc-mCherry) progressively becomes "yellow" due to the increasing fluorescence in FP-22 channel. As in the case of VSV-G, since at 37°C protein transport can proceed to the plasma membrane, after reaching maximum recovery at 20 min postbleach, FP-22 Golgi signal slowly decreases and the protein reaches the plasma membrane (Fig. 22 A, lower panels). The fast ER to Golgi anterograde transport of FP-22 was further confirmed by quantitative analysis as shown in Fig. 22 B; after bleaching, FP-22 Golgi fluorescence increases very rapidly and

more than 90% of the signal recovers within 15-20 min, indicating that FP-22 transport rate is comparable to that of VSV-G.

4.3 Localization of FP-22 and VSV-G DxE upon incubation at 20°C

Since at the physiological temperature of 37°C the transport can proceed along the secretory pathway to the plasma membrane and, therefore, while our model proteins are reaching the Golgi apparatus there is also a trafficking flux towards the plasma membrane, to better investigate the transport at the ER-Golgi interface we took advantage of the temperature block at 20°C. Indeed, at this temperature the membrane fluidity from the *trans*-Golgi cisternae to the plasma membrane is blocked and only the transport between ER and Golgi is allowed (Kusimanen and Saraste, 1989). NRK cells were co-microinjected with FP-22 and GalNAc-mCherry, incubated for 1 h at 37°C to allow protein expression, shifted to 20°C for 2 h and then fixed. As shown in figure 23 (upper panels), FP-22 is not completely accumulated in the Golgi apparatus (co-localization with GalNAc-mCherry), but it displays also an ER distribution. By contrast, after transfection at the non permissive temperature of 39°C followed by a 2 h incubation at 20°C, VSV-G EGFP expressing cells display complete accumulation of the protein in the Golgi, as demonstrated by the perfect co-localization with GalNAc-mCherry and the absence of ER distribution (Fig. 23, lower panels).

4.4 ER to Golgi transport of VSV-G is slowed down at 20°C

To establish the transport rate of VSV-G DxE from the ER to the Golgi, we co-transfected NRK cells with VSV-G EGFP and GalNAc-mCherry at 39°C for 24 h and we performed live-cell imaging at 20°C. Since at 20°C only the transport between the

ER and the Golgi is permitted, we were able to measure both the accumulation of VSV-G to the Golgi and the ER emptying. As shown in figure 24 A (upper panels), as soon as cells are shifted from 39°C to 20°C, VSV-G is predominantly localized only in the ER, but then it starts to progressively accumulate in the Golgi, as demonstrated by the increase in the fluorescent intensity of the perinuclear region, which co-localizes with GalNAc-mCherry (Fig. 24 A, central panels). Since cells were imaged in the presence of 100 μg/ml puromycin, simultaneously to Golgi accumulation, we also observed a progressive and constant decrease of the VSV-G ER signal over time, which is particular evident in the two cells highlighted in insets (Fig. 24 A, left panels). Quantitative analysis confirmed that at 20°C VSV-G is progressively transported from the ER to the Golgi and that its Golgi fluorescence intensity doubles during the registration, while the ER signal decreases of about 50-60% (Fig. 24 B). Since in the latest timepoint the Golgi fluorescence was still increasing as well as the ER signal still decreasing, these data also indicates that VSV-G transport is significantly slowed down at 20°C compared to 32°C, where in 12 min it was completely accumulated in the Golgi (Fig. 21).

4.5 ER to Golgi transport and intrareticular diffusion of FP-22 at 20°C

Since we have found that FP-22 didn't completely accumulate in the Golgi apparatus upon incubation at 20°C (Fig. 23 and section 4.3), raising the possibility that FP-22 anterograde transport is somehow impaired at this temperature, we analyzed its ER to Golgi transport by live-cell imaging. Like in the experiments performed at 37°C (Fig. 22 and section 4.2), cells were co-microinjected with FP-22 and GalNAc-mCherry and incubated for 1 h at 37°C to allow protein synthesis. Cells were then shifted to 20°C for 30 min before starting FRAP experiments at the same temperature. Since the ER is spread everywhere in the cytosol and even in the Golgi region and, therefore, could potentially disturb our transport analysis, we also bleached a portion of the ER in some FP-22 expressing cells (as indicated by the arrow and in Fig. 25 A) and we compared ER fluorescence recovery to that of the Golgi (bleached regions are

indicated by the arrowheads, Fig. 25 A). After Golgi bleaching, a clear fluorescence recovery was observed and, indeed it progressively became more intense over time (left panels and in the lower cell of inset, Fig. 25 A). This recovery can be also appreciated in merged images, where the Golgi apparatus of the bleached cells progressively becomes "more yellow" due to the increase of FP-22 signal (central panels, Fig. 25 A). Thus, FP-22 transport is not blocked at 20°C and, as in the case of VSV-G, is slowed down compared to 37°C (Fig. 22); indeed, the analysis showed that the Golgi signal was still increasing after 60 min (Fig. 25 B). In contrast, FRAP on an ER portion (indicated by the arrow and by the red ROI in the upper cell of insets, Fig. 25 A) displayed a complete recovery 20 min after bleaching and the signal no longer increased at later timepoints (40 and 60 min, Fig. 25 A). Quantitative analysis indicated that the diffusion of FP-22 within the ER is fast and that the equilibrium is reached within 10-15 min after bleaching and that, since Golgi apparatus behaves differently, we are able to discriminate between intrareticular diffusion and transport at the ER to Golgi interface.

Since vesicular transport is an energy-dependent process, to further control whether the fluorescence recovery we observed in the Golgi apparatus was really due to FP-22 transport from the ER to the Golgi, we repeated Golgi FRAP experiments on energy-depleted cells. After microinjection, incubation for 1h at 37°C followed by 20 min at 20°C, cells were kept other 10 min at 20°C in energy-depleted condition and then FRAP experiments were performed maintaining the same temperature and the absence of energy. After bleaching FP-22's Golgi fraction (yellow ROIs, Fig. 26 A), a fast fluorescence recovery was observed, but after 15-20 min, when the bleached region has reached the same intensity of the surrounding ER, Golgi fluorescence no longer increased and the signal was constant until the end of the registration (Fig. 26 A), mimicking exactly the same behavior of ER diffusion (Fig. 25). Indeed, as shown in Fig. 26 B, Golgi fluorescence recoveries are similar between +/- ATP at early timepoints where the major contribution is given by ER diffusion, but then, in the absence of energy, the fluorescence signal reaches a plateau and no longer increases because of the inhibition of transport, while in the presence of energy the signal continues to increase at later timepoints until the end of the registration. To better appreciate the difference between the two conditions, we also measured the fluorescent intensity profile, before and 60 min after bleaching, along a line that comprised a portion of the ER and of the Golgi (white lines in Fig. 27). Both in the presence or absence of ener-

gy, prebleach images displayed an intense Golgi fluorescence that is clearly distinguishable from the lower ER signal (Fig. 27). In the presence of ATP, 60 min after bleaching, fluorescent intensity profile showed a nice recovery in the Golgi, whose fluorescence is still distinguishable from the surrounding ER and resembled the same three peaks of prebleach Golgi profile (upper graph, Fig. 27). In contrast, in energy-depleted conditions, 60 min postbleach the fluorescence intensity in the Golgi region no longer mimicked prebleach profile and had exactly the same intensity of the surrounding ER (lower graph, Fig. 27).

Taken together, all these data demonstrated that our experimental system and the photobleaching approach represent a useful tool to study FP-22 transport at the ER-Golgi interface.

4.6 FP-22 is recycled from the Golgi to the ER

In previous experiments we demonstrated that FP-22, on one side, does not completely accumulate in the Golgi apparatus upon incubation at 20°C for 2h (Fig. 23), but also, on the other side, that its anterograde transport from the ER to the Golgi is not blocked at this temperature (Fig. 25), raising the possibility that FP-22 is recycled from the Golgi to the ER. To test this hypothesis, we bleached the ER fraction of FP-22 and we measured either fluorescence recovery of the ER or the Golgi intensity over time. In figure 28 two co-microinjected cells with FP-22 and RFP-KDEL are shown (upper panels). Like in previous experiments, microinjected cells were incubated 1 h at 37°C, followed by 30 min at 20°C and then imaged at the same temperature. Cells were imaged for 30 min before bleaching and, then, by drawing ROIs using RFP-KDEL as ER template, ER fractions were bleached and fluorescence recovery was followed for 60 min. As shown in insets (right panels, Fig. 28 A) and in the quantification (left graph, Fig. 28 B), before bleaching FP-22 Golgi fluorescence (black squares) is stable, but then progressively decreases over time until the end of the experiments and this event is also accompanied by a recovery of the ER fluorescence (black circles). By comparing FP-22 Golgi intensity between Golgi and ER bleaching experiments, it can be appreciated that the two curves display specular

trends; indeed, the recovery observed after Golgi bleaching (black circles) has a similar slope to that of the decrease after ER bleaching (black squares, right graph, Fig. 28 B). These results demonstrated that FP-22, once arrives to the Golgi, is retrogradely transported back to the ER; moreover, Golgi fluorescence is stable before bleaching, indicating that at 20°C it reaches an equilibrium and, therefore, anterograde and retrograde transports occur with comparable kinetics.

To investigate whether FP-22's recycling from the Golgi to the ER is a general phenomenon that happens even at physiological temperatures and not only at 20°C, we repeated the same experiments at 37°C, at which the fluidity of cellular membranes is not altered. As shown in figure 29 A and B, also at this temperature after bleaching the ER fraction of FP-22 there was a progressive decrease of Golgi fluorescence over time. In some cells we also observed FP-22-positive tubular structures leaving Golgi apparatus towards the ER (arrowhead in the inset of 5 min postbleach, Fig, 29 A). Of course, since at 37°C vesicular transport along the secretory pathway is not impaired in any step, theoretically the transport from *trans*-Golgi to PM might partially contribute to the decrease of Golgi fluorescence. But if this was the case, in unbleached cells (lower left cell, Fig. 29 A) we would have observed the same progressively loss of fluorescence of the Golgi apparatus and a progressive appearance of the PM; instead, in our experiments FP-22 fluorescence in Golgi was stable over time as well as FP-22 signal in the plasma membrane did not dramatically increase, indicating that the observed Golgi emptying was mainly due to retrograde trafficking of FP-22 back to the ER.

4.7 VSV-G AxA behaves similarly to FP-22

In figure 23, we showed that VSV-G DxE, in contrast to FP-22, completely accumulated into the Golgi apparatus upon incubation at 20°C, suggesting that is not included into retrograde transport from the Golgi to the ER; or even if it is recycled, the balance between anterograde and retrograde transports strongly favors the anterograde direction allowing a complete recruitment to the Golgi and the absence of ER distribution. To investigate whether VSV-G is excluded from recycling at the ER-Golgi in-

terface because of the presence of the export signal in its cytosolic tail, we mutagenized the di-acidic sequence and we replaced it with two alanines (AxA) (Fig. 30 A). Even though the export signal interacts with Sec24 subunit of COPII and plays a crucial role for VSV-G recruitment at ERES (Nishimura and Balch, 1997), the signal-deficient form of VSV-G is still able to travel along the secretory pathway and to reach the plasma membrane: indeed, NRK cells transfected with VSV-G AxA for 24 h at the permissive temperature of 32°C, displayed a complete PM distribution (Fig. 30 B), as was already demonstrated by other groups in other cell lines (Dukhovny et al., 2009). To study transport of VSV-G AxA at the ER-Golgi interface, cells were transfected for 24 h at the non permissive temperature of 39°C, in order to accumulate the protein in the ER, incubated for 30 min at 20°C to block transport from TGN to PM, and imaged alive at the same temperature in the presence of a protein synthesis inhibitor. First, we observed that upon incubation at 20°C VSV-G AxA showed a similar distribution to that of FP-22 between the ER and the Golgi apparatus (left panels, Fig. 31 A). Therefore, to investigate the possibility of recycling, we applied the same photobleaching strategy: the ER fraction of VSV-G AxA (red ROI in prebleach and bleach images, Fig. 31 A) was photobleached and both fluorescent recovery of the ER and fluorescent signal of the Golgi were measured over time. After ER bleaching, a clear progressive decrease of Golgi fluorescent was observed in all timepoints and at the end of the experiment the Golgi signal of VSV-G AxA was very weak compared to prebleach and bleach images (Fig. 31 A). This behavior appeared clearly also in merged images, where the Golgi apparatus was “yellow” at the beginning, meaning that VSV-G and GalNAc fluorescence intensities were comparable, and then progressively became more “red” because of the fluorescence decrease in VSV-G channel (lower panels, Fig. 31 A). As shown in figure 31 B, quantitative analysis revealed that the decrease of Golgi fluorescence (black squares) after bleaching is also accompanied by a specular recovery of the ER fluorescence (black circles) as demonstrated by the similarity of the slope of the two curves. Even though fluorescence is very low, the recovery of the ER signal can be even perceived in images shown in Fig. 31 A (upper panels). All these data demonstrated that the signal-deficient form of VSV-G behaves as FP-22 and it is continuously recycled from the Golgi to the ER.

These experiments also indicates that anterograde and retrograde transport rates of VSV-G AxA at the ER-Golgi interface are comparable; indeed, by measuring Gol-

gi fluorescence for 30 min before bleaching, we observed that the signal is stable, meaning that at 20°C there is a balance between the transport from the ER to the Golgi and that of in the opposite direction (Fig. 31 B). This observation is further confirmed by the fact that in unbleached cells Golgi fluorescence didn't change during the 80 min of recording (upper cell, Fig. 31 A).

4.8 Reconstitution of FP-17 and FP-22 in LUVs

To investigate whether FP-22 is segregated into curved domains because here it could tilt less its TMD to accommodate the hydrophobic mismatch (see section 1.7.2), we pulled out lipid nanotubes from GUVs reconstituted with both FP-17 and FP-22. To this aim, we generated different fluorescent variants of our model proteins and we purified mg amounts of them. After having generated the different variants in plasmids designed for expression in mammal cells (see section 3.1), we transfected CV1 cells with all these constructs to analyze their steady-state distribution on fixed cells at confocal microscope and we compared them to the localization of Venus-17 and -22 variants, which were already available in our laboratory (described in (Ronchi et al., 2008). As shown in Fig. 32 A, all the different FP-17 spectral variants displayed a clear ER distribution and, depending on the focus plane that was acquired, the nuclear envelope was also observed in some images (Venus-17 and mEGFP-17 pictures, Fig. 32 A). By contrast, all fluorescent versions of FP-22 were uniquely distributed at the plasma membrane and the typical ER distribution of the shorter TMD was not observed (lower panels, Fig. 32 A).

After subcloning all these sequences in pGEX2T vector, we expressed in and purified them from bacteria and then checked on SDS-PAGE followed by Coomassie Blue staining. All recombinant proteins had the predicted molecular weight (upper and predominant band in each lane, Fig. 32 B). As expected, Tomato-17 and -22 are bigger than other proteins because the fluorescent protein tdTomato is composed of two red fluorescent proteins linked together to from a tandem dimer (Nienhaus and Wiedenmann, 2009), while all the other proteins are monomeric. Due to the presence of five more aminoacids in FP-22 proteins, a shift in the molecular weight between

FP-17 and FP-22 was detected in all fluorescent variants, even though was less evident in TagBFP and Tomato variants. On SDS-PAGE we also observed that a number of minor bands of smaller molecular weight, that probably correspond to degradation products formed during the purification process, were always present, and that the amount of degradation was bigger in purified FP-17 compared to the corresponding FP-22 as well as it varied depending on the fluorescent version that was used (Fig. 32 B).

As shown in Fig. 33 A, the shape and morphology of FP-17 and/or FP-22-containing proteoliposomes were analyzed by negative staining at the electron microscope. In all conditions (liposomes without proteins, with FP-17 or -22 and with both of them), proteoliposomes are round-shaped and they are homogenous within the field. The averaged diameter was also measured, but no clear differences between experimental groups were observed as well as a big heterogeneity between different preparations was found (not shown).

The insertion of the two proteins within the bilayer was analyzed by membrane carbonate extraction followed by discontinuous sucrose gradient and Western blot analysis (Fig. 33 B). In proteoliposomes both FP-17 and FP-22 were found in the top, light fractions of the gradient, meaning that the two proteins interact with lipids, which confer to proteins the ability to float in the gradient (left panel, Fig. 33 B). In contrast, the two proteins alone were found only on the bottom fractions of the gradient (right panel, Fig. 33 B), indicating that FP-17 and FP-22 are tightly integrated in the lipid bilayer. Interestingly, the amount of proteins that was degraded during the purification process (see above) is not inserted in the lipid bilayer and, indeed, didn't float and remained in the heavy fractions of the gradient, indicating that only full-length proteins are reconstituted in liposomes (left panel, Fig. 33 B).

4.9 FP-17 and FP-22 are not segregated in lipid nanotubes pulled out with molecular motors

To investigate the role of membrane curvature in TMD-dependent partitioning of FP-22 in ER tubules and ERES, in collaboration with Jean-Baptiste Manneville and

Bruno Goud at Marie Curie Institute (Paris, France), we generated FP-22 and FP-17 reconstituted Giant Unilamellar Vesicles using the electroformation technique (reviewed in (Manneville et al., 2012)) starting from our reconstituted LUVs. After some efforts, we set up a good protocol to achieve an abundant growth of GUVs by applying an alternate electric field for 4 h and figure 34 shows a typical growth of our reconstituted giant vesicles. Since this method is based on the swelling, under an alternate electric field, of lipids that are previously piled up on a conductive slide under vacuum, GUVs display a typical layering with the smallest vesicles close to the glass surface of the slide (low focus, Fig. 34) and with bigger vesicles that are found by progressively moving the focus away from the focus plane of the glass surface (medium, high and max focus, Fig. 34). The main advantages of GUVs are their micrometer scale size and that some micromanipulation techniques are available to pull out very thin nanotubes (Sens et al., 2008). In figure 35 A, the principles of the first technique we used to create artificial highly curved domains are depicted. This assay is based on *in vitro* polymerized MTs that are attached to a coverslip, and on biotinylated kinesins that, in the presence of ATP, walk along MTs and pull nanotubes (averaged tube radius of about 20 nm) from GUVs that can be bound thanks to the presence of streptavidin and biotinylated lipids. A representative picture of *in vitro* polymerized, fluorescent MT networks is shown in Fig. 35 B.

In order to compare the distribution of FP-17 and FP-22 in curved (tubules) and flat (vesicle) domains, for each GUV, two single optical sections were acquired in the equatorial plane of the vesicle and in the plane of the tube network. Indeed, kinesins walk along MTs that are attached to the coverslip and, thus, they pull nanotubes from the bottom of the vesicle, whose focus plane does not correspond to the equatorial plane of the vesicles (Fig. 36 A). As shown in the tube plane of figure 36 A, the distribution of the two proteins was not homogenous in all tubes of the network; some tubes appeared predominantly “red”, meaning that FP-22 is enriched compared to FP-17 (left side of the network, tube plane images, Fig. 36 A), but in some other it seemed the opposite (right and upper side of the network, Fig. 36 A). For this reason and to globally analyze protein distribution within tube networks, we developed a manual quantification method as described in section 3.13 and shown in Fig. 36 B. The first two fluorescent couples we used in these experiments were TagBFP-17 together with Venus-22 and Venus-17 with TagBFP-22. Unfortunately, image analysis revealed that TagBFP fluorescent protein itself was not homogenously distributed in

flat and curved domains, but it showed a preference for tubules and, therefore, it was altering the analysis (not shown). In contrast, the green (mEGFP)-red (tdTomato) couples were found homogenously distributed in vesicles and tubules and, therefore, we always used these couples in all tube pulling experiments that will be shown. The kinesins assay was performed on either GUVs of uniform lipid composition (POPC) or composed of ER lipids extracted from rat liver microsomes. In all cases any statistically significant difference in the fluorescence intensity ratio of FP-22 over FP-17 in vesicles and tube was found and, indeed, in all the three histograms (Fig. 37 A and B), the mean fluorescence ratio in tubes has about the same value of the mean ratio in vesicles. Since in the case of ER lipids (Fig. 37 B) we analyzed both mEGFP-17 versus Tomato-22 and the inverted couple and no differences were found between them, we also demonstrated that fluorescent proteins themselves were not influencing our results. Since a lot of heterogeneity between different tube networks was found, we decided to analyze the sorting ratio (fluorescence intensity ratio of FP-22 over FP-17 divided by the same ratio in the vesicle, see section 3.13) distribution of all tube networks; even though most networks showed a sorting ratio around 1, one or two outliers in which FP-22 was enriched in tubes compared to FP-17 were always found in each experimental group (red squares, left graphs, Fig. 37 A and B). And this became even clearer when all the experimental data were grouped and analyzed together (Fig. 37 C); also in this case the mean fluorescent ratio of FP-22 over FP-17 in tubes was identical to the value in the vesicles and, indeed, *t test* didn't reveal any statistically significant difference. But the analysis of the sorting ratio distribution displayed the presence of some outliers reporting always an enrichment of FP-22 in tubes and never reporting the opposite situation (FP-17 partitioning in tubes). Indeed, the skewness (g_1) calculation revealed that the distribution of our dataset is far from being symmetrical and that the asymmetry was due to high values. Taken together, these data suggests that FP-22 was not significantly enriched in tubes pulled out with molecular motors compared to FP-17, but probably under specific conditions, which have been reproduced in the outliers, FP-22 may be preferentially partitioned into highly curved domains.

4.10 FP-17 and FP-22 diffuse similarly in flat and curved domains

Because of the outliers found in the previous experiment (Fig. 37) suggesting the possibility that FP-22 could be partitioned into curved domains under specific conditions, we further investigate this hypothesis by combining FRAP and real time registration to the kinesin assay. Theoretically, if FP-22 prefers curved domains, it would diffuse faster than FP-17 in tubes. Moreover, since tdTomato is about twice bigger than mEGFP, with FRAP we also tested whether it could influence the diffusion of our model proteins within the thin nanotubes because of steric reasons. Therefore, we photobleached in both FP-17 and FP-22 channels portion of tubes and vesicles and we measured their fluorescence recovery over time. As shown in figure 38, both FP-17 and FP-22 diffuse very rapidly within the vesicle; 15 sec after bleaching half of the fluorescence was already recovered (Fig. 38 A and B) and at the end of the experiments the intensity in the bleached region is approximately the same of the surrounding areas (right panels, Fig. 38 A). This behavior appears also clear from the recovery curves in Fig. 38 B, where the two proteins reached the equilibrium very rapidly. In addition, the calculation of half times and mobile fractions didn't reveal any significant difference by comparing neither the two fluorophores nor the two TMDs (Fig. 38 C). All the reconstituted proteins showed fluorescence recovery half times between 15 and 20 sec (left graph, Fig. 38 C) and about 80-90% is free to diffuse within the vesicle (right graph, Fig. 38 C).

By contrast, some differences were seen when a portion of tubes was bleached (yellow ROI, Fig. 39 A). First, we found that all proteins, probably because of the different geometry between tubes and vesicles, diffuse more slowly in lipid nanotubes compared to vesicles: indeed, 58 sec after bleaching about half of the fluorescence signal was recovered and the equilibrium was reached after 8-10 min (Fig. 39 A and B), indicating that the diffusion is slowed down about 4 times compared to vesicles. Moreover, quantitative analysis also revealed that the two fluorescent variants behave differently in term of velocity of diffusion: as shown in figure 39 B, both Tomato-17 and -22 diffuse slower and their fluorescence recovery curves are less sloped than those of mEGFP-17 and mEGFP-22. Statistical analysis confirmed that the fluorescence recovery half time of Tomato is significantly higher to that of mEGFP (left

graph, Fig. 39 C). In contrast, as demonstrated by the calculation of mobile fractions, at steady state the amount of Tomato that diffuses in the tube is the same of mEGFP (right graph, Fig. 39 C). Since all the experiments were performed at least 20 min after adding kinesins and GUVs in the flow chamber that is used for this assay, we are sure that our analysis was not altered by the fact that Tomato-17 and -22 diffuse more slowly than mEGFP-17 and -22. Concerning FP-17 and FP-22, even though FP-17 displayed a shorter half time and FP-22 a bigger mobile fraction (Fig. 39 C), no statistically significant differences were found in both cases, suggesting that the longer TMD does not diffuse faster in tubes compared to FP-17 and, thus, that is not preferentially sorted into highly curved domains.

4.11 FP-17 and FP-22 are homogenously distributed in tubes pulled out with optical tweezers and micropipette aspiration system

Since with the kinesins assay some outliers, in which FP-22 was enriched in highly curved domains were found and this assay didn't allow a strict control of the membrane tension and, thus, of the tube radius, we hypothesized that maybe in those outliers there was a specific membrane curvature that induced FP-22 sorting. To this aim, FP-17 and FP-22 distribution was investigated in tubes pulled out by combining the use of optical tweezers and a micropipette aspiration system. As described in section 3.12 and shown in Fig. 40 A and B, this technique is based on the aspiration of a GUV with a micropipette that is connected to a water reservoir and, by simply regulating water height in the reservoir, it is possible to regulate the sunction pressure applied to aspirate the vesicle. On the other hand, a streptavidin-coated bead is trapped by an optical tweezer. By contacting biotinylated lipid-containing GUV with a trapped bead and moving the GUV away from the trap a tube can be pulled out and, then, by increasing the aspiration force the membrane tension can be progressively increased (and the tube radius progressively decreases). Representative fluorescence levels of FP-17 and FP-22 are shown in Fig. 40 C. Upper panels displayed protein dis-

tribution in the first tension step after the tube has been pulled out; because the tube has a diameter under the optical resolution limit, the signal is always lower compared to the vesicle and decreases during each tension step because of the progressive reduction in the tube radius (lower panels, Fig. 40 C). Indeed, while in the vesicle is already clear by eye that FP-17 and FP-22 are equally distributed, in the tube is not so obvious because of the low fluorescent signal and quantitative analysis was required. Fluorescence analysis using a home-made routine for Matlab (from Bassereau lab, Institute Curie, Paris), revealed that FP-22 is not enriched in tubes during the progressive increase of the membrane tension compared to FP-17 and, indeed, the red trend line is flat, meaning that the sorting ratio didn't change with the tension (right graph, Fig. 40 D). As we did with the molecular motor assay, to be sure that the fluorescent proteins were not influencing TMD distribution we also compared mEGFP-17 with Tomato-17 and mEGFP-22 with Tomato-22. The fact that the sorting ratio didn't change with the progressive decrease of the tube radius by comparing the same TMD indicates that the fluorophore didn't alter the distribution of TMDs in flat and curved domains. Taken together, these data demonstrate that FP-22 is not preferentially partitioned into artificially curved domains.

5. FUGURES AND LEGENDS

Figure 21: ER to Golgi transport rate of ts045 VSV-G DxE-EGFP at 32°C. (A) NRK cell transfected with VSV-G DxE-EGFP construct for 24 h at the non permissive temperature of 39°C were imaged alive at 32°C. Immediately after shifting to the permissive temperature of 32°C, VSV-G is mostly localized in the ER (even though in the right cell VSV-G already partially localizes in the Golgi), but, then, it rapidly accumulates in the Golgi apparatus and in 12 min the ER distribution of VSV-G disappeared (5 and 12 min timepoints). At the later timepoints VSV-G is transported to the plasma membrane and, indeed, Golgi fluorescence progressively disappears and the intensity of the plasma membrane increases (20, 30 and 40 min timepoints) (scale bar = 10 μm). (B) Quantitative analysis showing that VSV-G is transported very rapidly to the Golgi apparatus; 12 min after shifting to the permissive temperature Golgi fluorescence intensity reaches the maximum value and then progressively decreases because of the transport to the plasma membrane (n = 11).

A

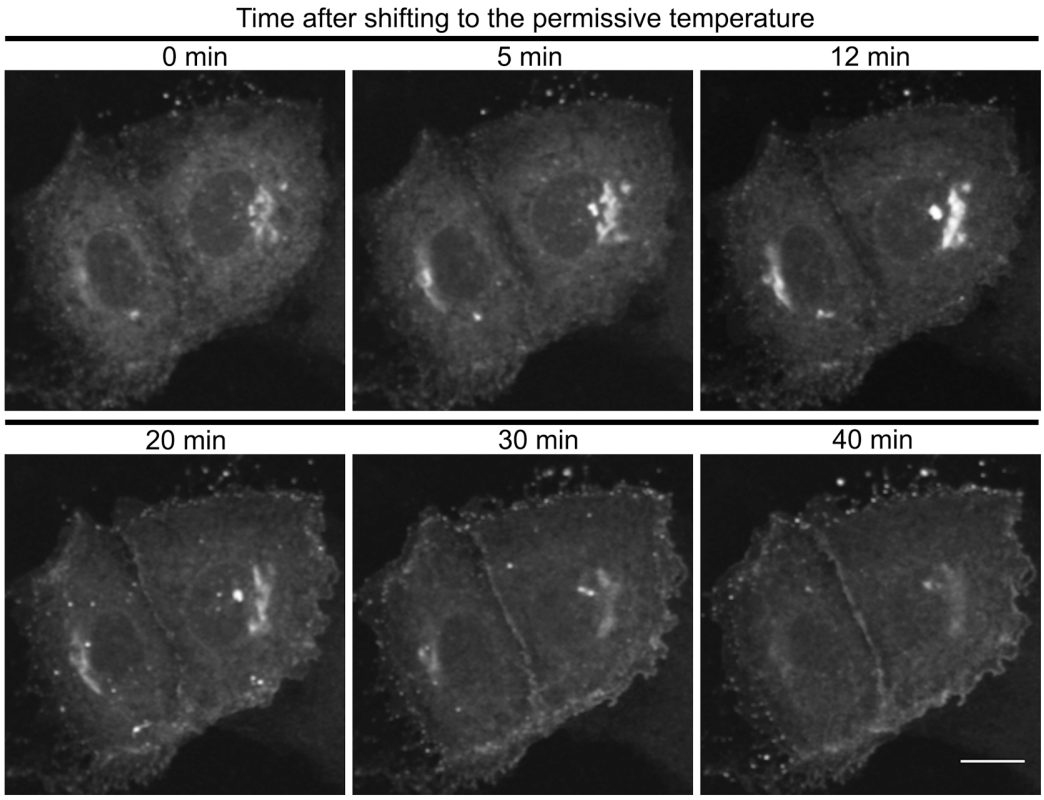
Time after shifting to the permissive temperature
0 min
5 min
12 min
20 min
30 min
40 min

B

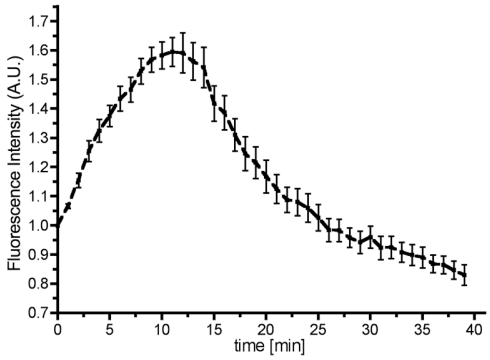
Fluorescence Intensity (A.U.)
1.7
1.6
1.5
1.4
1.3
1.2
1.1
1.0
0.9
0.8
0.7
0
5
10
15
20
25
30
35
40
time [min]

Figure 22: Anterograde transport of FP-22 at the ER-Golgi interface at 37°C. (A) Prebleach images show NRK cells expressing FP-22 and GalNAc-mCherry 1h after microinjection; arrowheads and red ROIs (in inset) indicate Golgi fractions of FP-22 that were bleached. After bleaching a rapid recovery of FP-22 Golgi fluorescence is observed and, indeed, a clear recovery can be seen 5 min after bleaching and it further increases until 20 min postbleach. At later timepoints a slow decrease of the Golgi fluorescence is observed because FP-22 transport proceeds to the plasma membrane, in which FP-22 signal can be detected in the latest timepoint (50 min) (scale bars = 10 μm). (B) Quantitative analysis revealed that after bleaching FP-22 Golgi fluorescence recovery is fast and reaches a peak after 15-20 min and then the fluorescence slowly decreases because FP-22 is delivered to the plasma membrane (n = 15).

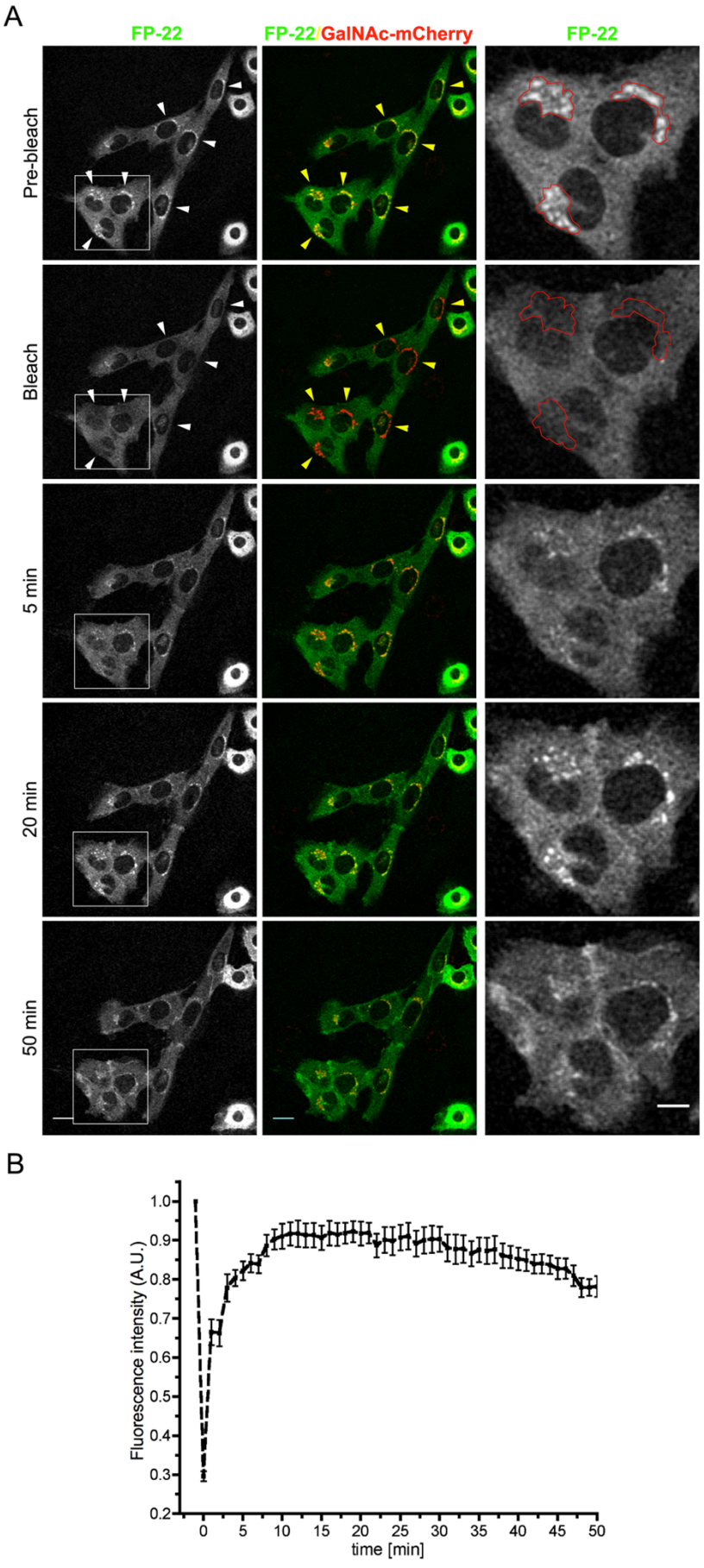
A
FP-22
FP-22/GalNAc-mCherry
FP-22
Pre-bleach
Bleach
5 min
20 min
50 min
B
Fluorescence intensity (A.U.)
1.0
0.9
0.8
0.7
0.6
0.5
0.4
0.3
0.2
0
5
10
15
20
25
30
35
40
45
50
time [min]

Figure 23: Intracellular localization of FP-22 and VSV-G DxE-EGFP upon incubation at 20°C for 2h. Co-microinjected cells with FP-22 and GalNAc-mCherry show that FP-22 is distributed between the ER and Golgi apparatus and, indeed, a partial co-localization with the Golgi marker GalNAc-mCherry is observed (upper panels). In contrast, NRK cells co-transfected with VSV-G DxE-EGFP and GalNAc-mCherry show a perfect co-localization between the two proteins and the absence of VSV-G in the ER (lower panels) (scale bars = 10 μm).

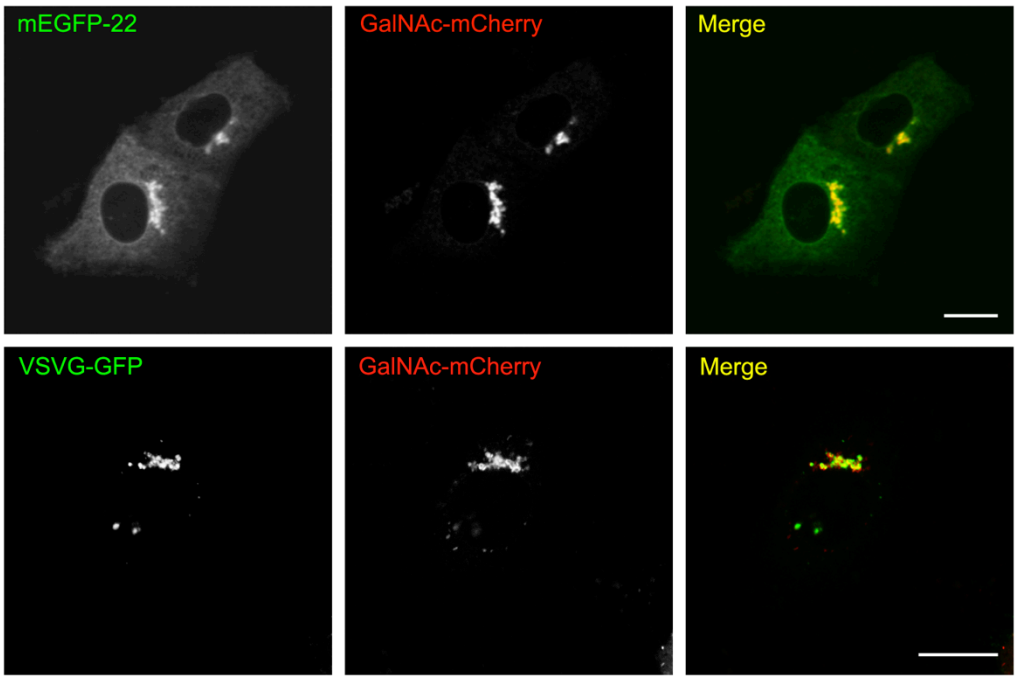
mEGFP-22
GalNAc-mCherry
Merge
VSVG-GFP
GalNAc-mCherry
Merge

Figure 24: VSV-G transport from the ER to the Golgi apparatus at 20°C. (A) NRK cells transfected with VSV-G DxE-EGFP and GalNAc-mCherry for 24h at the non-permissive temperature of 39°C were shifted at 20°C and imaged alive. At time 0 VSV-G is distributed in the ER and no co-localization with GalNAc-mCherry was observed; at later timepoints it started to accumulate in the Golgi (progressive increase in the co-localization with GalNAc-mCherry) and, simultaneously, the ER signal decreases (scale bars = 10 μm). (B) Quantitative analysis showing the progressive increase of VSV-G fluorescence in the Golgi apparatus and decrease in the ER when cells are incubated at 20°C (n = 27).

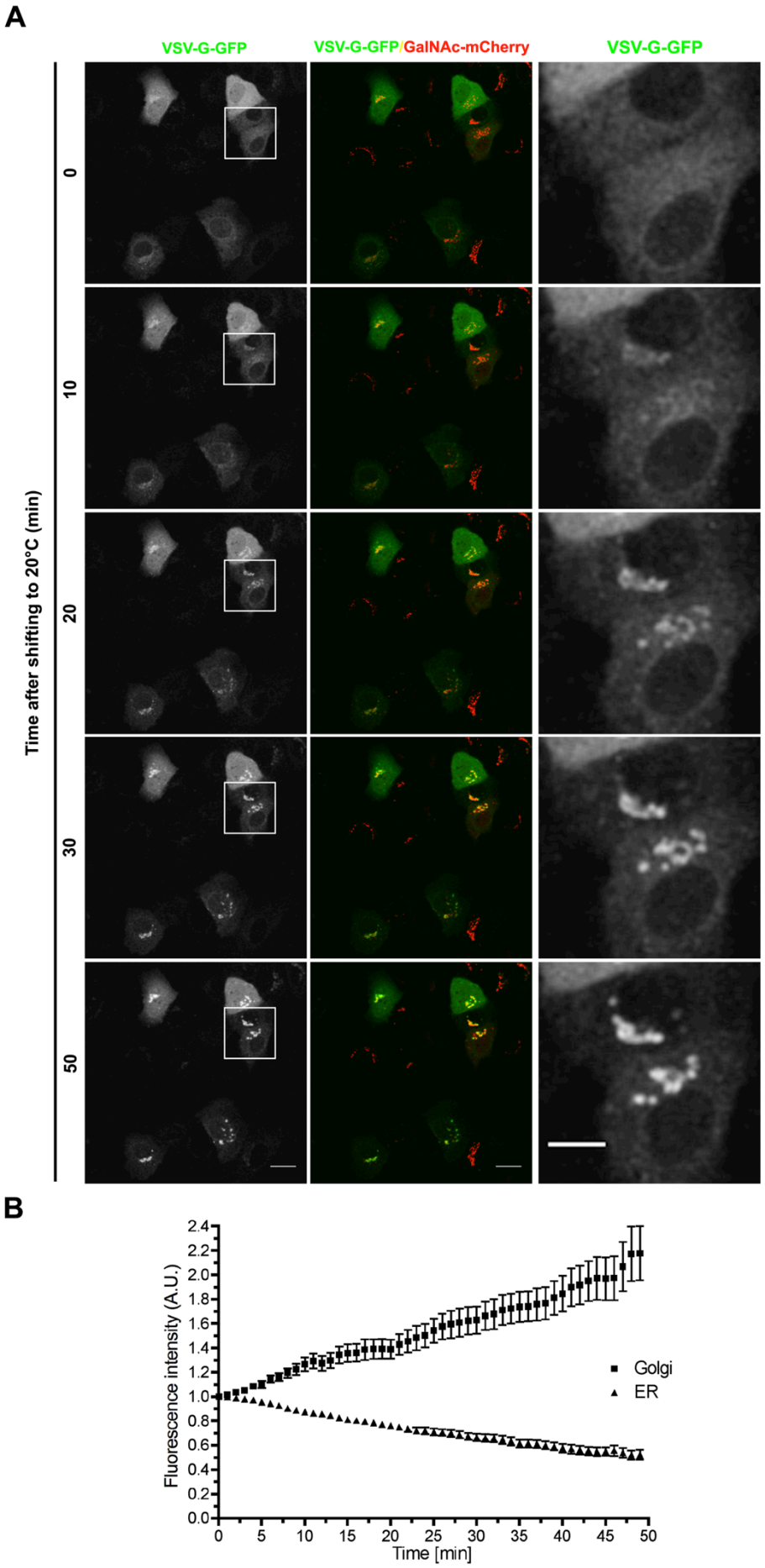
A
VSV-G-GFP
VSV-G-GFP/GalNAc-mCherry
VSV-G-GFP
Time after shifting to 20°C (min)
0
10
20
30
50
B
Fluorescence intensity (A.U.)
Time [min]
Golgi
ER

Figure 25: ER to Golgi transport and intrareticular diffusion of FP-22 at 20°C. (A) NRK cells co-microinjected with FP-22 and GalNAc-mCherry were incubated 1h at 37°C, 30 min at 20°C and imaged alive at the same temperature. FP-22 is initially distributed between the ER and the Golgi apparatus (co-localization with GalNAc-mCherry) (prebleach images). Arrowheads indicate bleached FP-22 Golgi fractions and the arrow indicates the bleached ER portion (red ROIs in inset, the upper ROI indicates the bleached ER region and the lower one the bleached Golgi region). 20 min after bleaching, a clear fluorescence recovery in the ER was observed and the signal no longer increased at later timepoints (40 and 60 min). In contrast, after Golgi bleaching only a partial recovery was found after 20 min, but FP-22 Golgi signal progressively increased even in the later timepoints until the end of the registration (60 min) (scale bars = 10 μm). (B) FRAP analysis showing the different fluorescent recovery in the ER (black squares) and Golgi (black circles). The ER recovers rapidly and reaches a plateau after 10-15 min (with a recovery of about 90% compared to the prebleach value), while the Golgi fluorescence recovers more slowly and the signal progressively increases in all timepoints until the end of the experiments (n = 17 for FRAP on Golgi and n = 7 for FRAP on ER).

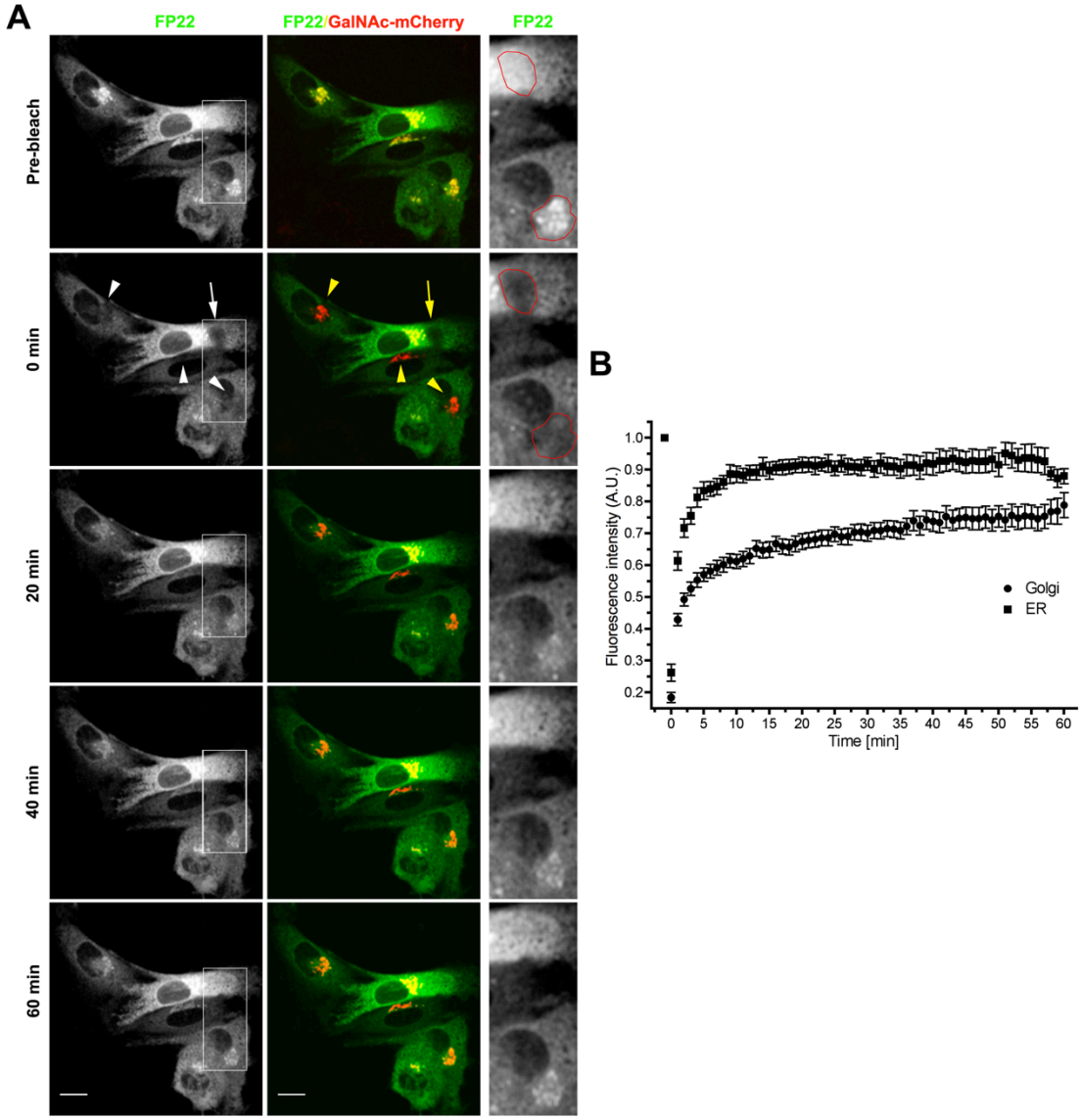
A
FP22
FP22/GalNAc-mCherry
FP22
Pre-bleach
0 min
20 min
40 min
60 min
B
Fluorescence intensity (A.U.)
1.0
0.9
0.8
0.7
0.6
0.5
0.4
0.3
0.2
0
5
10
15
20
25
30
35
40
45
50
55
60
Time [min]
Golgi
ER

Figure 26: ER to Golgi transport of FP-22 is inhibited in energy-depleted conditions at 20°C. (A) NRK cells co-microinjected with FP-22 and GalNAc-mCherry were incubated 1h at 37°C, 30 min at 20°C and imaged alive in the absence of energy at the same temperature. Yellow ROIs in prebleach and bleach images indicate bleached Golgi fractions of FP-22. After bleaching, a fluorescence recovery was observed in the first 20 min until the signal reached the same intensity of the surrounding ER and then Golgi fluorescence no longer increased in later timepoints (40 and 60 min). This can also be observed in merged images, where the Golgi apparatus, which was "yellow" before bleaching because of the co-localization with GalNAc-mCherry, remained only "red" because FP-22 didn't recover after bleaching (scale bar = 10 μm). (B) Quantitative analysis of Golgi recovery in the presence (black squares) and absence of energy (black circles); immediately after bleaching the two curves showed similar trends because the major contribution was given by intrareticular diffusion, but then, while in the presence of energy the Golgi fluorescence progressively recovered until the end of the registration, upon ATP depletion no fluorescence recovery was detected after the first 15-20 min (n = 8 for ATP depletion and n = 17 for controlled condition).

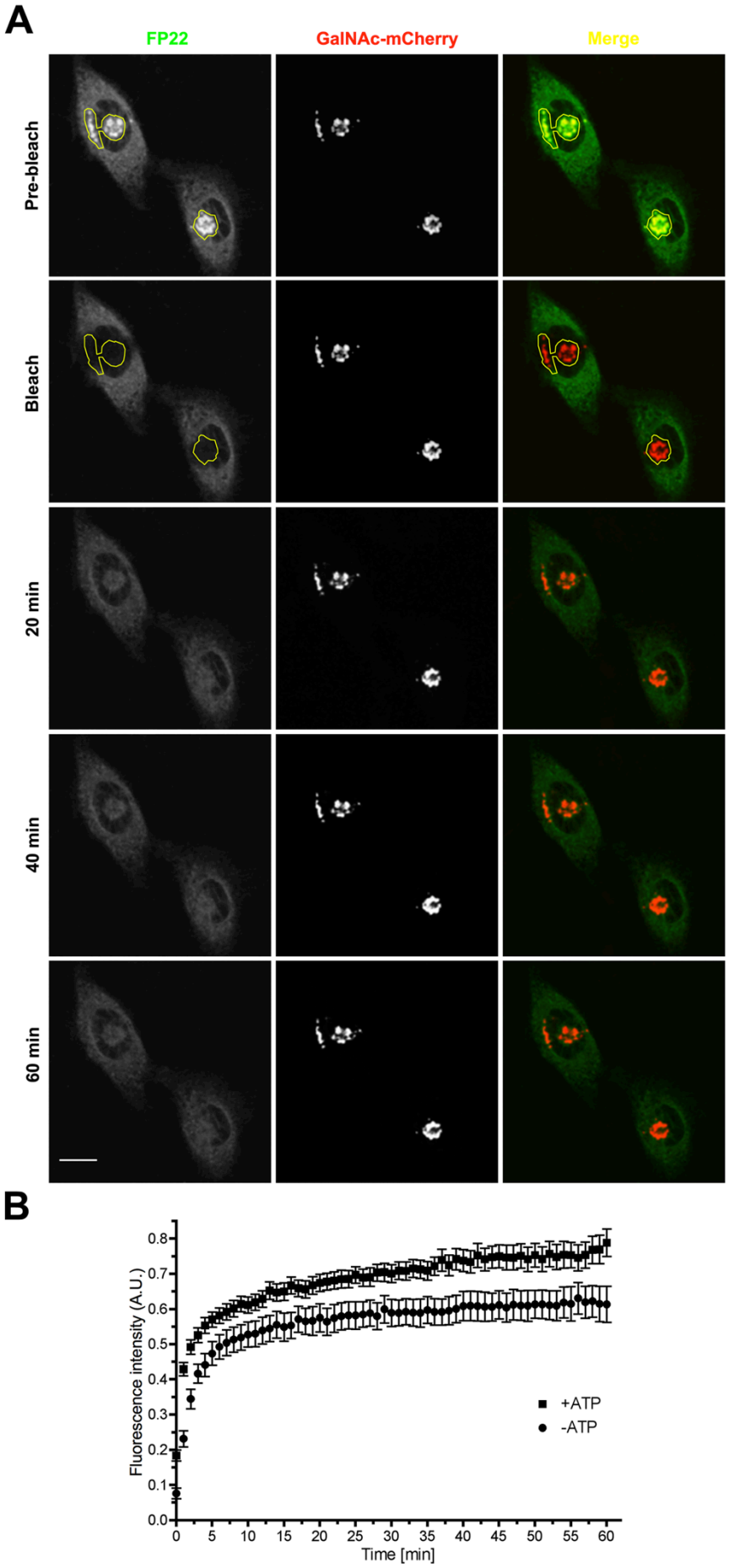
A
FP22
GalNAc-mCherry
Merge
Pre-bleach
Bleach
20 min
40 min
60 min
B
Fluorescence intensity (A.U.)
Time [min]
+ATP
-ATP

Figure 27: Fluorescence intensity profiles of FP-22 in the Golgi and ER in the presence and absence of energy. Fluorescence intensity along the white lines was measured in control conditions or upon ATP depletion before and 60 min after bleaching. Fluorescence images are reported in a pseudocolor scale where blue tones represent low intensities and green/red tones higher intensities. In the presence of ATP peaks corresponding to the Golgi apparatus are clearly distinguishable from the ER intensity both before and 60 min after bleaching (upper panels and graph). In energy-depleted conditions, the Golgi intensity after bleaching is no longer distinguishable to that of the surrounding ER and, indeed, it has the same intensity of the ER fluorescence level (lower panels and graph) (scale bars = 10 μm).

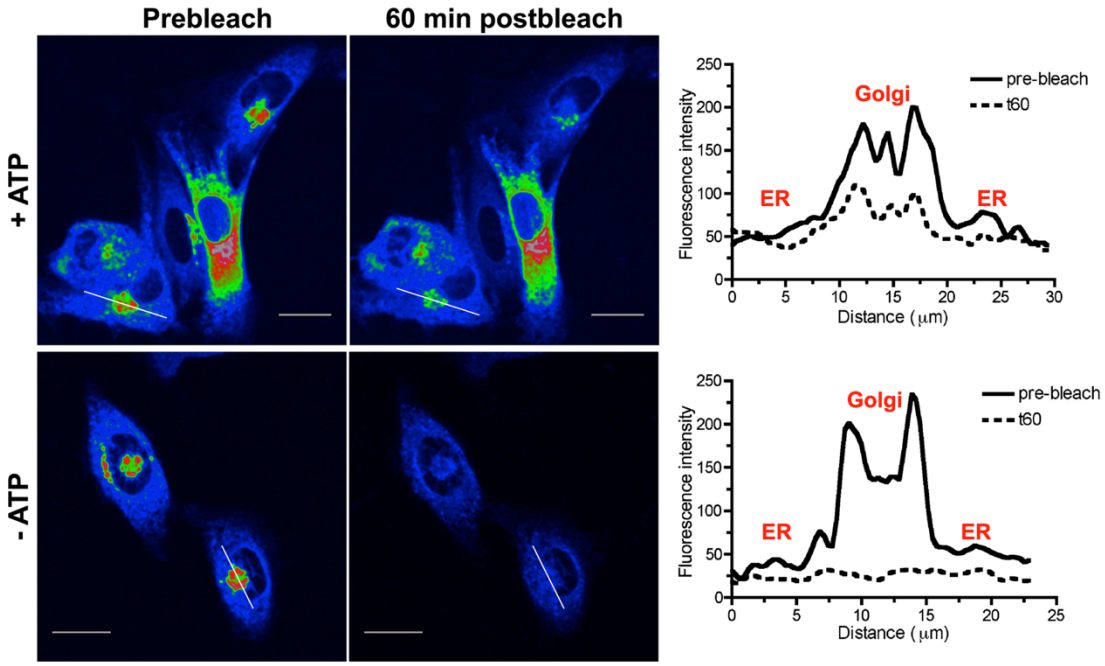
Prebleach
60 min postbleach
+ ATP
- ATP
Golgi
ER
ER
pre-bleach
t60
Fluorescence intensity
Distance (μm)
Golgi
ER
ER
pre-bleach
t60
Fluorescence intensity
Distance (μm)

Figure 28: FP-22 recycles from the Golgi to the ER at 20°C. (A) NRK cells co-microinjected with FP-22 and GalNAc-mCherry were incubated 1h at 37°C, 30 min at 20°C and imaged alive at the same temperature. Before bleaching FP-22 is distributed between the ER, as demonstrated by the co-localization with the ER marker RFP-KDEL, and the Golgi, which corresponds to the intense fluorescence in the perinuclear region. After bleaching the ER fraction of FP-22 (indicated by red ROIs) a progressive emptying of the Golgi fluorescence and a recovery of the ER were observed until the latest timepoint (60 min). Insets show a more detailed temporal sequence of FP-22 Golgi fluorescence, which was constant before bleaching and progressively decreases as soon as the ER fraction was bleached (scale bars = 10 μm and 5 μm in insets). (B) Left graph displays ER and Golgi fluorescent changes over time of the experiment showed in (A). Before bleaching FP-22 Golgi fluorescence (black squares) was stable, but then rapidly decreased of about 45% during 60 min of registration and, conversely, the ER (black circles) recovered with the opposite slope to that of the Golgi fluorescence (n = 12). Right graph shows the anterograde (black circles) and retrograde (black squares) transport rates of FP-22, analyzed by Golgi and ER bleaching, respectively. After Golgi bleaching, there is a progressive recovery of the signal, while after ER bleaching, the Golgi apparatus progressively empties. Since the two curves display specular slopes, the analysis suggests that the anterograde and retrograde transports occur with similar kinetics (n = 17 for anterograde transport and n = 12 for retrograde).

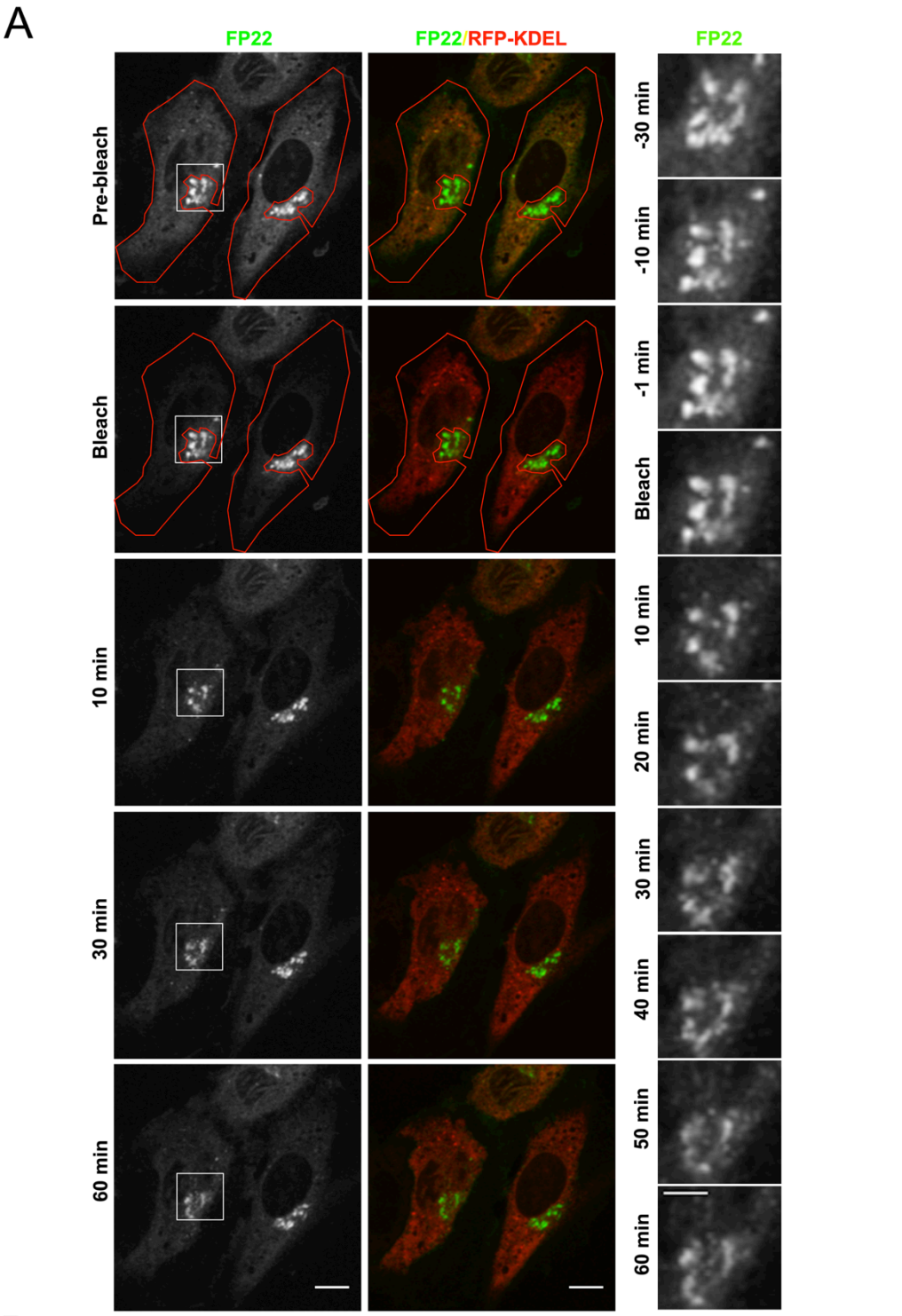
A
FP22
FP22/RFP-KDEL
FP22
Pre-bleach
Bleach
10 min
30 min
60 min
-30 min
-10 min
-1 min
Bleach
10 min
20 min
30 min
40 min
50 min
60 min
B
Fluorescence Intensity (A.U.)
time [min]
Golgi
ER
Fluorescence intensity (A.U.)
time [min]
Retrograde
Anterograde

Figure 29: FP-22 is recycled from the Golgi apparatus to the ER at 37°C. (A) NRK cells co-microinjected with FP-22 and GalNAc-mCherry were incubated 1h at 37°C and imaged alive at the same temperature. As already showed in Fig. 22, before bleaching FP-22 is distributed between the ER (co-localization with RFP-KDEL) and the Golgi apparatus. The red ROI indicates the bleached region corresponding to the ER fraction of FP-22. After ER bleaching, there was a progressive decrease of the Golgi fluorescence over time and a tubular structure, showed in inset (5 min) and indicated by the arrowhead, leaving the Golgi apparatus was also observed. In addition, in unbleached cell (lower left cell) the Golgi fluorescence was stable over time, suggesting that the observed decrease of the Golgi fluorescence in bleached cell was due to retrograde transport and not to trafficking from the Golgi to the plasma membrane (scale bars = 10 μm and 5μm in inset). (B) Quantitative analysis confirmed the progressive decrease of FP-22 Golgi fluorescence after ER bleaching (n = 8).

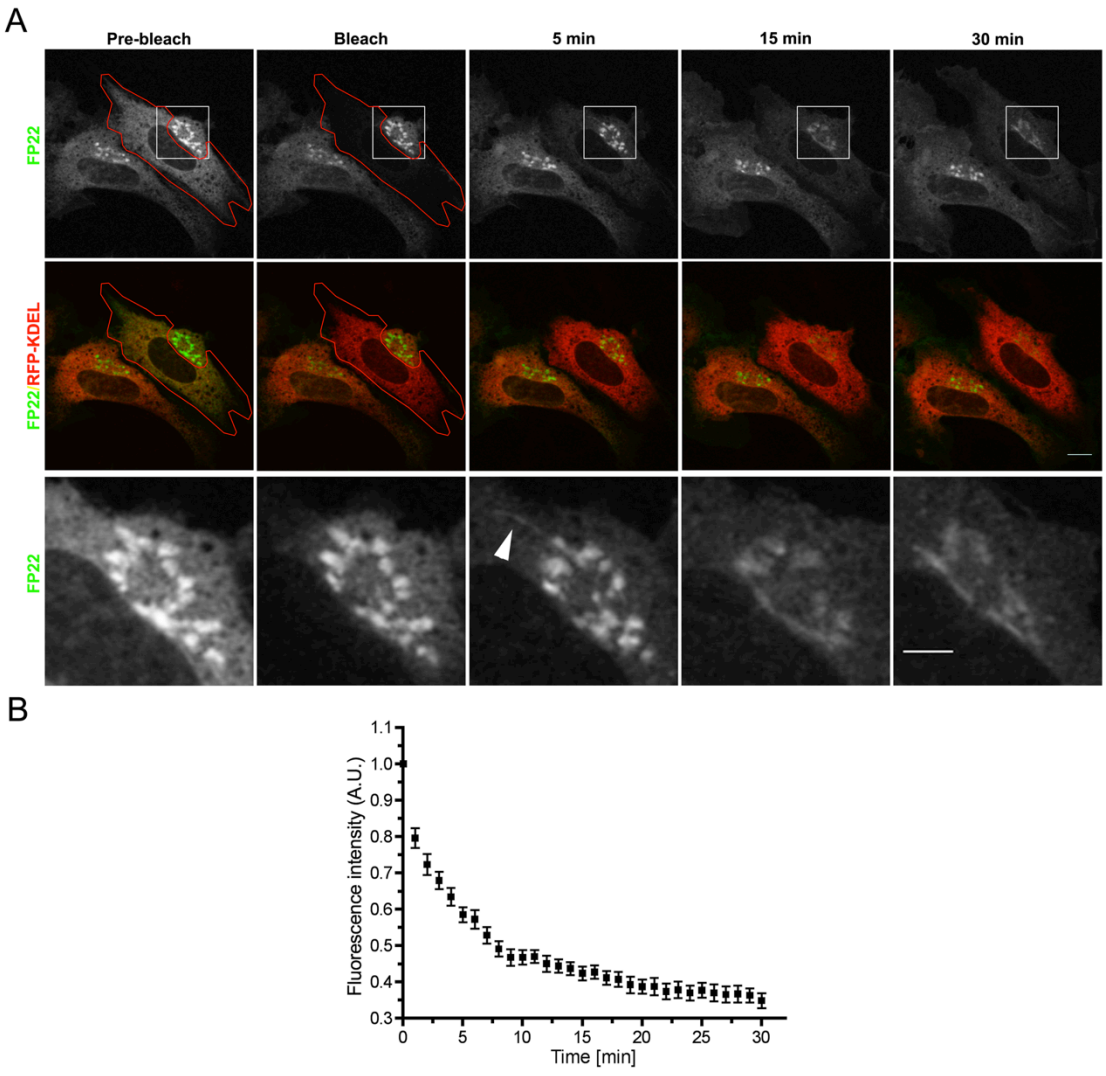
A
Pre-bleach
Bleach
5 min
15 min
30 min
FP22
FP22 RFP-KDEL
FP22
B
Fluorescence intensity (A.U.)
Time [min]
1.1
1.0
0.9
0.8
0.7
0.6
0.5
0.4
0.3
0
5
10
15
20
25
30

Figure 30: Topology of ts045VSV-G AxA and its localization after transfection at the permissive temperature. (A) The di-acidic export signal in the cytosolic tail of the protein was replaced by site-directed mutagenesis with two alanines. VSV-G is a type I transmembrane protein and contains a single TMD and an N-terminus domain exposed in the ER lumen. (B) After transfection for 24h at the permissive temperature of 32°C VSV-G AxA shows a typical plasma membrane distribution without any ER or Golgi localization (scale bar = 10 μm).

A

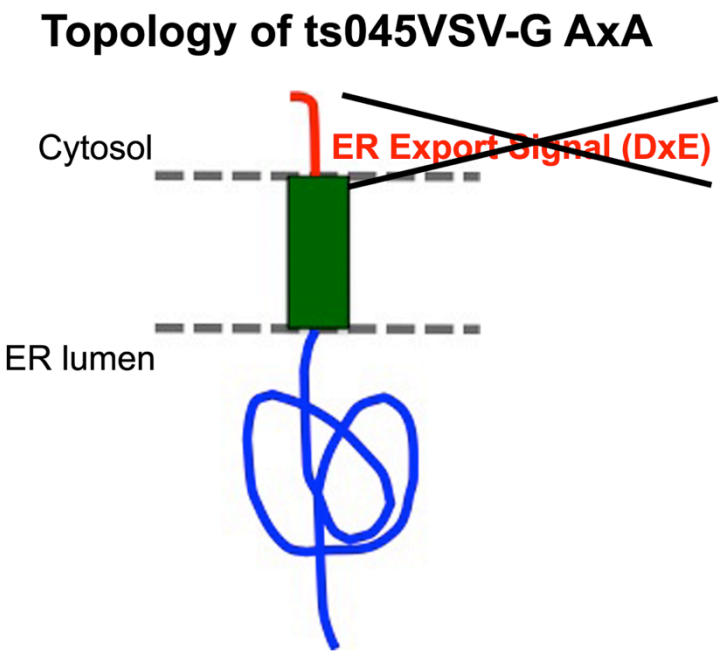
Topology of ts045VSV-G AxA
Cytosol
ER Export Signal (DxE)
ER lumen

B

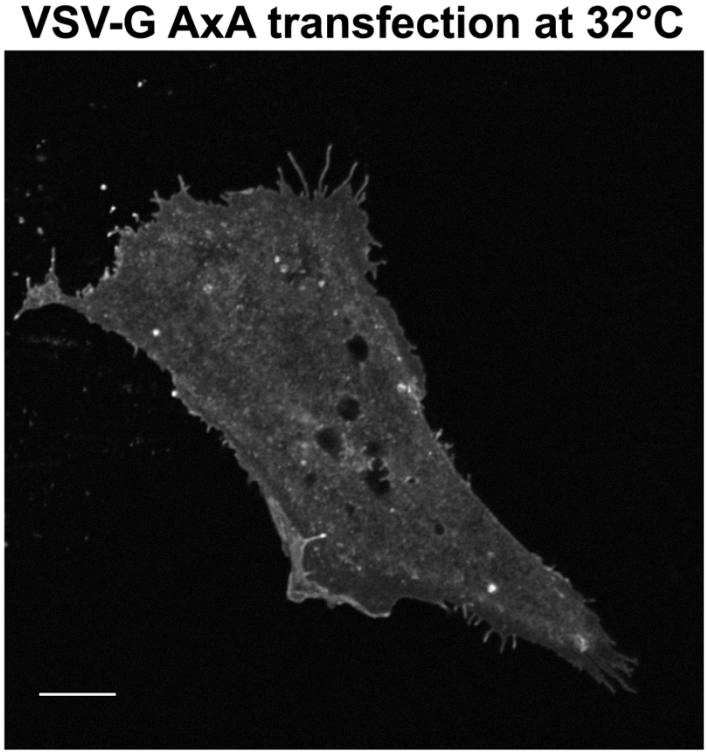
VSV-G AxA transfection at 32°C

Figure 31: VSV-G AxA is recycled from the Golgi apparatus to the ER at 20°C. (A) NRK cells were transfected with VSV-G AxA-EGFP and GalNAc-mCherry for 24 h at 39°C, incubated for 30 min at 20°C and then imaged alive at the same temperature. At 20°C VSV-G AxA is distributed between the ER and the Golgi (co-localization with GalNAc-mCherry in prebleach images). The red ROI indicates bleached area. After bleaching the ER portion of VSV-G AxA, a progressive decrease of Golgi fluorescence was observed over time, while in the unbleached cell the fluorescent signal in the Golgi remained constant until the end of the registration. In merged images the decrease of Golgi fluorescence can be perceived by the fact that Golgi apparatus becomes "more red" over time (scale bar = 5 μm). (B) Quantitative analysis shows that Golgi fluorescence of VSV-G AxA (black squares) is stable over time before bleaching and, then, progressively diminishes after bleaching. Golgi emptying is accompanied by a progressive fluorescence recovery in the ER (black circles), whose curve has a specular slope compared to that of the Golgi decrease (n = 13).

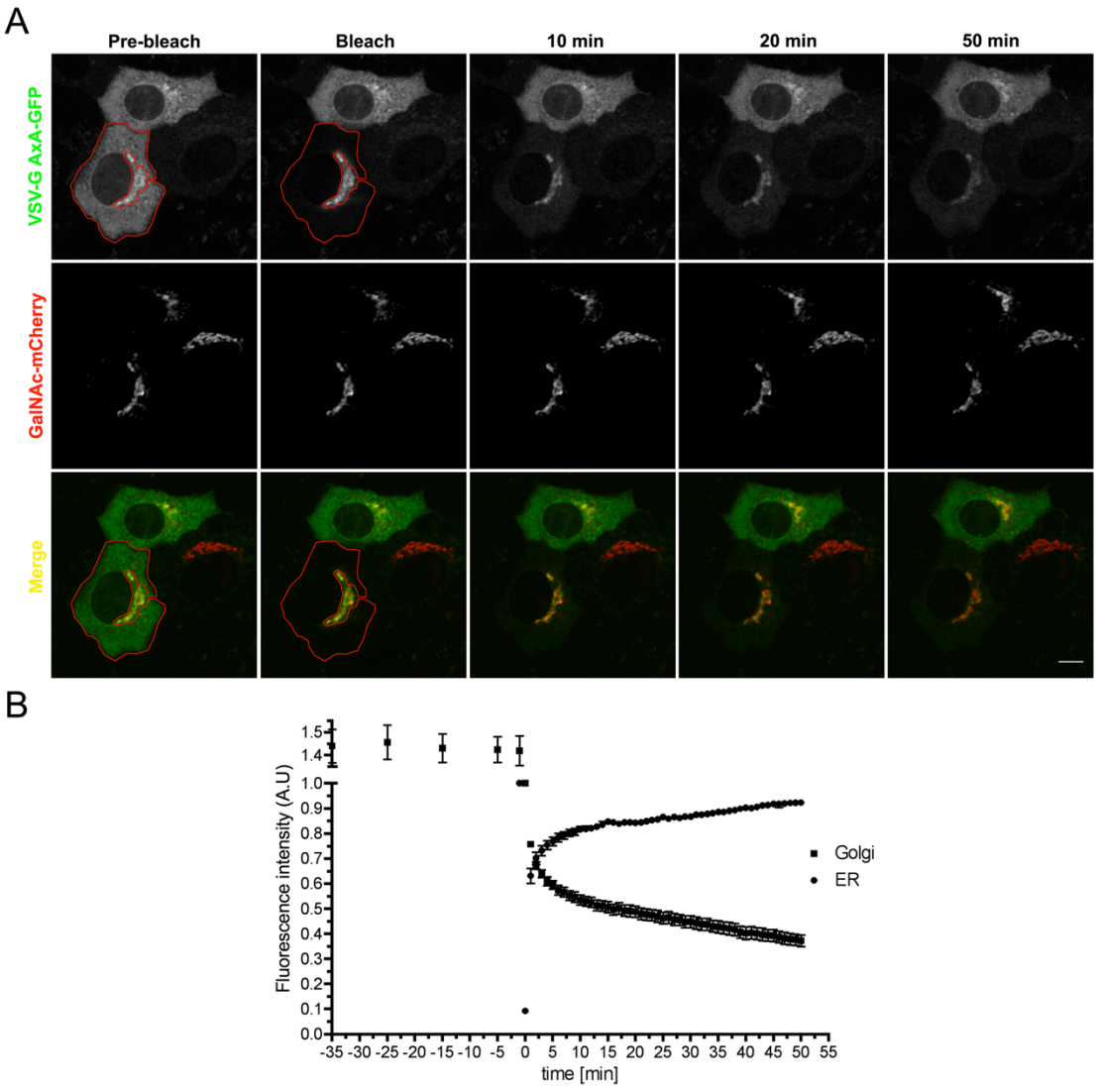
A
Pre-bleach
Bleach
10 min
20 min
50 min
VSV-G AxA-GFP
GalNAc-mCherry
Merge
B
Fluorescence intensity (A.U)
time [min]
Golgi
ER

Figure 32: Intracellular localization of different spectral variants of FP-17 and FP-22 and corresponding bacterially purified recombinant proteins on SDS-PAGE. (A) CV1 cells were transfected with FP-17 or FP-22 for 24 h with Calcium Phosphate method. All FP-17 fluorescent variants show a typical ER distribution, in which the nuclear envelop can be observed in some cases (Venus-17 and mEGFP-17) depending on the focus plane that was chosen for image acquisition. By contrast, FP-22 variants are all localized to the plasma membrane (scale bar = 10 μm). (B) The same fluorescent variants were purified from bacteria with the GST-fusion system and checked on SDS-PAGE. In all cases a shift in the molecular weight between FP-17 and FP-22 was observed, even though it was clearer for Venus and mEGFP fluorescent variants. Tomato-17 and -22 are approximately twice bigger than other variants, because the fluorescence protein Tomato is not monomeric but is composed of two fluorescent proteins linked together to form a tandem dimer. During the purification process a certain amount of degradation was obtained and corresponds to the lower bands. In all lanes a band of 70 kDa was observed and corresponds to the bacterial cytosolic chaperone Hsp70.

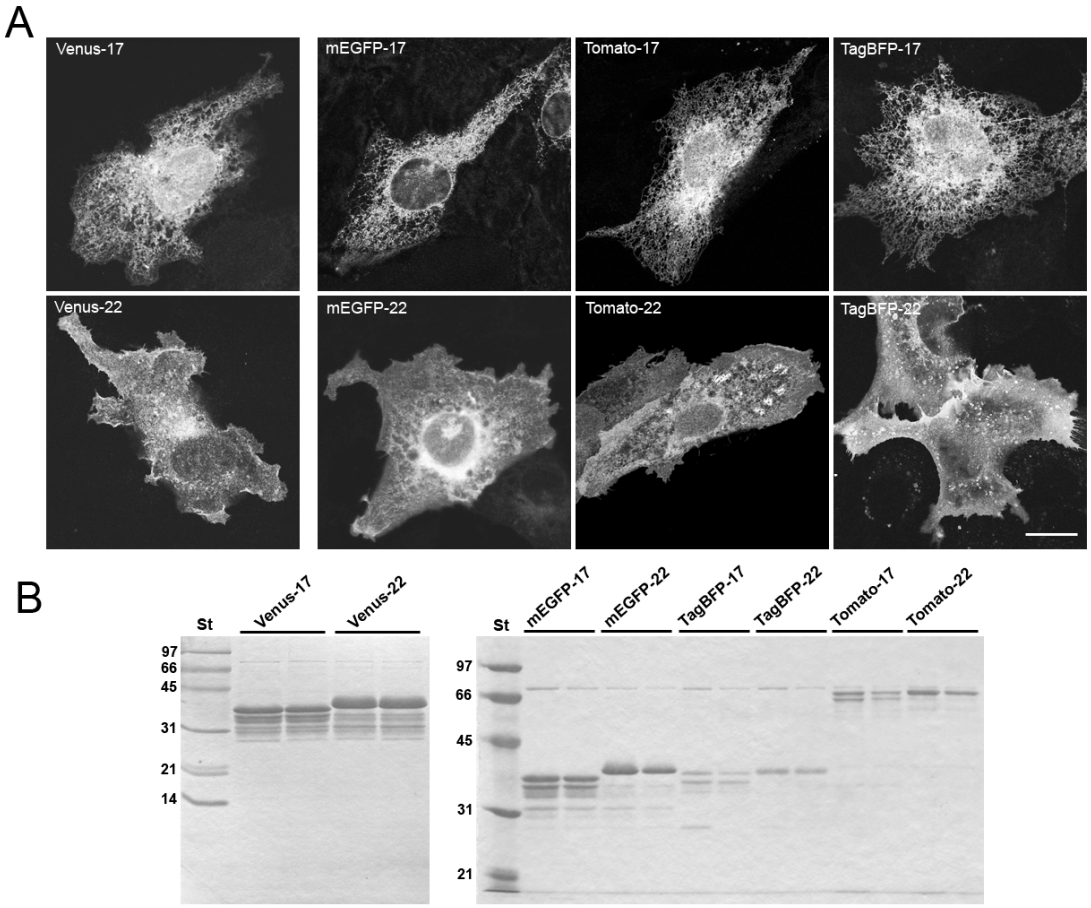
A
Venus-17
mEGFP-17
Tomato-17
TagBFP-17
Venus-22
mEGFP-22
Tomato-22
TagBFP-22
B
St
Venus-17
Venus-22
97
66
45
31
21
14
St
mEGFP-17
mEGFP-22
TagBFP-17
TagBFP-22
Tomato-17
Tomato-22
97
66
45
31
21

Figure 33: Morphological and biochemical characterization of reconstituted LUVs. (A) Electron micrographs of negatively stained liposomes without protein or containing FP-17 and/or FP-22. In all samples a homogenous round-shaped population of liposomes was observed, even though some heterogeneity in size within the same sample and between different experimental groups was found (scale bar = 500 nm). (B) Reconstituted proteoliposomes or purified proteins were treated with sodium carbonate, layered under a discontinuous sucrose gradient and collected fractions were analyzed by Western Blot with an αGFP antibody. Only in proteoliposomes the full-length form of both FP-17 and FP-22 float into the light fractions of the gradient, indicating a tight integration in the bilayer. Indeed, the two proteins alone remain in the heavy fractions in the tube bottom. In both proteoliposomes and proteins alone the shift in the molecular weight between FP-17 and FP-22 was detected.

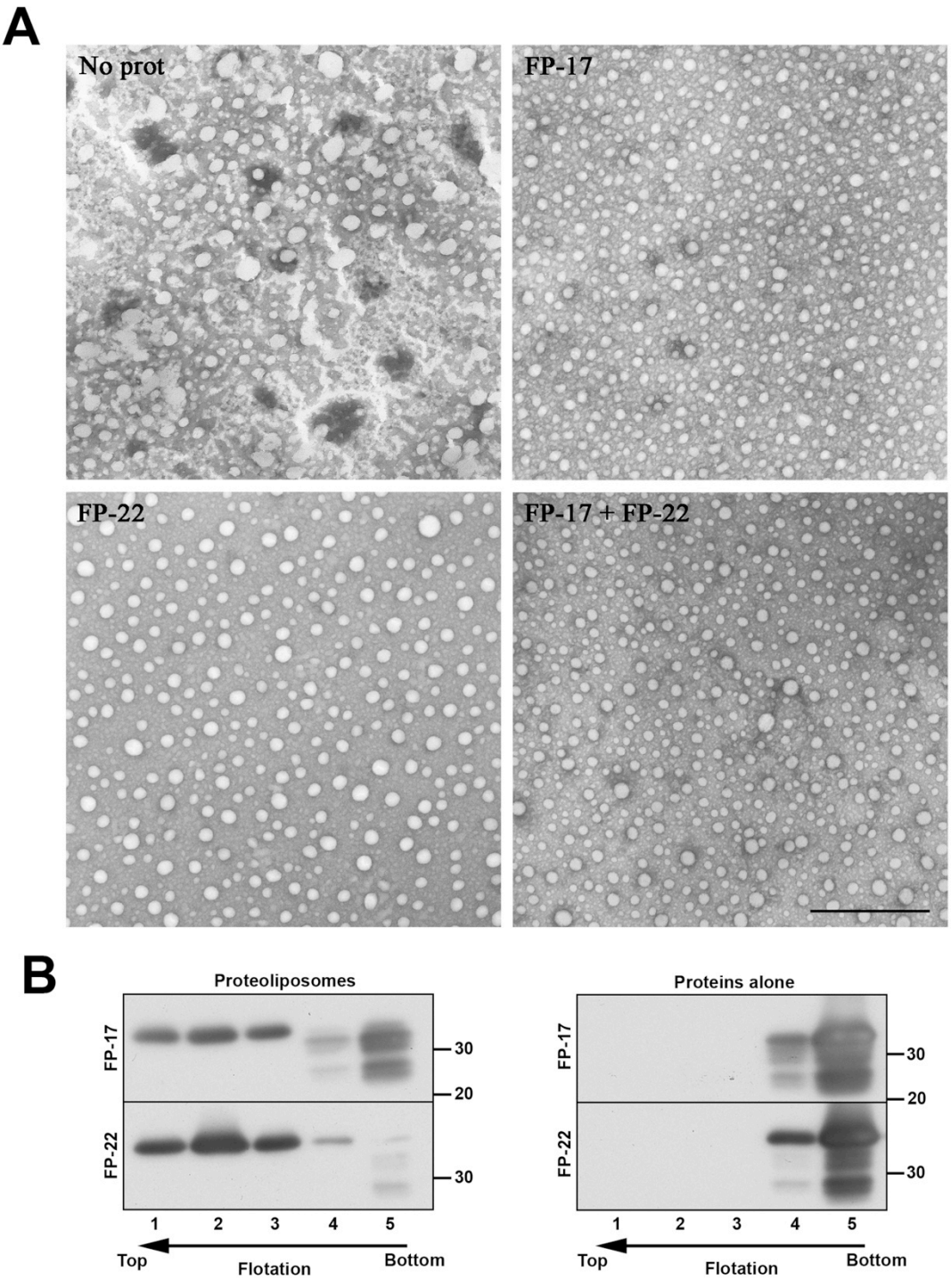
A
No prot
FP-17
FP-22
FP-17 + FP-22
B
Proteoliposomes
Proteins alone
FP-17
FP-22
30
20
30
1
2
3
4
5
Top
Flotation
Bottom

Figure 34: Reconstituted Giant Unilamellar Vesicles with FP-17 and FP-22 observed in phase contrast. Since the electroformation method we used to grow GUVs is based on the swelling, under an alternate electric field, of lipids that were previously dried under vacuum, at the microscope GUVs appeared layered in the growth chamber, with small vesicles in the lower focus plane (close to the glass surface of the slide) and progressively bigger vesicles in higher focus planes (scale bar = 20 μm).

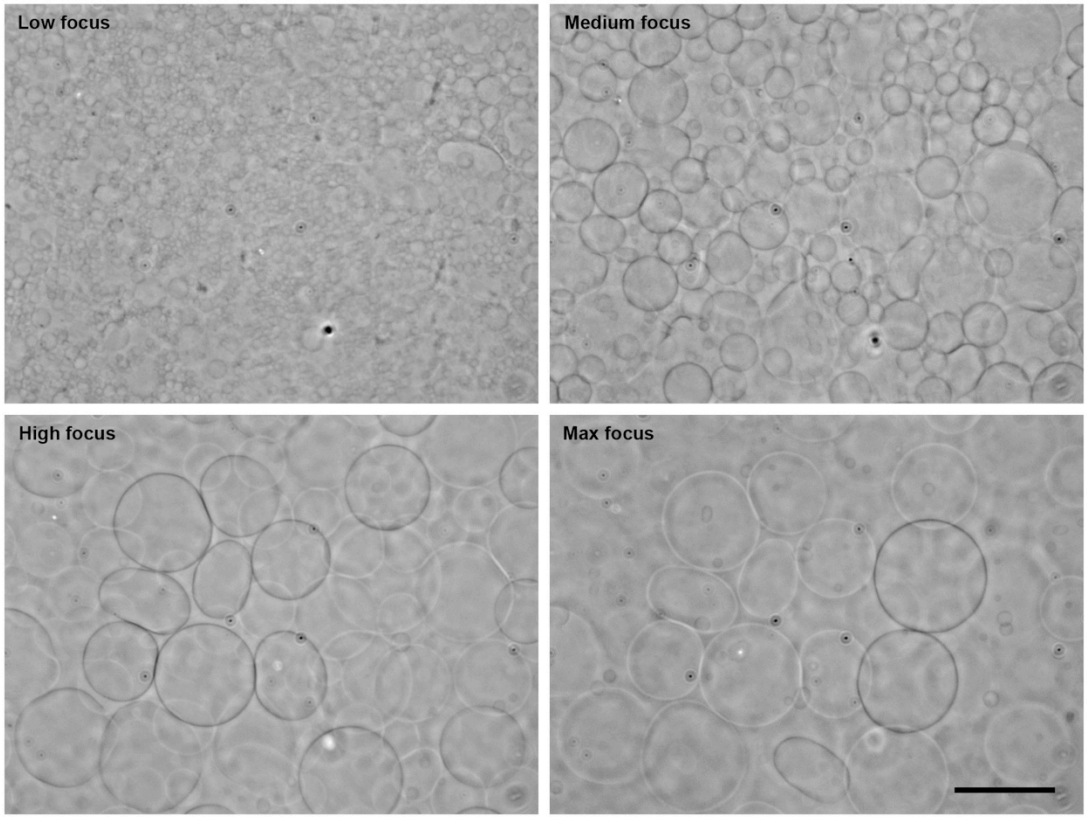
Low focus
Medium focus
High focus
Max focus

Figure 35: (A) Schematic picture representing kinesin assay. In the presence of ATP, biotinylated kinesins move along *in vitro* polymerized MTs and pull out lipid nano-tubes (average radius of 20 nm) thanks to presence of biotinylated lipids in GUVs (average radius of 10-40 μm) and of streptavidin that bridges biotinylated kinesins to biotinylated lipids (from Bruno Goud's laboratory). (B) Fluorescent MT networks of *in vitro* polymerized MTs attached to the coverslip of the flow chamber used for the kinesin assay (scale bar = 20 μm).

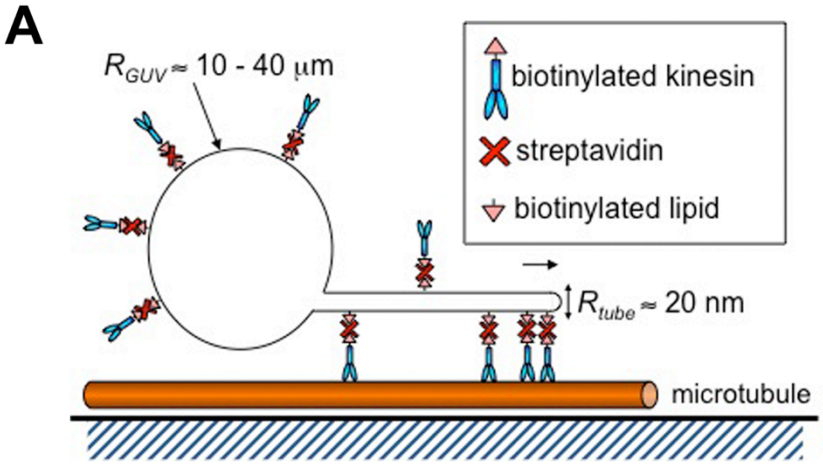

B ***In vitro*** **polymerized microtubules**

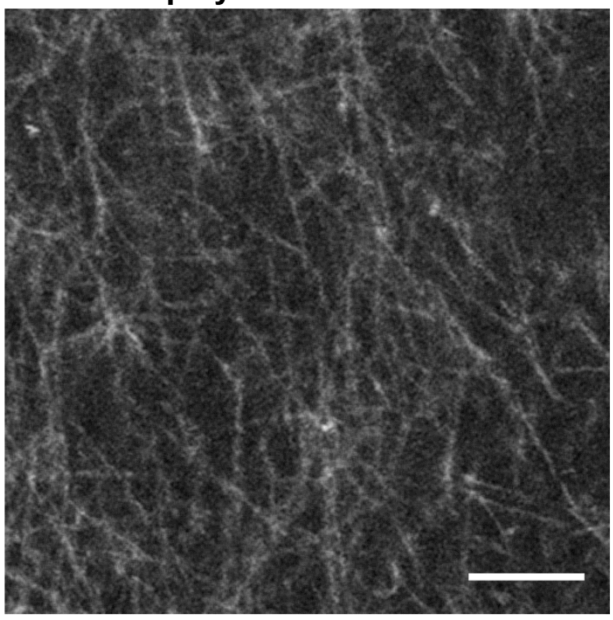

Figure 36: (A) Representative images of a tube network pulled by molecular motors from GUV reconstituted with FP-17 and FP-22 together. In upper panels the distribution of FP-17 and FP-22 in the equatorial plane of the vesicle is shown; both proteins are uniformly distributed within the vesicle as demonstrated by the perfect merge. Lower panels show the tube network pulled out from the bottom of the same vesicle. Tubes are less intense compared to the vesicle because of their smaller size. FP-17 and FP-22 distribution is heterogeneous with some tubes that seem to contain more FP-17 (top right field) and some others more FP-22 (bottom left field) (scale bar = 10 μm). (B) Figure summarizing the quantification method that was used to analyze the distribution of FP-17 and FP-22 in GUVs and nanotubes. The first panel shows FP-22 fluorescence in tube plane after background subtraction. Secondly, a threshold based on fluorescence intensity was applied and a ROI around the network was drawn to create a mask highlighting only the tubes (second panel on the left); finally the mask was superimposed to the original images and the mean fluorescence intensity was measured (scale bar = 10 μm).

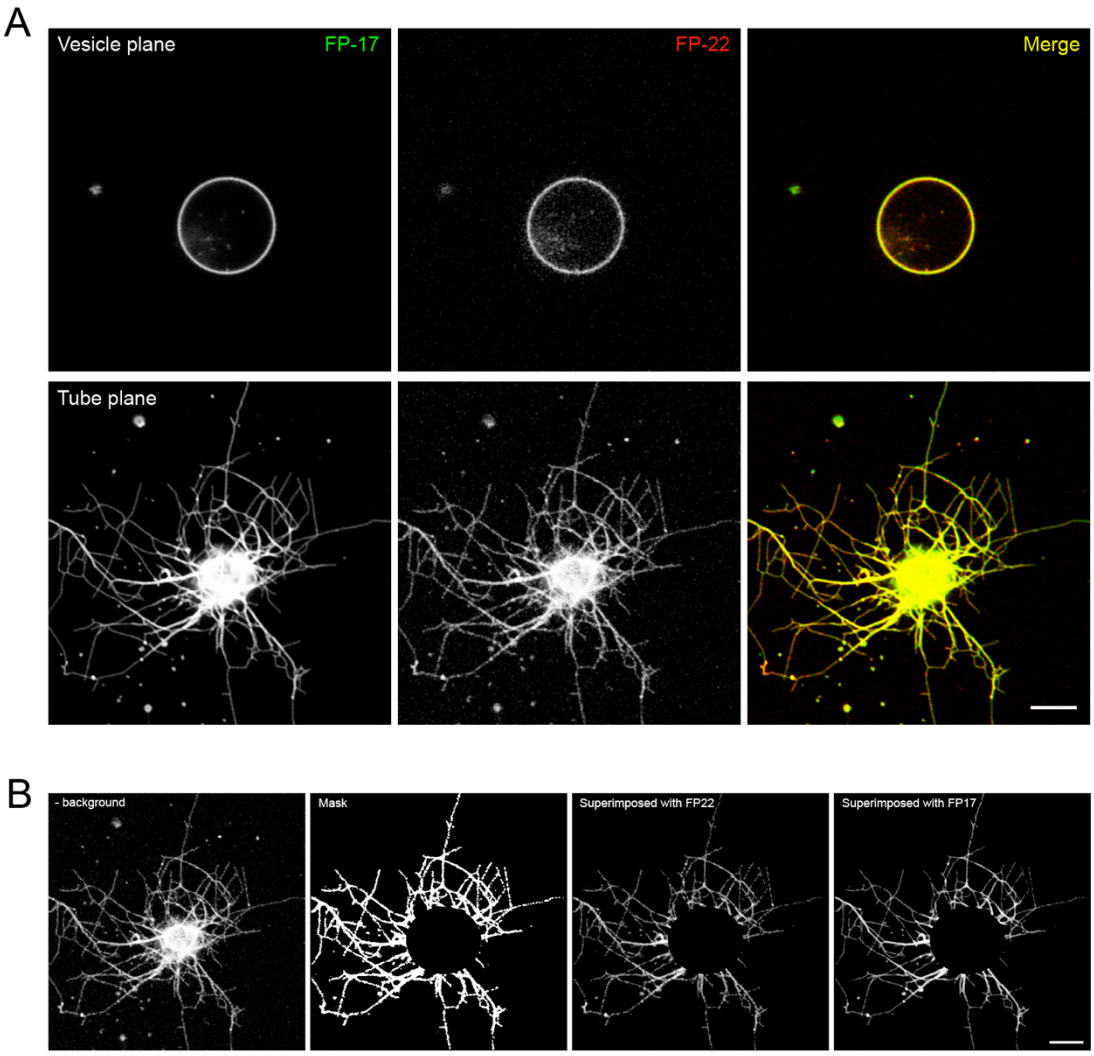
A
Vesicle plane
FP-17
FP-22
Merge
Tube plane
B
- background
Mask
Superimposed with FP22
Superimposed with FP17

Figure 37: Quantitative analysis of the distribution of FP-17 and FP-22 in lipid nanotubes and in GUVs. (A) No statistical differences in the mean fluorescent ratio of FP-22 over FP-17 between vesicles and tubes were observed in GUVs/tubes composed of POPC (left graph). Right graph shows the sorting ratio distribution of each network; even though most of them displayed a ratio around 1, one outlier with an enrichment of FP-22 in tubes was observed (n = 35). (B) As in vesicles composed of POPC only, the mean fluorescent ratio of FP-22 over FP-17 in liposomes composed of ER lipids extracted from rat liver microsomes is the same between vesicles and tubes either when mEGFP-17 and Tomato-22 was compared (left upper graph) or when the inverted fluorescent couple was used (left lower graph). Again, when the distribution of the sorting ratio was analyzed two outliers, in the case of mEGFP-17/Tomato-22, and one outlier with the inverted couple, were found and they all show an enrichment of FP-22 in tubes (n= 35 for mEGFP-17/Tomato-22 and n = 16 for mEGFP-22/Tomato-17). (C) The left graph shows the mean fluorescence ratio of FP-22 over FP-17 of all the data collected and presented in (A) and (B); no differences were observed between vesicles and tubes. Indeed, most networks have a sorting ratio around 1, even though some outliers showing an enrichment of FP-22 in the tubes were observed (right graph) (n = 86).

A

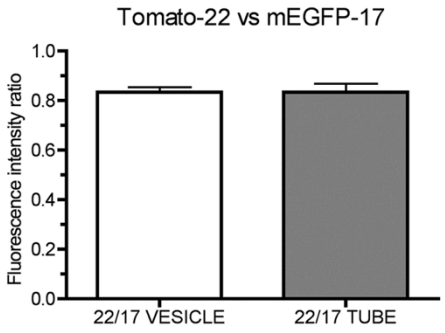
Tomato-22 vs mEGFP-17
Fluorescence intensity ratio
1.0
0.8
0.6
0.4
0.2
0.0
22/17 VESICLE
22/17 TUBE

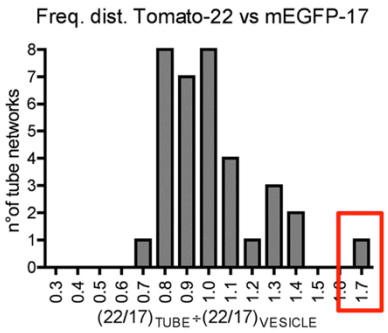
Freq. dist. Tomato-22 vs mEGFP-17
n°of tube networks
8
7
6
5
4
3
2
1
0
0.3 0.4 0.5 0.6 0.7 0.8 0.9 1.0 1.1 1.2 1.3 1.4 1.5 1.6 1.7
(22/17)TUBE÷(22/17)VESICLE

B

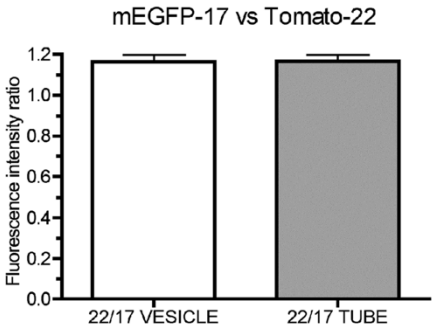
mEGFP-17 vs Tomato-22
Fluorescence intensity ratio
1.2
1.0
0.8
0.6
0.4
0.2
0.0
22/17 VESICLE
22/17 TUBE

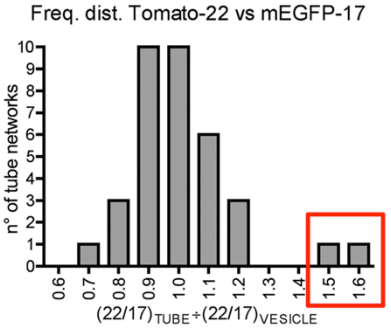
Freq. dist. Tomato-22 vs mEGFP-17
n° of tube networks
10
9
8
7
6
5
4
3
2
1
0
0.6 0.7 0.8 0.9 1.0 1.1 1.2 1.3 1.4 1.5 1.6
(22/17)TUBE÷(22/17)VESICLE

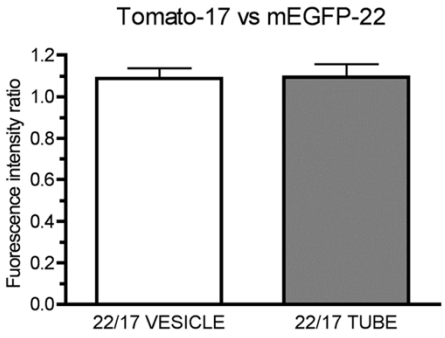
Tomato-17 vs mEGFP-22
Fuorescence intensity ratio
1.2
1.0
0.8
0.6
0.4
0.2
0.0
22/17 VESICLE
22/17 TUBE

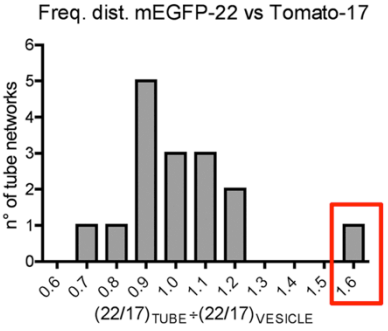
Freq. dist. mEGFP-22 vs Tomato-17
n° of tube networks
6
5
4
3
2
1
0
0.6 0.7 0.8 0.9 1.0 1.1 1.2 1.3 1.4 1.5 1.6
(22/17)TUBE÷(22/17)VESICLE

C

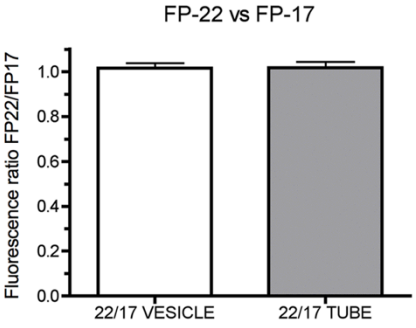
FP-22 vs FP-17
Fluorescence ratio FP22/FP17
1.0
0.8
0.6
0.4
0.2
0.0
22/17 VESICLE
22/17 TUBE

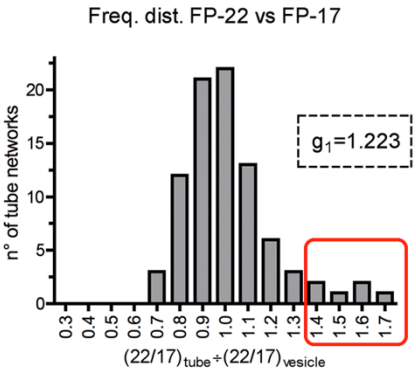
Freq. dist. FP-22 vs FP-17
n° of tube networks
20
15
10
5
0
g1=1.223
0.3 0.4 0.5 0.6 0.7 0.8 0.9 1.0 1.1 1.2 1.3 1.4 1.5 1.6 1.7
(22/17)tube÷(22/17)vesicle

Figure 38: Diffusion of FP-17 and FP-22 in reconstituted GUVs composed of ER lipids extracted from rat liver microsomes. (A) A portion of the vesicle was bleached in both FP-17 and FP-22 channels and their fluorescent recovery was followed over time. Images 15 sec after bleaching show a fast fluorescent recovery in the bleached area that, indeed, reaches about the same intensity of the prebleach values after 250 sec. (B) Fluorescent recovery curves have similar trends between the fluorescent proteins that were analyzed, even though Tomato-17 seems to diffuse more slowly (n = 10 for each fluorescent protein). (C) However calculation of fluorescent half time recovery (left histogram) didn't display any statistically significant difference neither between different fluorescent proteins nor between different TMD lengths. Like half times, no difference in the mobile fractions were observed between fluorescent proteins and TMD lengths.

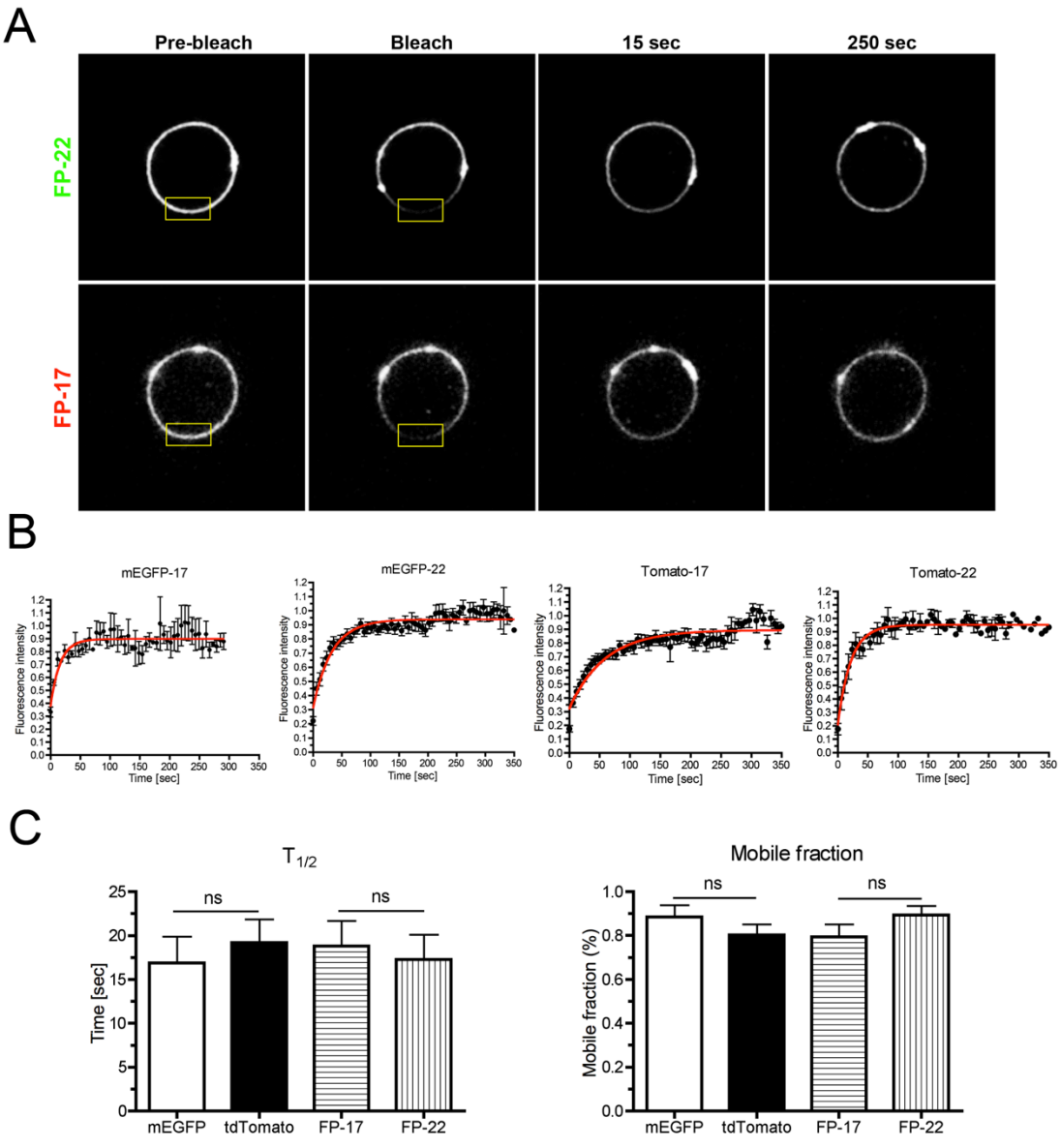
A
Pre-bleach
Bleach
15 sec
250 sec
FP-22
FP-17
B
mEGFP-17
mEGFP-22
Tomato-17
Tomato-22
Fluorescence intensity
Time [sec]
C
T1/2
Time [sec]
ns
mEGFP
tdTomato
FP-17
FP-22
Mobile fraction
Mobile fraction (%)

Figure 39: Diffusion of FP-17 and FP-22 in lipid nanotubes pulled by molecular motors from GUVs composed of ER lipids extracted from rat liver microsomes. (A) As indicated by the yellow ROI, a portion of a tube was bleached in both FP-17 and FP-22 channels and their fluorescent recovery was followed over time. 58 sec after bleaching both FP-17 and FP-22 showed a clear recovery of the fluorescence and in the latest timepoint (527 sec) both proteins displayed a fluorescent intensity, which is approximately the same of the prebleach images. (B) Fluorescent recovery curves have similar trends between mEGFP-17 and –22 and between Tomato-17 and -22, but they are different between Tomato and mEGFP fusion proteins; mEGFP-17 and -22 diffuse and reach plateau faster than Tomato-17 and -22. However, in the end the value that is reached at the steady-state is similar (n = 9 for each fluorescent protein). (C) Comparison of fluorescent recovery half times revealed a significant difference between mEGFP and Tomato and not between different TMD lengths (left histogram), while the analysis of mobile fractions demonstrates that the amount of protein that is free to diffuse is the same between all samples (right histogram).

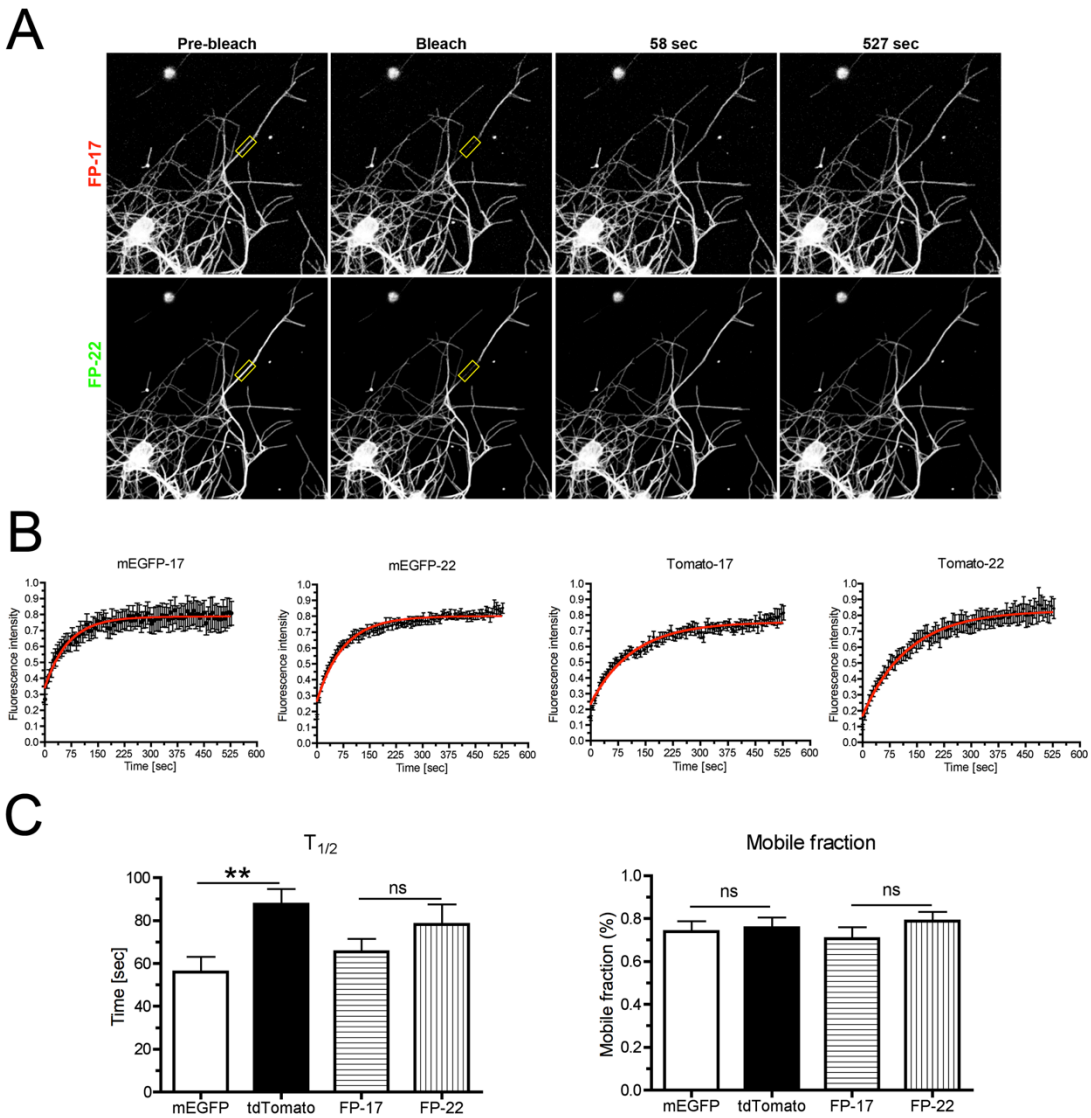
A
Pre-bleach
Bleach
58 sec
527 sec
FP-17
FP-22
B
mEGFP-17
mEGFP-22
Tomato-17
Tomato-22
Fluorescence intensity
Time [sec]
C
T1/2
Time [sec]
**
ns
Mobile fraction
Mobile fraction (%)
mEGFP
tdTomato
FP-17
FP-22

Figure 40: Lipid nanotubes pulled out by optical twezeers and micropipette aspiration system from GUVs composed of ER lipids extracted from rat liver microsomes. (A) Experimental configuration of nanotube pulling by an optical tweezers from a vesicle aspirated in a micropipette. The GUV, which contains biotinylated lipids is held on the left side by a micropipette connected to a water tank. On the right side, a membrane nanotube is pulled using a streptavidin-coated bead (black circle) trapped in an optical tweezers. By measuring the progressive displacement of the bead (Δx), the force (f) necessary to pull the tube and the tube radius ($R_{t)}$can be derived. (B) DIC image of a GUV aspirated by the micropipette and a tube pulled from the aspirated GUV using a bead trapped in an optical tweezers (scale bar = 5 μm). (C) Fluorescent confocal images of the vesicle and the tube shown in (B). The aspiration of the vesicle can be perceived by the membrane invagination inside the pipette. Upper panels show fluorescence intensities of FP-17 and FP-22 in the tube and vesicle in the first tension step, which corresponds to the tension applied to pull the tube. Both in the vesicle and in the tube FP-17 and FP-22 have about the same fluorescence intensities and seem to be homogenously distributed. Lower panels show the distribution of the two proteins in the final tension step; the increased tension can be appreciated by the bigger portion of the vesicle that is aspirated inside the micropipette. Because of the reduced tube radius, fluorescence signal in both channels was arbitrary enhanced to highlight the fluorescence signal in the tube. Even at this tension step, FP-17 and FP-22 seem to be equally distributed in the tube and in the vesicle (scale bar = 5 μm). (D) Quantitative analysis of mEGFP-17 versus Tomato-17 and mEGFP-22 versus Tomato-22 revealed that the sorting ratio is the same with the progressive increase of the membrane tension, indicating that fluorophores do not influence protein distribution. The same behavior was observed when FP-22 distribution was compared to that FP-17 (n = 12 for FP-22/FP-17, n = 7 for mEGFP-17/Tomato17 and n = 6 for mEGFP22/Tomato22).

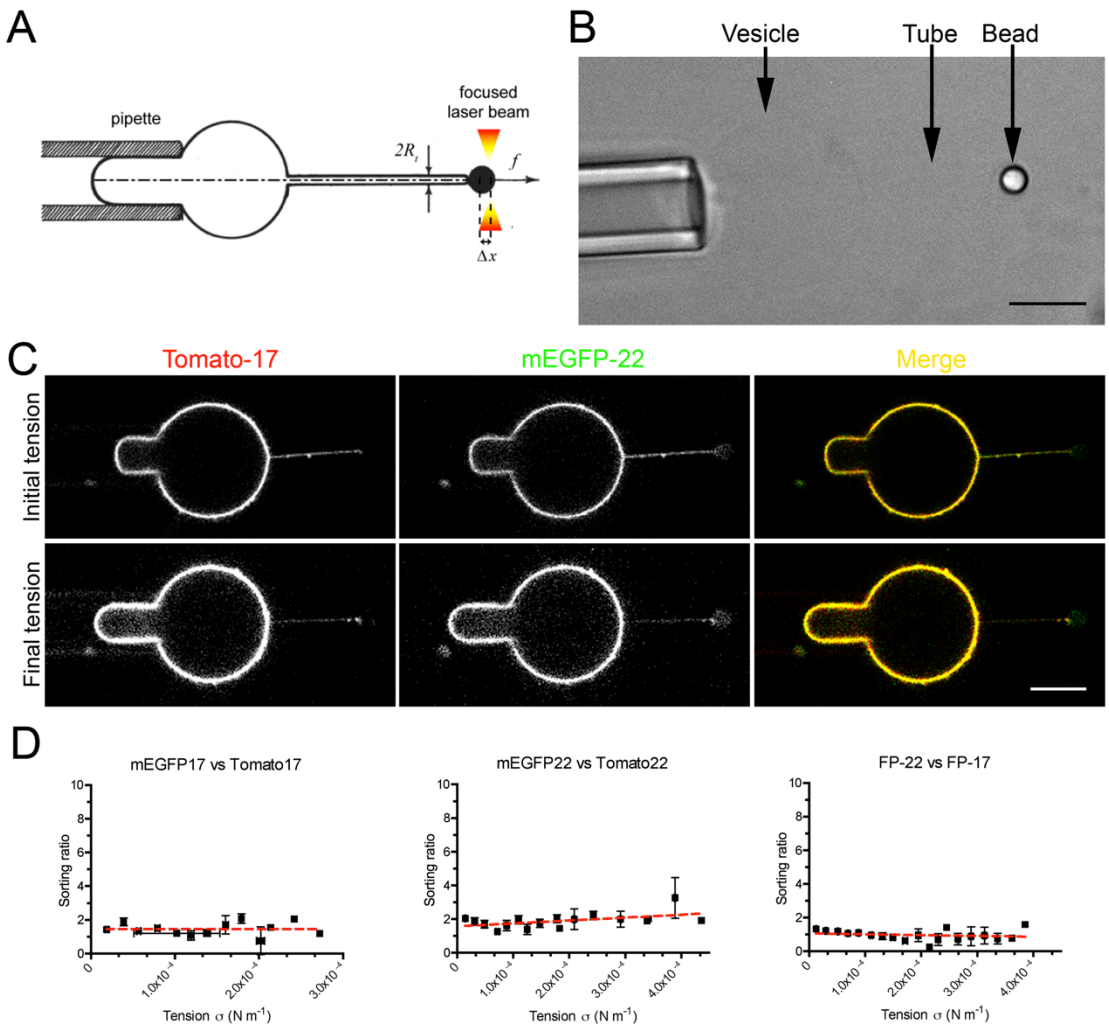
A
pipette
focused
laser beam
$2R_i$
f
Δx
B
Vesicle
Tube
Bead
C
Tomato-17
mEGFP-22
Merge
Initial tension
Final tension
D
mEGFP17 vs Tomato17
mEGFP22 vs Tomato22
FP-22 vs FP-17
Sorting ratio
Tension σ (N m^{-1})

Figure 41: Working model explaining the role of the export signal in protein transport along the secretory pathway. (A) Transport of transmembrane cargoes that contain the export signal in their cytosolic tail are strongly recruited at the ERES and efficiently transported to the Golgi apparatus, where they are excluded from retrograde transport back to the ER, probably through the interaction with an unknown protein, and then proceed directly to the plasma membrane, given a global high efficiency of their transport through the secretory pathway. (B) Cargoes that lack the export signal are still positively recruited at the ERES (even though less than signal-bearing cargoes), thanks to the physicochemical features of the TMD, and transported quite efficiently to the Golgi apparatus, where the vast majority of them are included into retrograde carriers and transported back to the ER. Since only a small fraction can escape from this futile recycling their arrival to the plasma membrane is significantly delayed and less efficient compared to the cargoes that have the export signal.

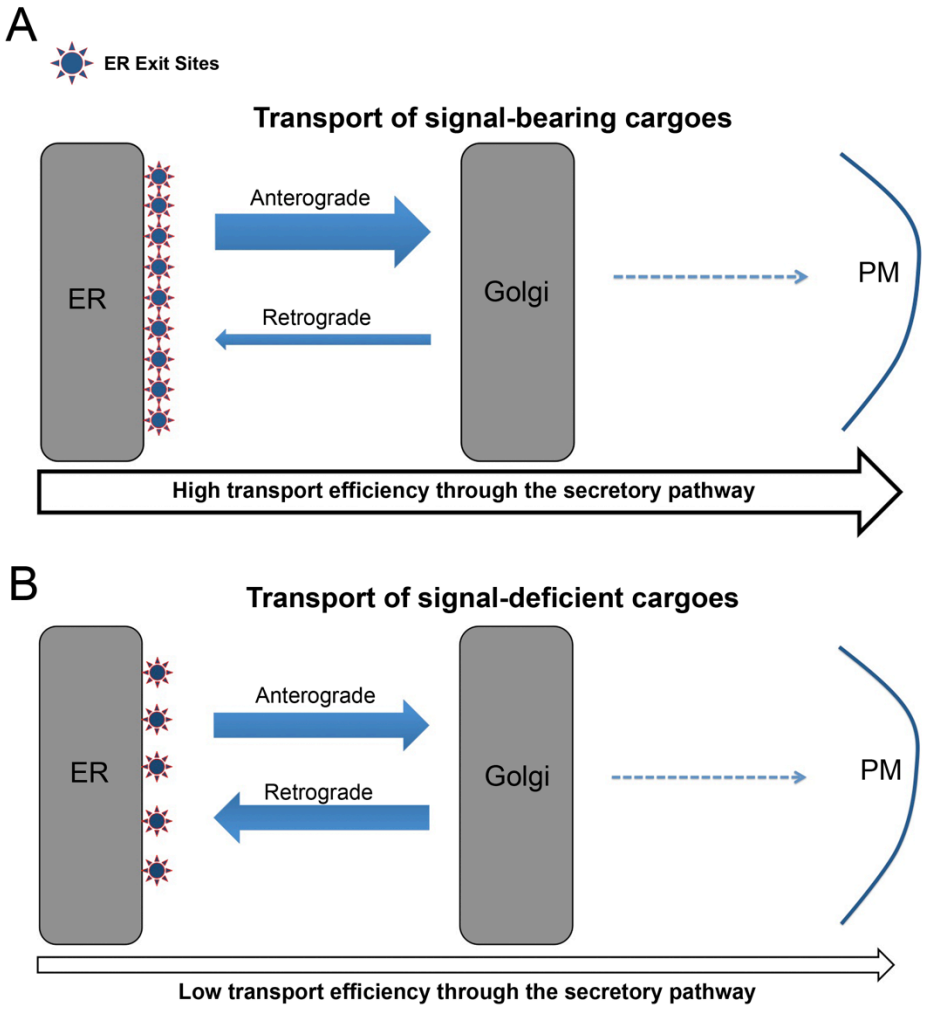
A
ER Exit Sites
Transport of signal-bearing cargoes
ER
Anterograde
Retrograde
Golgi
PM
High transport efficiency through the secretory pathway
B
Transport of signal-deficient cargoes
ER
Anterograde
Retrograde
Golgi
PM
Low transport efficiency through the secretory pathway

6. DISCUSSION

6.1 A novel role of the VSV-G di-acidic export signal at the Golgi apparatus

The importance of the export signal in protein transport along the secretory pathway is well known and many short aminoacid motives, such as di-acidic or di-hydrophobic stretches, have been identified in the cytosolic tail of different membrane cargoes (Barlowe, 2003). Till now, these export signals were thought to be important only for cargo concentration into COPII-coated vesicles; this belief was probably due to the fact that many proteins on which the export signal has been identified are components of the transport machinery at the ER-Golgi interface and, therefore, after leaving the ER they need to be recycled back for a new round of transport (Dancourt and Barlowe, 2010). But in the present study we demonstrated for the first time that the export signal of proteins that are localized at the plasma membrane assists their transport even in another step downstream the exit from the ER when proteins reach the Golgi apparatus.

Indeed, in the first part of the thesis we compared protein trafficking at the ER-Golgi interface of two model proteins, VSV-G and FP-22, by combining cDNA microinjection to temperature blocks and photobleaching approaches, which provide us a powerful tool to precisely analyze the transport of membrane proteins at the very early steps of the secretory pathway. VSV-G is the most used model protein to study transport along the secretory pathway and contains a well known di-acidic export signal in its cytosolic tail that leads to its recruitment into COPII-coated vesicles at the ERES (Nishimura and Balch, 1997). FP-22 is a TA chimeric protein, which contains a fluorescent protein exposed in the cytosol fused with an extended form of the TMD of cyt(b_5) (22 aa) and it is positively enriched at the ERES and transported to the plasma membrane thanks to the physicochemical features of the TMD (Bulbarelli et al., 2002; Pedrazzini et al., 1996; Ronchi et al., 2008). Our group previously demonstrated that

VSV-G is transported more efficiently to its final destination (in 75 min reaches is transported from the ER to the plasma membrane) compared to FP-22, which is still distributed between the ER and the Golgi 2h after cDNA microinjection (Ronchi et al., 2008). Even though FP-22 is less recruited at the ERES compared to VSV-G (Ronchi et al., 2008), in the present study we demonstrated that its anterograde transport from the ER to the Golgi apparatus is fast and with transport rates that are comparable to those of VSV-G and that the low efficiency of its transport is mainly given by the fact that the vast majority of FP-22, once arrives to the Golgi, is recycled back to the ER.

To investigate whether this mechanism was restricted to TA proteins only or whether was a more general phenomenon, we took advantage of a signal-deleted form of VSV-G (VSV-G AxA), which showed exactly the same behavior of FP-22. Already in 1997, Nishimura and colleagues demonstrated that the absence of the di-acidic sequence causes a stronger reduction in VSV-G recruitment into export domains and a reduction in its arrival to the plasma membrane (Nishimura and Balch, 1997). More recently, it has been also reported that the transport of VSV-G AxA is guided by the physicochemical features of the TMD, which has a predicted length of 22-23 aminoacids, like FP-22 (Dukhovny et al., 2009). In this study we found that the delayed arrival of VSV-G AxA to the plasma membrane is, again, due to a futile recycling from the Golgi to the ER, whose transport rate is similar to that of the anterograde transport (Golgi fluorescence is stable before bleaching at 20°C, see Fig. 31).

Taken together, these findings indicate a novel role of the VSV-G export signal at the Golgi apparatus, which is responsible for the exclusion of cargoes from futile cycling from the Golgi to the ER (Fig. 41). Indeed, signal-bearing cargoes are strongly recruited at the ERES thanks to the interaction between the export motif and the Sec24 subunit of COPII complex (Mancias and Goldberg, 2008), are rapidly transported to the Golgi apparatus and then directly to the plasma membrane. By contrast, signal-deficient cargoes such as FP-22 or VSV-G AxA are still efficiently anterogradely transported to the Golgi apparatus (fast fluorescence recovery after Golgi bleaching, see Fig. 22), but, then, the vast majority is included into retrograde transport carriers back to the ER and only a small fraction can progressively escape from this futile recycling and travel towards the plasma membrane, giving a global low efficiency of transport along the secretory pathway compared to membrane cargoes that contain the export signal. We think that this event not only influences the ef-

ficiency of transport through the secretory pathway of membrane proteins, but it might also be a general phenomenon influencing the trafficking of all proteins that lack an export signal. Indeed, this could be the reason why some Golgi enzymes continuously cycle between the ER and the Golgi; for example glycosilation Golgi enzymes lack any export signal and their correct localization is guaranteed by the physicochemical features of the TMD, whose length is shorter than the TMD of protein localized at the plasma membrane; but instead of being stably retained in the proper Golgi cisterna, they slowly cycled at the ER-Golgi interface (Munro, 1995; Opat et al., 2001).

Since we didn't provide any direct proof on the exclusion of VSV-G DxE from retrograde transport carriers, this hypothesis should be considered. Recently, Contreras and colleagues showed that the expression of a dominant negative form of p24, a key membrane component of COPI transport machinery, caused an acceleration of VSV-G transport, raising the possibility that even signal-bearing cargoes can be recycled from the Golgi to the ER (Contreras et al., 2012). This hypothesis needs to be further tested, but even if it is true, would not invalidate our working model; indeed, we clearly demonstrated that upon incubation at 20°C, VSV-G DxE and not FP-22 and VSV-G AxA is completely accumulated in the Golgi complex, indicating that the balance between anterograde and retrograde transports is strongly shifted in favour of the anterograde transport.

Of course the molecular mechanism of this phenomenon as well as the retrograde transport pathway that is involved in recycling cargoes from the Golgi to the ER remain to be elucidated. Concerning the retrograde pathway, two main retrograde routes from the Golgi to the ER have been identified (see section 1.4.2). The most studied route is the COPI-dependent pathway, which usually recognizes a specific retention motif in the cytosolic tail of membrane cargoes (KK and RR motives) (Michelsen et al., 2005). The second retrograde pathway is COPI-independent and Rab6-dependent and, till now, no specific signal on cargoes have been identified (Sannerud et al., 2003). Since our model proteins FP-22 and VSV-G AxA does not contain any known retention signal recognized by COPI machinery, the Rab6-dependent route represents a good candidate for their retrograde transport from the Golgi to the ER. Since in our laboratory are now available dominant negatives constructs of both Arf1 (a key component of COPI-dependent transport) and Rab6 (kind gift from Bruno Goud's lab, Institute Curie, Paris), we plan to co-microinject cells

with FP-22 and the dominant negative constructs in order to identify which is the retrograde pathway involved in futile recycling of signal-deficient cargoes and to investigate whether the inhibition of retrograde trafficking leads to a complete accumulation of FP-22 in the Golgi and to an acceleration of its transport to the plasma membrane.

The second point that needs to be elucidated concerns the identification of the protein/receptor that recognizes and binds the DxE sequence in the Golgi to exclude cargoes from recycling. How transport carriers that have left the ER can be recognized and fuse to the *cis*-face of the Golgi apparatus is a subject of intense studies and many proteins that facilitate this event have been identified. These proteins are mainly divided in two different families: multisubunit complexes, like the TRAPP-I and COG complexes, and coiled-coil proteins, called Golgins (Lorente-Rodriguez and Barlowe, 2011). These proteins act as tethering factors by binding specific components of transport vesicles, such as Rab GTPases, and they facilitate docking and fusion events of the vesicles to the correct acceptor compartment (Ramirez and Lowe, 2009). Even if all these tethering factors might be good candidates to interact with the export signal of protein cargoes, no evidences on their ability to bind the DxE sequence or other export sequences has been reported. Recently, D'Angelo and colleagues demonstrated for the first time that two *cis*-Golgi proteins, GRASP65 and GRASP55, also involved in vesicle tethering via the interaction with GM130 and Golgin-45 (Marra et al., 2007), bind C-terminal valine-bearing cargoes (but not the diacidic signal) and sequentially promote their transport to and through the Golgi complex (D'Angelo et al., 2009), suggesting that probably the transport to the Golgi is mediated by different proteins that recognize different class of secretory proteins.

6.2 Mechanisms of TMD-dependent sorting at the ER-Golgi interface

In the second part of my thesis, we focused our attention on one possible mechanism of TMD-dependent sorting of FP-17 and FP-22 at the very early steps of the secretory pathway. As described in section 1.7.2, our lab previously demonstrated that FP-17 and FP-22 are partitioned in different ER subdomains: FP-17 is excluded from ERES and distributed in both ER tubules and sheets, while FP-22 is segregated at the ERES and ER tubules and excluded from ER sheets. Even though in principle the recruitment of FP-22 could be explained by its interaction with a specific receptor that recognizes the TMDs, which has also been recently identified (Herzig et al., 2012), the exclusion of FP-17 from ERES and FP-22 partitioning in ER tubules are difficult to be explained on a receptor-mediated mechanism (Ronchi et al., 2008). Therefore, we hypothesized that the TMD-dependent partitioning of the two proteins could be due to specific interaction of TMDs with lipid bilayer and based on hydrophobic mismatch of the FP-22 within the thin ER bilayer (see section 1.7.2).

The possible mechanism we tested in the second part of the thesis was based on the idea that in curved domains, such as COPII nascent vesicles at ERES or ER peripheral tubules, FP-22 could tilt less its TMD with respect to the acyl chains of the bilayer, resulting in a more favorable interaction between the TMD and the acyl chains. In addition, in the first part of this thesis we demonstrated that proteins, whose transport is guided by the physicochemical features of the TMD, are also included into retrograde transport carriers, which are characterized, as COPII-coated vesicles and ER tubules, by high degree of curvature. To this aim, in collaboration with Jean-Baptiste Manneville and Bruno Goud (Institute Marie Curie, Paris), we used an *in vitro* model system to create highly curved domains in artificial membranes of defined lipid composition (reviewed in (Manneville et al., 2012). Quantitative analysis of the distribution of FP-17 and FP-22 in lipid nanotubes pulled out by molecular motors or optical tweezers and micropipette aspiration from GUVs composed of both POPC only or ER lipids extracted from rat liver microsomes revealed that the two proteins are uniformly distributed in highly curved domains, therefore demonstrating

that the membrane curvature alone is not sufficient to explain TMD-dependent partitioning of FP-22 in the early steps of the secretory pathway.

The second hypothesis we formulated was based on the idea that FP-22 could segregate in specific ER subdomains, where the lipid composition could locally increase the thickness of the thin ER bilayer and, thus, matches better with the length of the longer TMD. Although detailed informations are lacking, some studies have reported the presence of lipid microdomains in the ER membranes, suggesting an involvement in different processes, such as protein folding and transport (Bagnat et al., 2000; Campana et al., 2006). Particularly, a growing number of evidences suggests a key role of cholesterol in the formation of anterograde transport carriers and recruitment of membrane cargoes; indeed, the transport of VSV-G is impaired in cultured cells acutely depleted of cholesterol, which decreases the lateral mobility of cargoes and the turnover of Sec23 subunit of COPII (Ridsdale et al., 2006; Runz et al., 2006). More recently, another paper suggesting a role of cholesterol reported that a GPI-anchored protein, CD59, is segregated together with p24, the receptor of GPI-anchored cargoes, into COPII-coated vesicles specifically enriched in cholesterol and in C and D isoforms of Sec24 subunit of COPII (Bonnon et al., 2010).

Finally, our previous results with a model system consisting of proteoliposomes reconstituted either with wild-type cyt(b_5) or cyt(b_5) with an extended TMD are fully consistent with the hypothesis of lipid-based sorting. Differential scanning calorimetry and fluorescence measurements of lipid probes revealed that the extended b_5 mutant (which *in vivo* is sorted to the plasma membrane, like FP-22) partitions preferentially into domains enriched in acidic phospholipids or in ceramide, and that the wild-type protein is partially excluded from these domains (Ceppi et al., 2005). In our laboratory we are presently working on cultured cells trying to identify whether FP-17 and FP-22 interact with different lipid species and whether pharmacological lipid depletion affects FP-22 transport. Preliminary results are suggesting that FP-17 and FP-22 interact with a different lipid environment within the ER and that cholesterol depletion seems to cause an impairment in the transport of the longer TMD; in particular, we are comparing the impairment of FP-22 to that of VSV-G DxE and our results seem to indicate a stronger impairment of FP-22, suggesting a more important role of cholesterol in TMD-dependent transport with the respect of the sequence-dependent.

Another important aspect that could contribute to explain both the ER retention of FP-17 and the export of FP-22 concerns the oligomerization. Indeed, it has been

demonstrated that the export of some proteins requires their oligomerization (Nufer et al., 2003; Sato et al., 2003b) as well as protein aggregation could cause the immobilization of proteins in the ER and the failure of their export. Even though a previous work from our laboratory, based on sucrose gradient and FRAP analysis, suggested that both proteins are present as monomers, this hypothesis cannot be completely excluded. The diffusion coefficient of FP-17 and FP-22 is identical and indicates that both proteins are freely diffusible within the ER. In addition, the sedimentation of FP-17 and –22 in detergent-solubilized cell lysates on sucrose gradients also shows an aggregation state peak compatible with monomers (Ronchi et al., 2008). However, FRAP technique is not probably enough sensitive to distinguish between monomers and small oligomers and the sucrose gradient was performed on transfected cells, in which FP-22 was mainly localized to the plasma membrane and only a small fraction was still in the ER, and in the presence of the detergent Triton X-100, which might potentially destroy small FP-17 or -22 aggregates.

6.3 Conclusions

In the present work we analyzed two factors that strongly influence the transport of membrane proteins along the secretory pathway: the role of the ER export signal and of membrane curvature.

For the first time we identified a novel role of the di-acidic export signal at the Golgi apparatus, which is required to exclude cargoes from a futile inclusion into retrograde transport carriers and to guarantee an efficient transport through the secretory pathway and arrival to the plasma membrane.

Secondly, using an *in vitro* system we were able to investigate to role of membrane curvature alone in TMD-dependent partitioning of membrane proteins at the ER-Golgi interface and our data clearly indicate that the membrane curvature, even when the composition resembles that of the ER, is not sufficient to determine TMD-dependent segregation.

Since all plasma membrane-localized proteins are delivered to their final destination through the exocytic pathway and some pathological conditions are caused by

an altered protein trafficking, the understanding of the molecular mechanisms that determine the efficiency of protein export is of fundamental importance and the data presented in this thesis contribute to clarify some aspects that was previously unknown.

REFERENCES

Antonny, B. 2011. Mechanisms of membrane curvature sensing. *Annual review of biochemistry*. 80:101-123.

Antonny, B., S. Beraud-Dufour, P. Chardin, and M. Chabre. 1997. N-terminal hydrophobic residues of the G-protein ADP-ribosylation factor-1 insert into membrane phospholipids upon GDP to GTP exchange. *Biochemistry*. 36:4675-4684.

Antonny, B., P. Gounon, R. Schekman, and L. Orci. 2003. Self-assembly of minimal COPII cages. *EMBO reports*. 4:419-424.

Antonny, B., D. Madden, S. Hamamoto, L. Orci, and R. Schekman. 2001. Dynamics of the COPII coat with GTP and stable analogues. *Nature cell biology*. 3:531-537.

Aoe, T., A.J. Lee, E. van Donselaar, P.J. Peters, and V.W. Hsu. 1998. Modulation of intracellular transport by transported proteins: insight from regulation of COPI-mediated transport. *Proceedings of the National Academy of Sciences of the United States of America*. 95:1624-1629.

Appenzeller, C., H. Andersson, F. Kappeler, and H.P. Hauri. 1999. The lectin ERGIC-53 is a cargo transport receptor for glycoproteins. *Nature cell biology*. 1:330-334.

Aridor, M., J. Weissman, S. Bannykh, C. Nuoffer, and W.E. Balch. 1998. Cargo selection by the COPII budding machinery during export from the ER. *The Journal of cell biology*. 141:61-70.

Baba, T., C. Rauch, M. Xue, N. Terada, Y. Fujii, H. Ueda, I. Takayama, S. Ohno, E. Farge, and S.B. Sato. 2001. Clathrin-dependent and clathrin-independent endocytosis are differentially sensitive to insertion of poly (ethylene glycol)-derivatized cholesterol in the plasma membrane. *Traffic*. 2:501-512.

Bagnat, M., S. Keranen, A. Shevchenko, and K. Simons. 2000. Lipid rafts function in biosynthetic delivery of proteins to the cell surface in yeast. *Proc Natl Acad Sci U S A*. 97:3254-3259.

Balch, W.E., J.M. McCaffery, H. Plutner, and M.G. Farquhar. 1994. Vesicular stomatitis virus glycoprotein is sorted and concentrated during export from the endoplasmic reticulum. *Cell*. 76:841-852.

Barlowe, C. 2003. Signals for COPII-dependent export from the ER: what's the ticket out? *Trends in cell biology*. 13:295-300.

Barlowe, C., and R. Schekman. 1993. SEC12 encodes a guanine-nucleotide-exchange factor essential for transport vesicle budding from the ER. *Nature*. 365:347-349.

Beck, R., M. Rawet, F.T. Wieland, and D. Cassel. 2009. The COPI system: molecular mechanisms and function. *FEBS letters*. 583:2701-2709.

Bi, X., R.A. Corpina, and J. Goldberg. 2002. Structure of the Sec23/24-Sar1 pre-budding complex of the COPII vesicle coat. *Nature*. 419:271-277.

Bigay, J., J.F. Casella, G. Drin, B. Mesmin, and B. Antonny. 2005. ArfGAP1 responds to membrane curvature through the folding of a lipid packing sensor motif. *The EMBO journal*. 24:2244-2253.

Blobel, G., and B. Dobberstein. 1975. Transfer of proteins across membranes. *J. Cell Biol.* 67:835-851.

Bonifacino, J.S., and B.S. Glick. 2004. The mechanisms of vesicle budding and fusion. *Cell*. 116:153-166.

Bonnon, C., M.W. Wendeler, J.P. Paccaud, and H.P. Hauri. 2010. Selective export of human GPI-anchored proteins from the endoplasmic reticulum. *Journal of cell science*. 123:1705-1715.

Borgese, N., S. Brambillasca, and S. Colombo. 2007. How tails guide tail-anchored proteins to their destinations. *Curr Opin Cell Biol*. 19:368-375.

Borgese, N., S. Brambillasca, P. Soffientini, M. Yabal, and M. Makarow. 2003. Biogenesis of tail-anchored proteins. *Biochem. Soc. Trans.* 31:1238-1242.

Borgese, N., A. D'Arrigo, M. De Silvestris, and G. Pietrini. 1993. NADH-cytochrome b_5 reductase and cytochrome b_5-The problem of postranslational targeting to the Endoplasmic Reticulum. *In Subcellular Biochemistry Vol 21, N. Borgese and J.R. Harris, Eds, Plenum Press, New York*:313-341.

Borgese, N., and J.R. Harris. 1993. Endoplasmic Reticulum. *Subcellular Biochem.* 21 - Plenum Press, N.Y.

Brown, W.J., H. Plutner, D. Drecktrah, B.L. Judson, and W.E. Balch. 2008. The lysophospholipid acyltransferase antagonist CI-976 inhibits a late step in COPII vesicle budding. *Traffic*. 9:786-797.

Brugger, B., R. Sandhoff, S. Wegenhingel, K. Gorgas, J. Malsam, J.B. Helms, W.D. Lehmann, W. Nickel, and F.T. Wieland. 2000. Evidence for segregation of sphingomyelin and cholesterol during formation of COPI-coated vesicles. *J. Cell Biol.* 151:507-518.

Bulbarelli, A., T. Sprocati, M. Barberi, E. Pedrazzini, and N. Borgese. 2002. Trafficking of Tail-anchored Proteins: Transport from the Endoplasmic Reticulum to the Plasma Membrane and Sorting between Surface Domains in Polarised Epithelial Cells. *J. Cell Sci.* 115:1689-1702.

Callan-Jones, A., B. Sorre, and P. Bassereau. 2011. Curvature-driven lipid sorting in biomembranes. *Cold Spring Harb Perspect Biol*. 3.

Campana, V., D. Sarnataro, C. Fasano, P. Casanova, S. Paladino, and C. Zurzolo. 2006. Detergent-resistant membrane domains but not the proteasome are involved in the misfolding of a PrP mutant retained in the endoplasmic reticulum. *J Cell Sci*. 119:433-442.

Ceppi, P., S. Colombo, M. Francolini, F. Raimondo, N. Borgese, and M. Masserini. 2005. Two tail-anchored protein variants, differing in transmembrane domain length and intracellular sorting, interact differently with lipids. *Proc Natl Acad Sci U S A*. 102:16269-16274.

Contreras, F.X., A.M. Ernst, P. Haberkant, P. Bjorkholm, E. Lindahl, B. Gonen, C. Tischer, A. Elofsson, G. von Heijne, C. Thiele, R. Pepperkok, F. Wieland, and B. Brugger. 2012. Molecular recognition of a single sphingolipid species by a protein's transmembrane domain. *Nature*. 481:525-529.

Cukierman, E., I. Huber, M. Rotman, and D. Cassel. 1995. The ARF1 GTPase-activating protein: zinc finger motif and Golgi complex localization. *Science*. 270:1999-2002.

D'Angelo, G., L. Prencipe, L. Iodice, G. Beznoussenko, M. Savarese, P. Marra, G. Di Tullio, G. Martire, M.A. De Matteis, and S. Bonatti. 2009. GRASP65 and GRASP55 sequentially promote the transport of C-terminal valine-bearing cargos to and through the Golgi complex. *The Journal of biological chemistry*. 284:34849-34860.

Dancourt, J., and C. Barlowe. 2010. Protein sorting receptors in the early secretory pathway. *Annual review of biochemistry*. 79:777-802.

De Matteis, M.A., and A. Godi. 2004. PI-loting membrane traffic. *Nature cell biology*. 6:487-492.

de Planque, M.M.R., and J.A. Killian. 2003. Protein-lipid interactions studied with designed transmembrane peptides: role of hydrophobic matching and interfacial anchoring. *Mol Membrane Biol*. 20:271-284.

Dominguez, M., K. Dejgaard, J. Fullekrug, S. Dahan, A. Fazel, J.P. Paccaud, D.Y. Thomas, J.J. Bergeron, and T. Nilsson. 1998. gp25L/emp24/p24 protein family members of the cis-Golgi network bind both COP I and II coatomer. *The Journal of cell biology*. 140:751-765.

Dukhovny, A., Y. Yaffe, J. Shepshelovitch, and K. Hirschberg. 2009. The length of cargo-protein transmembrane segments drives secretory transport by facilitating cargo concentration in export domains. *J Cell Sci*. 122:1759-1767.

Espenshade, P., R.E. Gimeno, E. Holzmacher, P. Teung, and C.A. Kaiser. 1995. Yeast SEC16 gene encodes a multidomain vesicle coat protein that interacts with Sec23p. *The Journal of cell biology*. 131:311-324.

Farsad, K., and P. De Camilli. 2003. Mechanisms of membrane deformation. *Curr Opin Cell Biol*. 15:372-381.

Ferguson, S.M., and P. De Camilli. 2012. Dynamin, a membrane-remodelling GTPase. *Nature reviews. Molecular cell biology*. 13:75-88.

Fernandez-Ulibarri, I., M. Vilella, F. Lazaro-Dieguez, E. Sarri, S.E. Martinez, N. Jimenez, E. Claro, I. Merida, K.N. Burger, and G. Egea. 2007. Diacylglycerol is required for the formation of COPI vesicles in the Golgi-to-ER transport pathway. *Molecular biology of the cell*. 18:3250-3263.

Folch, J., M. Lees, and G.H. Sloane Stanley. 1957. A simple method for the isolation and purification of total lipides from animal tissues. *J Biol Chem*. 226:497-509.

Futai, E., S. Hamamoto, L. Orci, and R. Schekman. 2004. GTP/GDP exchange by Sec12p enables COPII vesicle bud formation on synthetic liposomes. *The EMBO journal*. 23:4146-4155.

Girod, A., B. Storrie, J.C. Simpson, L. Johannes, B. Goud, L.M. Roberts, J.M. Lord, T. Nilsson, and R. Pepperkok. 1999. Evidence for a COP-I-independent transport route from the Golgi complex to the endoplasmic reticulum. *Nature cell biology*. 1:423-430.

Goswami, D., K. Gowrishankar, S. Bilgrami, S. Ghosh, R. Raghupathy, R. Chadda, R. Vishwakarma, M. Rao, and S. Mayor. 2008. Nanoclusters of GPI-anchored proteins are formed by cortical actin-driven activity. *Cell*. 135:1085-1097.

Herzig, Y., H.J. Sharpe, Y. Elbaz, S. Munro, and M. Schuldiner. 2012. A systematic approach to pair secretory cargo receptors with their cargo suggests a mechanism for cargo selection by Erv14. *PLoS Biol*. 10:e1001329.

Hyman, A.A. 1991. Preparation of marked microtubules for the assay of the polarity of microtubule-based motors by fluorescence. *J Cell Sci Suppl*. 14:125-127.

Jahn, R., and H. Grubmuller. 2002. Membrane fusion. *Current opinion in cell biology*. 14:488-495.

Kaether, C., J. Scheuermann, M. Fassler, S. Zilow, K. Shirotani, C. Valkova, B. Novak, S. Kacmar, H. Steiner, and C. Haass. 2007. Endoplasmic reticulum retention

of the gamma-secretase complex component Pen2 by Rer1. *EMBO reports*. 8:743-748.

Kappeler, F., D.R. Klopfenstein, M. Foguet, J.P. Paccaud, and H.P. Hauri. 1997. The recycling of ERGIC-53 in the early secretory pathway. ERGIC-53 carries a cytosolic endoplasmic reticulum-exit determinant interacting with COPII. *The Journal of biological chemistry*. 272:31801-31808.

Kliouchnikov, L., J. Bigay, B. Mesmin, A. Parnis, M. Rawet, N. Goldfeder, B. Antonny, and D. Cassel. 2009. Discrete determinants in ArfGAP2/3 conferring Golgi localization and regulation by the COPI coat. *Molecular biology of the cell*. 20:859-869.

Kuehn, M.J., J.M. Herrmann, and R. Schekman. 1998. COPII-cargo interactions direct protein sorting into ER-derived transport vesicles. *Nature*. 391:187-190.

Kusimanen, E., and J. Saraste. 1989. Low temperature-induced transport blocks as tools to manipulate membrane traffic. *Methods Cell Biol.* 32:257-274.

Kwok, R., and E. Evans. 1981. Thermoelasticity of large lecithin bilayer vesicles. *Biophysical journal*. 35:637-652.

Lee, M.C., E.A. Miller, J. Goldberg, L. Orci, and R. Schekman. 2004. Bi-directional protein transport between the ER and Golgi. *Annu Rev Cell Dev Biol*. 20:87-123.

Lee, M.C., L. Orci, S. Hamamoto, E. Futai, M. Ravazzola, and R. Schekman. 2005. Sar1p N-terminal helix initiates membrane curvature and completes the fission of a COPII vesicle. *Cell*. 122:605-617.

Lenne, P.F., L. Wawrezinieck, F. Conchonaud, O. Wurtz, A. Boned, X.J. Guo, H. Rigneault, H.T. He, and D. Marguet. 2006. Dynamic molecular confinement in the plasma membrane by microdomains and the cytoskeleton meshwork. *The EMBO journal*. 25:3245-3256.

Lingwood, D., and K. Simons. 2010. Lipid rafts as a membrane-organizing principle. *Science*. 327:46-50.

Long, K.R., Y. Yamamoto, A.L. Baker, S.C. Watkins, C.B. Coyne, J.F. Conway, and M. Aridor. 2010. Sar1 assembly regulates membrane constriction and ER export. *The Journal of cell biology*. 190:115-128.

Lorente-Rodriguez, A., and C. Barlowe. 2011. Entry and exit mechanisms at the cis-face of the Golgi complex. *Cold Spring Harb Perspect Biol*. 3.

Lowry, O.H., N.J. Rosebrough, A.L. Farr, and R.J. Randall. 1951. Protein measurement with the Folin phenol reagent. *J. Biol. Chem.* 193:265-275.

Ma, D., N. Zerangue, Y.F. Lin, A. Collins, M. Yu, Y.N. Jan, and L.Y. Jan. 2001. Role of ER export signals in controlling surface potassium channel numbers. *Science*. 291:316-319.

Maceyka, M., and C.E. Machamer. 1997. Ceramide accumulation uncovers a cycling pathway for the cis-Golgi network marker, infectious bronchitis virus M protein. *The Journal of cell biology*. 139:1411-1418.

Malkus, P., F. Jiang, and R. Schekman. 2002. Concentrative sorting of secretory cargo proteins into COPII-coated vesicles. *The Journal of cell biology*. 159:915-921.

Mancias, J.D., and J. Goldberg. 2008. Structural basis of cargo membrane protein discrimination by the human COPII coat machinery. *Embo J*. 27:2918-2928.

Manneville, J.B., J.F. Casella, E. Ambroggio, P. Gounon, J. Bertherat, P. Bassereau, J. Cartaud, B. Antonny, and B. Goud. 2008. COPI coat assembly occurs on liquid-disordered domains and the associated membrane deformations are limited by membrane tension. *Proceedings of the National Academy of Sciences of the United States of America*. 105:16946-16951.

Manneville, J.B., C. Leduc, B. Sorre, and G. Drin. 2012. Studying in vitro membrane curvature recognition by proteins and its role in vesicular trafficking. *Methods Cell Biol*. 108:47-71.

Marra, P., T. Maffucci, T. Daniele, G.D. Tullio, Y. Ikehara, E.K. Chan, A. Luini, G. Beznoussenko, A. Mironov, and M.A. De Matteis. 2001. The GM130 and GRASP65 Golgi proteins cycle through and define a subdomain of the intermediate compartment. *Nature cell biology*. 3:1101-1113.

Marra, P., L. Salvatore, A. Mironov, Jr., A. Di Campli, G. Di Tullio, A. Trucco, G. Beznoussenko, A. Mironov, and M.A. De Matteis. 2007. The biogenesis of the Golgi ribbon: the roles of membrane input from the ER and of GM130. *Molecular biology of the cell*. 18:1595-1608.

Martinez-Menarguez, J.A., H.J. Geuze, J.W. Slot, and J. Klumperman. 1999. Vesicular tubular clusters between the ER and Golgi mediate concentration of soluble secretory proteins by exclusion from COPI-coated vesicles. *Cell*. 98:81-90.

Massaad, M.J., A. Franzusoff, and A. Herscovics. 1999. The processing alpha1,2-mannosidase of Saccharomyces cerevisiae depends on Rer1p for its localization in the endoplasmic reticulum. *European journal of cell biology*. 78:435-440.

Matanis, T., A. Akhmanova, P. Wulf, E. Del Nery, T. Weide, T. Stepanova, N. Galjart, F. Grosveld, B. Goud, C.I. De Zeeuw, A. Barnekow, and C.C. Hoogenraad. 2002. Bicaudal-D regulates COPI-independent Golgi-ER transport by recruiting the dynein-dynactin motor complex. *Nature cell biology*. 4:986-992.

Matsuoka, K., L. Orci, M. Amherdt, S.Y. Bednarek, S. Hamamoto, R. Schekman, and T. Yeung. 1998. COPII-coated vesicle formation reconstituted with purified coat proteins and chemically defined liposomes. *Cell*. 93:263-275.

McMahon, H.T., and J.L. Gallop. 2005. Membrane curvature and mechanisms of dynamic cell membrane remodelling. *Nature*. 438:590-596.

Mesmin, B., G. Drin, S. Levi, M. Rawet, D. Cassel, J. Bigay, and B. Antonny. 2007. Two lipid-packing sensor motifs contribute to the sensitivity of ArfGAP1 to membrane curvature. *Biochemistry*. 46:1779-1790.

Michelsen, K., H. Yuan, and B. Schwappach. 2005. Hide and run. Arginine-based endoplasmic-reticulum-sorting motifs in the assembly of heteromultimeric membrane proteins. *EMBO reports*. 6:717-722.

Munro, S. 1991. Sequences within and adjacent to the transmembrane segment of α-2,6-sialyltransferase specify Golgi retention. *EMBO J.* 10:3577-3588.

Munro, S. 1995. An investigation of the role of transmembrane domains in Golgi protein retention. *EMBO J.* 14:4695-4704.

Nienhaus, G.U., and J. Wiedenmann. 2009. Structure, dynamics and optical properties of fluorescent proteins: perspectives for marker development. *Chemphyschem*. 10:1369-1379.

Nishimura, N., and W.E. Balch. 1997. A di-acidic signal required for selective export from the endoplasmic reticulum. *Science*. 277:556-558.

Nufer, O., F. Kappeler, S. Guldbrandsen, and H.P. Hauri. 2003. ER export of ERGIC-53 is controlled by cooperation of targeting determinants in all three of its domains. *J Cell Sci*. 116:4429-4440.

Opat, A.S., C. van Vliet, and P.A. Gleeson. 2001. Trafficking and localisation of resident Golgi glycosylation enzymes. *Biochimie*. 83:763-773.

Otte, S., and C. Barlowe. 2002. The Erv41p-Erv46p complex: multiple export signals are required in trans for COPII-dependent transport from the ER. *The EMBO journal*. 21:6095-6104.

Pagano, A., F. Letourneur, D. Garcia-Estefania, J.L. Carpentier, L. Orci, and J.P. Paccaud. 1999. Sec24 proteins and sorting at the endoplasmic reticulum. *The Journal of biological chemistry*. 274:7833-7840.

Palade, G. 1975. Intracellular aspects of the process of protein synthesis. *Science*. 189:347-358.

Pathre, P., K. Shome, A. Blumental-Perry, A. Bielli, C.J. Haney, S. Alber, S.C. Watkins, G. Romero, and M. Aridor. 2003. Activation of phospholipase D by the small GTPase Sar1p is required to support COPII assembly and ER export. *The EMBO journal*. 22:4059-4069.

Pedrazzini, E., A. Villa, and N. Borgese. 1996. A mutant cytochrome b_5 with a lengthened membrane anchor escapes from the endoplasmic reticulum and reaches the plasma membrane. *Proc. Natl. Acad. Sci. USA*. 93:4207-4212.

Pedrazzini, E., A. Villa, R. Longhi, A. Bulbarelli, and N. Borgese. 2000. Mechanism of residence of cytochrome b(5), a tail-anchored protein, in the endoplasmic reticulum. *J. Cell Biol.* 148:899-914.

Rabouille, C., and J. Klumperman. 2005. Opinion: The maturing role of COPI vesicles in intra-Golgi transport. *Nature reviews. Molecular cell biology*. 6:812-817.

Ramirez, I.B., and M. Lowe. 2009. Golgins and GRASPs: holding the Golgi together. *Seminars in cell & developmental biology*. 20:770-779.

Rapoport, T.A. 2007. Protein translocation across the eukaryotic endoplasmic reticulum and bacterial plasma membranes. *Nature*. 450:663-669.

Ridsdale, A., M. Denis, P.Y. Gougeon, J.K. Ngsee, J.F. Presley, and X. Zha. 2006. Cholesterol is required for efficient endoplasmic reticulum-to-Golgi transport of secretory membrane proteins. *Molecular biology of the cell*. 17:1593-1605.

Rizzo, M.A., G.H. Springer, B. Granada, and D.W. Piston. 2004. An improved cyan fluorescent protein variant useful for FRET. *Nat Biotechnol*. 22:445-449.

Romer, W., L.L. Pontani, B. Sorre, C. Rentero, L. Berland, V. Chambon, C. Lamaze, P. Bassereau, C. Sykes, K. Gaus, and L. Johannes. 2010. Actin dynamics drive membrane reorganization and scission in clathrin-independent endocytosis. *Cell*. 140:540-553.

Ronchi, P., S. Colombo, M. Francolini, and N. Borgese. 2008. Transmembrane domain-dependent partitioning of membrane proteins within the endoplasmic reticulum. *J Cell Biol*. 181:105-118.

Rothman, J.E., and L. Orci. 1992. Molecular dissection of the secretory pathway. *Nature*. 355:409-415.

Roux, A., G. Cappello, J. Cartaud, J. Prost, B. Goud, and P. Bassereau. 2002. A minimal system allowing tubulation with molecular motors pulling on giant liposomes. *Proceedings of the National Academy of Sciences of the United States of America*. 99:5394-5399.

Roux, A., D. Cuvelier, P. Nassoy, J. Prost, P. Bassereau, and B. Goud. 2005. Role of curvature and phase transition in lipid sorting and fission of membrane tubules. *Embo J*. 24:1537-1545.

Runz, H., K. Miura, M. Weiss, and R. Pepperkok. 2006. Sterols regulate ER-export dynamics of secretory cargo protein ts-O45-G. *Embo J*. 25:2953-2965.

Saito, K., M. Chen, F. Bard, S. Chen, H. Zhou, D. Woodley, R. Polischuk, R. Schekman, and V. Malhotra. 2009. TANGO1 facilitates cargo loading at endoplasmic reticulum exit sites. *Cell*. 136:891-902.

Sannerud, R., J. Saraste, and B. Goud. 2003. Retrograde traffic in the biosynthetic-secretory route: pathways and machinery. *Current opinion in cell biology*. 15:438-445.

Sato, K., and A. Nakano. 2005. Dissection of COPII subunit-cargo assembly and disassembly kinetics during Sar1p-GTP hydrolysis. *Nat Struct Mol Biol*. 12:167-174.

Sato, K., M. Sato, and A. Nakano. 2003a. Rer1p, a retrieval receptor for ER membrane proteins, recognizes transmembrane domains in multiple modes. *Mol. Biol. Cell*. 14:3605-3616.

Sato, K., M. Sato, and A. Nakano. 2003b. Rer1p, a retrieval receptor for ER membrane proteins, recognizes transmembrane domains in multiple modes. *Molecular biology of the cell*. 14:3605-3616.

Sato, M., K. Sato, and A. Nakano. 1996. Endoplasmic reticulum localization of Sec12p is achieved by two mechanisms: Rer1p-dependent retrieval that requires the transmembrane domain and Rer1p-independent retention that involves the cytoplasmic domain. *The Journal of cell biology*. 134:279-293.

Schamel, W.W.A., S. Kuppig, B. Becker, K. Gimborn, H.P. Hauri, and M. Reth. 2003. A high-molecular-weight complex of membrane proteins BAP29/31 is involved in the retention of membrane-bound IgD in the endoplasmic reticulum. *Proc Natl Acad Sci U S A*. 100:9861-9866.

Sens, P., L. Johannes, and P. Bassereau. 2008. Biophysical approaches to protein-induced membrane deformations in trafficking. *Current opinion in cell biology*. 20:476-482.

Sevier, C.S., O.A. Weisz, M. Davis, and C.E. Machamer. 2000. Efficient export of the vesicular stomatitis virus G protein from the endoplasmic reticulum requires a signal in the cytoplasmic tail that includes both tyrosine-based and di-acidic motifs. *Molecular biology of the cell*. 11:13-22.

Sharpe, H.J., T.J. Stevens, and S. Munro. 2010. A comprehensive comparison of transmembrane domains reveals organelle-specific properties. *Cell*. 142:158-169.

Shikano, S., and M. Li. 2003. Membrane receptor trafficking: evidence of proximal and distal zones conferred by two independent endoplasmic reticulum localization signals. *Proceedings of the National Academy of Sciences of the United States of America*. 100:5783-5788.

Simons, K., and J.L. Sampaio. 2011. Membrane organization and lipid rafts. *Cold Spring Harb Perspect Biol*. 3:a004697.

Simons, K., and G. van Meer. 1988. Lipid sorting in epithelial cells. *Biochemistry*. 27:6197-6202.

Singer, S.J., and G.L. Nicolson. 1972. The fluid mosaic model of the structure of cell membranes. *Science*. 175:720-731.

Snapp, E.L., R.S. Hegde, M. Francolini, F. Lombardo, S. Colombo, E. Pedrazzini, N. Borgese, and J. Lippincott-Schwartz. 2003. Formation of stacked ER cisternae by low affinity protein interactions. *J. Cell Biol.* 163:257-269.

Sorre, B., A. Callan-Jones, J.B. Manneville, P. Nassoy, J.F. Joanny, J. Prost, B. Goud, and P. Bassereau. 2009. Curvature-driven lipid sorting needs proximity to a demixing point and is aided by proteins. *Proc Natl Acad Sci U S A*. 106:5622-5626.

Spang, A., K. Matsuoka, S. Hamamoto, R. Schekman, and L. Orci. 1998. Coatomer, Arf1p, and nucleotide are required to bud coat protein complex I-coated vesicles from large synthetic liposomes. *Proceedings of the National Academy of Sciences of the United States of America*. 95:11199-11204.

Sprong, H., P. van der Sluijs, and G. van Meer. 2001a. How proteins move lipids and lipids move proteins. *Nature reviews. Molecular cell biology*. 2:504-513.

Sprong, H., P. van der Sluijs, and G. van Meer. 2001b. How proteins move lipids and lipids move proteins. *Nature Reviews Mol. Cell Biol.* 2:504-513.

Stephens, D.J., N. Lin-Marq, A. Pagano, R. Pepperkok, and J.P. Paccaud. 2000. COPI-coated ER-to-Golgi transport complexes segregate from COPII in close proximity to ER exit sites. *Journal of cell science*. 113 (Pt 12):2177-2185.

Takida, S., Y. Maeda, and T. Kinoshita. 2008. Mammalian GPI-anchored proteins require p24 proteins for their efficient transport from the ER to the plasma membrane. *The Biochemical journal*. 409:555-562.

van Meer, G., D.R. Voelker, and G.W. Feigenson. 2008. Membrane lipids: where they are and how they behave. *Nature reviews. Molecular cell biology*. 9:112-124.

Voelker, D.R. 2005. Bridging gaps in phospholipid transport. *Trends Biochem Sci*. 30:396-404.

Voeltz, G.K., W.A. Prinz, Y. Shibata, J.M. Rist, and T.A. Rapoport. 2006. A class of membrane proteins shaping the tubular endoplasmic reticulum. *Cell*. 124:573-586.

Votsmeier, C., and D. Gallwitz. 2001. An acidic sequence of a putative yeast Golgi membrane protein binds COPII and facilitates ER export. *The EMBO journal*. 20:6742-6750.

White, J., L. Johannes, F. Mallard, A. Girod, S. Grill, S. Reinsch, P. Keller, B. Tzschaschel, A. Echard, B. Goud, and E.H. Stelzer. 1999. Rab6 coordinates a novel Golgi to ER retrograde transport pathway in live cells. *The Journal of cell biology*. 147:743-760.

Wieland, F.T., M.L. Gleason, T.A. Serafini, and J.E. Rothman. 1987. The rate of bulk flow form the endoplasmic reticulum to the cell surface. *Cell*. 50:289-300.

Yabal, M., S. Brambillasca, P. Soffientini, E. Pedrazzini, N. Borgese, and M. Makarow. 2003. Translocation of the C terminus of a tail-anchored protein across the endoplasmic reticulum membrane in yeast mutants defective in signal peptide-driven translocation. *J. Biol. Chem.* 278:3489-3496.